The IceCube Neutrino Observatory III: Cosmic Rays

THE ICECUBE COLLABORATION

1. The IceTop Air Shower Array: Detector Overview, Physics Goals and First Result **1**

2. Cosmic Ray Composition from the 40-string IceCube/IceTop Detectors **5**

3. Seasonal Variations of High Energy Cosmic Ray Muons Observed by the IceCube Observatory as a Probe of Kaon/Pion Ratio **9**

4. Measurements of the Air Shower Parameters with IceTop **13**

5. Extensive Air Showers Measured by the 79-string IceCube Observatory at South Pole **17**

6. Simulation of IceTop VEM calibration and the dependency on the snow layer **21**

7. Atmospheric Muon Spectrum from Catastrophic Energy Losses in IceCube **25**

8. Study of High p_T Muons in IceCube **29**

9. Energy Dependence of the Large Scale Galactic Cosmic Rays Anisotropy Measured With IceCube **33**

10. Observation of Anisotropy in the Arrival Direction Distribution of Cosmic Rays at TeV Energies with IceCube **37**

11. Measurement of the Solar Anisotropy with IceCube **41**

Keywords: *IceCube, IceTop, cosmic rays, mass composition, knee, muons, neutrinos, muon spectrum, stochastic losses, lateral distribution, extensive air showers, muon bundle, anisotropy*

THE ICECUBE COLLABORATION

R. ABBASI[28], Y. ABDOU[22], T. ABU-ZAYYAD[33], M. ACKERMANN[39], J. ADAMS[16], J. A. AGUILAR[28], M. AHLERS[32], M. M. ALLEN[36], D. ALTMANN[1], K. ANDEEN[28,a], J. AUFFENBERG[38], X. BAI[31,b], M. BAKER[28], S. W. BARWICK[24], R. BAY[7], J. L. BAZO ALBA[39], K. BEATTIE[8], J. J. BEATTY[18,19], S. BECHET[13], J. K. BECKER[10], K.-H. BECKER[38], M. L. BENABDERRAHMANE[39], S. BENZVI[28], J. BERDERMANN[39], P. BERGHAUS[31], D. BERLEY[17], E. BERNARDINI[39], D. BERTRAND[13], D. Z. BESSON[26], D. BINDIG[38], M. BISSOK[1], E. BLAUFUSS[17], J. BLUMENTHAL[1], D. J. BOERSMA[1], C. BOHM[34], D. BOSE[14], S. BÖSER[11], O. BOTNER[37], A. M. BROWN[16], S. BUITINK[14], K. S. CABALLERO-MORA[36], M. CARSON[22], D. CHIRKIN[28], B. CHRISTY[17], F. CLEVERMANN[20], S. COHEN[25], C. COLNARD[23], D. F. COWEN[36,35], A. H. CRUZ SILVA[39], M. V. D'AGOSTINO[7], M. DANNINGER[34], J. DAUGHHETEE[5], J. C. DAVIS[18], C. DE CLERCQ[14], T. DEGNER[11], L. DEMIRÖRS[25], F. DESCAMPS[22], P. DESIATI[28], G. DE VRIES-UITERWEERD[22], T. DEYOUNG[36], J. C. DÍAZ-VÉLEZ[28], M. DIERCKXSENS[13], J. DREYER[10], J. P. DUMM[28], M. DUNKMAN[36], J. EISCH[28], R. W. ELLSWORTH[17], O. ENGDEGÅRD[37], S. EULER[1], P. A. EVENSON[31], O. FADIRAN[28], A. R. FAZELY[6], A. FEDYNITCH[10], J. FEINTZEIG[28], T. FEUSELS[22], K. FILIMONOV[7], C. FINLEY[34], T. FISCHER-WASELS[38], B. D. FOX[36], A. FRANCKOWIAK[11], R. FRANKE[39], T. K. GAISSER[31], J. GALLAGHER[27], L. GERHARDT[8,7], L. GLADSTONE[28], T. GLÜSENKAMP[39], A. GOLDSCHMIDT[8], J. A. GOODMAN[17], D. GÓRA[39], D. GRANT[21], T. GRIESEL[29], A. GROSS[16,23], S. GRULLON[28], M. GURTNER[38], C. HA[36], A. HAJ ISMAIL[22], A. HALLGREN[37], F. HALZEN[28], K. HAN[39], K. HANSON[13,28], D. HEINEN[1], K. HELBING[38], R. HELLAUER[17], S. HICKFORD[16], G. C. HILL[28], K. D. HOFFMAN[17], A. HOMEIER[11], K. HOSHINA[28], W. HUELSNITZ[17,c], J.-P. HÜLSS[1], P. O. HULTH[34], K. HULTQVIST[34], S. HUSSAIN[31], A. ISHIHARA[15], E. JACOBI[39], J. JACOBSEN[28], G. S. JAPARIDZE[4], H. JOHANSSON[34], K.-H. KAMPERT[38], A. KAPPES[9], T. KARG[38], A. KARLE[28], P. KENNY[26], J. KIRYLUK[8,7], F. KISLAT[39], S. R. KLEIN[8,7], J.-H. KÖHNE[20], G. KOHNEN[30], H. KOLANOSKI[9], L. KÖPKE[29], S. KOPPER[38], D. J. KOSKINEN[36], M. KOWALSKI[11], T. KOWARIK[29], M. KRASBERG[28], T. KRINGS[1], G. KROLL[29], N. KURAHASHI[28], T. KUWABARA[31], M. LABARE[14], K. LAIHEM[1], H. LANDSMAN[28], M. J. LARSON[36], R. LAUER[39], J. LÜNEMANN[29], J. MADSEN[33], A. MAROTTA[13], R. MARUYAMA[28], K. MASE[15], H. S. MATIS[8], K. MEAGHER[17], M. MERCK[28], P. MÉSZÁROS[35,36], T. MEURES[13], S. MIARECKI[8,7], E. MIDDELL[39], N. MILKE[20], J. MILLER[37], T. MONTARULI[28,d], R. MORSE[28], S. M. MOVIT[35], R. NAHNHAUER[39], J. W. NAM[24], U. NAUMANN[38], D. R. NYGREN[8], S. ODROWSKI[23], A. OLIVAS[17], M. OLIVO[10], A. O'MURCHADHA[28], S. PANKNIN[11], L. PAUL[1], C. PÉREZ DE LOS HEROS[37], J. PETROVIC[13], A. PIEGSA[29], D. PIELOTH[20], R. PORRATA[7], J. POSSELT[38], P. B. PRICE[7], G. T. PRZYBYLSKI[8], K. RAWLINS[3], P. REDL[17], E. RESCONI[23,e], W. RHODE[20], M. RIBORDY[25], M. RICHMAN[17], J. P. RODRIGUES[28], F. ROTHMAIER[29], C. ROTT[18], T. RUHE[20], D. RUTLEDGE[36], B. RUZYBAYEV[31], D. RYCKBOSCH[22], H.-G. SANDER[29], M. SANTANDER[28], S. SARKAR[32], K. SCHATTO[29], T. SCHMIDT[17], A. SCHÖNWALD[39], A. SCHUKRAFT[1], A. SCHULTES[38], O. SCHULZ[23,f], M. SCHUNCK[1], D. SECKEL[31], B. SEMBURG[38], S. H. SEO[34], Y. SESTAYO[23], S. SEUNARINE[12], A. SILVESTRI[24], G. M. SPICZAK[33], C. SPIERING[39], M. STAMATIKOS[18,g], T. STANEV[31], T. STEZELBERGER[8], R. G. STOKSTAD[8], A. STÖSSL[39], E. A. STRAHLER[14], R. STRÖM[37], M. STÜER[11], G. W. SULLIVAN[17], Q. SWILLENS[13], H. TAAVOLA[37], I. TABOADA[5], A. TAMBURRO[33], A. TEPE[5], S. TER-ANTONYAN[6], S. TILAV[31], P. A. TOALE[2], S. TOSCANO[28], D. TOSI[39], N. VAN EIJNDHOVEN[14], J. VANDENBROUCKE[7], A. VAN OVERLOOP[22], J. VAN SANTEN[28], M. VEHRING[1], M. VOGE[11], C. WALCK[34], T. WALDENMAIER[9], M. WALLRAFF[1], M. WALTER[39], CH. WEAVER[28], C. WENDT[28], S. WESTERHOFF[28], N. WHITEHORN[28], K. WIEBE[29], C. H. WIEBUSCH[1], D. R. WILLIAMS[2], R. WISCHNEWSKI[39], H. WISSING[17], M. WOLF[23], T. R. WOOD[21], K. WOSCHNAGG[7], C. XU[31], D. L. XU[2], X. W. XU[6], J. P. YANEZ[39], G. YODH[24], S. YOSHIDA[15], P. ZARZHITSKY[2], M. ZOLL[34]

[1]*III. Physikalisches Institut, RWTH Aachen University, D-52056 Aachen, Germany*
[2]*Dept. of Physics and Astronomy, University of Alabama, Tuscaloosa, AL 35487, USA*
[3]*Dept. of Physics and Astronomy, University of Alaska Anchorage, 3211 Providence Dr., Anchorage, AK 99508, USA*
[4]*CTSPS, Clark-Atlanta University, Atlanta, GA 30314, USA*
[5]*School of Physics and Center for Relativistic Astrophysics, Georgia Institute of Technology, Atlanta, GA 30332, USA*
[6]*Dept. of Physics, Southern University, Baton Rouge, LA 70813, USA*
[7]*Dept. of Physics, University of California, Berkeley, CA 94720, USA*
[8]*Lawrence Berkeley National Laboratory, Berkeley, CA 94720, USA*
[9]*Institut für Physik, Humboldt-Universität zu Berlin, D-12489 Berlin, Germany*
[10]*Fakultät für Physik & Astronomie, Ruhr-Universität Bochum, D-44780 Bochum, Germany*
[11]*Physikalisches Institut, Universität Bonn, Nussallee 12, D-53115 Bonn, Germany*
[12]*Dept. of Physics, University of the West Indies, Cave Hill Campus, Bridgetown BB11000, Barbados*
[13]*Université Libre de Bruxelles, Science Faculty CP230, B-1050 Brussels, Belgium*
[14]*Vrije Universiteit Brussel, Dienst ELEM, B-1050 Brussels, Belgium*
[15]*Dept. of Physics, Chiba University, Chiba 263-8522, Japan*
[16]*Dept. of Physics and Astronomy, University of Canterbury, Private Bag 4800, Christchurch, New Zealand*
[17]*Dept. of Physics, University of Maryland, College Park, MD 20742, USA*
[18]*Dept. of Physics and Center for Cosmology and Astro-Particle Physics, Ohio State University, Columbus, OH 43210, USA*
[19]*Dept. of Astronomy, Ohio State University, Columbus, OH 43210, USA*
[20]*Dept. of Physics, TU Dortmund University, D-44221 Dortmund, Germany*
[21]*Dept. of Physics, University of Alberta, Edmonton, Alberta, Canada T6G 2G7*
[22]*Dept. of Physics and Astronomy, University of Gent, B-9000 Gent, Belgium*
[23]*Max-Planck-Institut für Kernphysik, D-69177 Heidelberg, Germany*
[24]*Dept. of Physics and Astronomy, University of California, Irvine, CA 92697, USA*
[25]*Laboratory for High Energy Physics, École Polytechnique Fédérale, CH-1015 Lausanne, Switzerland*
[26]*Dept. of Physics and Astronomy, University of Kansas, Lawrence, KS 66045, USA*
[27]*Dept. of Astronomy, University of Wisconsin, Madison, WI 53706, USA*
[28]*Dept. of Physics, University of Wisconsin, Madison, WI 53706, USA*
[29]*Institute of Physics, University of Mainz, Staudinger Weg 7, D-55099 Mainz, Germany*
[30]*Université de Mons, 7000 Mons, Belgium*
[31]*Bartol Research Institute and Department of Physics and Astronomy, University of Delaware, Newark, DE 19716, USA*
[32]*Dept. of Physics, University of Oxford, 1 Keble Road, Oxford OX1 3NP, UK*
[33]*Dept. of Physics, University of Wisconsin, River Falls, WI 54022, USA*
[34]*Oskar Klein Centre and Dept. of Physics, Stockholm University, SE-10691 Stockholm, Sweden*
[35]*Dept. of Astronomy and Astrophysics, Pennsylvania State University, University Park, PA 16802, USA*
[36]*Dept. of Physics, Pennsylvania State University, University Park, PA 16802, USA*
[37]*Dept. of Physics and Astronomy, Uppsala University, Box 516, S-75120 Uppsala, Sweden*
[38]*Dept. of Physics, University of Wuppertal, D-42119 Wuppertal, Germany*
[39]*DESY, D-15735 Zeuthen, Germany*
[a]*now at Dept. of Physics and Astronomy, Rutgers University, Piscataway, NJ 08854, USA*
[b]*now at Physics Department, South Dakota School of Mines and Technology, Rapid City, SD 57701, USA*
[c]*Los Alamos National Laboratory, Los Alamos, NM 87545, USA*
[d]*also Sezione INFN, Dipartimento di Fisica, I-70126, Bari, Italy*
[e]*now at T.U. Munich, 85748 Garching & Friedrich-Alexander Universität Erlangen-Nürnberg, 91058 Erlangen, Germany*
[f]*now at T.U. Munich, 85748 Garching, Germany*
[g]*NASA Goddard Space Flight Center, Greenbelt, MD 20771, USA*

Acknowledgments

We acknowledge the support from the following agencies: U.S. National Science Foundation-Office of Polar Programs, U.S. National Science Foundation-Physics Division, University of Wisconsin Alumni Research Foundation, the Grid Laboratory Of Wisconsin (GLOW) grid infrastructure at the University of Wisconsin - Madison, the Open Science Grid (OSG) grid infrastructure; U.S. Department of Energy, and National Energy Research Scientific Computing Center, the Louisiana Optical Network Initiative (LONI) grid computing resources; National Science and Engineering Research Council of Canada; Swedish Research Council, Swedish Polar Research Secretariat, Swedish National Infrastructure for Computing

(SNIC), and Knut and Alice Wallenberg Foundation, Sweden; German Ministry for Education and Research (BMBF), Deutsche Forschungsgemeinschaft (DFG), Research Department of Plasmas with Complex Interactions (Bochum), Germany; Fund for Scientific Research (FNRS-FWO), FWO Odysseus programme, Flanders Institute to encourage scientific and technological research in industry (IWT), Belgian Federal Science Policy Office (Belspo); University of Oxford, United Kingdom; Marsden Fund, New Zealand; Japan Society for Promotion of Science (JSPS); the Swiss National Science Foundation (SNSF), Switzerland; D. Boersma acknowledges support by the EU Marie Curie IRG Program; A. Groß acknowledges support by the EU Marie Curie OIF Program; J. P. Rodrigues acknowledges support by the Capes Foundation, Ministry of Education of Brazil; A. Schukraft acknowledges the support by the German Telekom Foundation; N. Whitehorn acknowledges support by the NSF Graduate Research Fellowships Program.

The IceTop Air Shower Array: detector overview, physics goals and first results

THE ICECUBE COLLABORATION[1]
[1]*See special section in these proceedings*

Abstract: IceTop, the surface component of the IceCube Neutrino Observatory at the South Pole, is an air shower array with an area of $1\,\mathrm{km}^2$. The detector is primarily designed to study the mass composition of primary cosmic rays in the energy range from about 10^{14} eV to 10^{18} eV by exploiting the correlation between the shower energy measured in IceTop and the energy deposited by muons in the deep ice. Construction of IceCube, including the IceTop component, was completed in December 2010. The final detector configuration, first operation and performance experiences, the development of an analysis framework, and first results will be reported.

Corresponding author: Hermann Kolanoski (*Hermann.Kolanoski@desy.de*)
Institut für Physik, Humboldt-Universität zu Berlin, D-12489 Berlin, Germany

Keywords: Cosmic rays, IceCube, IceTop

1 Introduction

The Neutrino Observatory IceCube is a 1-km^3 detector situated in the ice of the geographic South Pole at a depth of about 2000 m. IceTop, the surface component of IceCube, is an air shower array covering an area of $1\,\mathrm{km}^2$. The prime purpose of IceTop is the determination of the mass composition of primary cosmic rays in the energy range from about 10^{14} eV to 10^{18} eV. In the 'knee' region, at several PeV, the spectral index of the observed cosmic ray energy spectrum changes. Several experiments found this change to be accompanied by a change in the chemical composition of the primaries. However, details of the features are not well known. In particular, there may be at the high end of the IceTop energy range another change of the spectral index and an accompanying change of the composition, possibly indicating the transition from galactic to extra-galactic origin of cosmic rays. An improvement of the experimental situation in this energy range – between direct measurements with balloons and satellites and the highest energies tackled by experiments like HiRes and Auger – is one of the main goals of cosmic ray physics with IceCube.

The mass determination from extended air showers (EAS) is notoriously difficult because the measurements are indirect and have to rely on models for the hadronisation processes. Observables sensitive to the primary mass composition are mainly the height of the shower maximum (measured through fluorescence, Cherenkov or radio emission) and the number of muons in a shower. Concerning the muon rate, the highest energy muons stemming from the first interactions in the higher atmosphere are most closely correlated to the mass of the primary nucleus. IceCube, in combination with IceTop, offers the unique possibility to observe these muons, typically with initial energies above about 500 GeV, in the deep ice in coincidence with the mostly electromagnetically deposited shower energy measured at the surface. This provides an exceptionally powerful method for the determination of the mass composition.

To scrutinize the dependence on hadronisation models, several alternative methods for studying mass composition have been developed by the IceCube collaboration. Other mass sensitive observables are for example: the shower absorption in the atmosphere at different zenith angles, the number of dominantly low-energy muons in the surface detector, and other shower properties such as shower age and shower front curvature.

The IceTop array has additionally been used to study high-p_T muons, PeV-gammas and transient events, such as the radiation effects of solar flares. It also serves as a veto for the detection of downward-going neutrinos with IceCube and for direction calibration.

2 The detector

The IceCube construction was completed in December 2010. The results presented here are based on data taken with smaller detector configurations.

IceCube: The main component of Icecube is an array of 86 strings equipped with 5160 light detectors in a volume

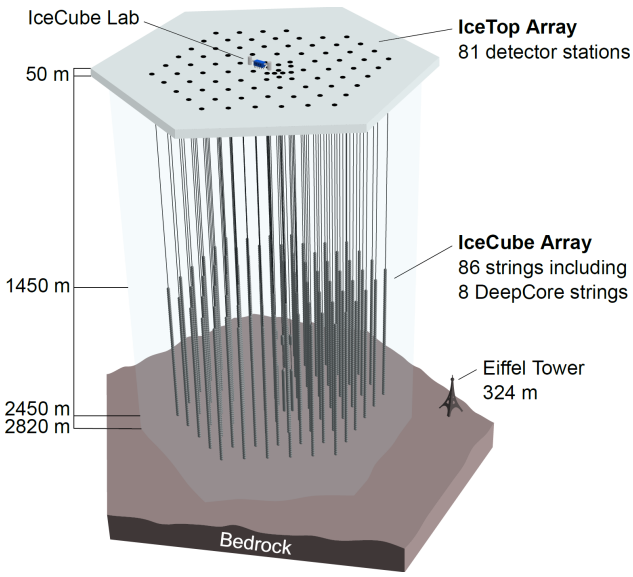

Figure 1: The IceCube Observatory with its components DeepCore and IceTop.

of 1 km^3 at a depth between 1450 m and 2450 m (Fig. 1). In the lower part of the detector a section called DeepCore is more densely instrumented. The main purpose of IceCube is the detection of high energy neutrinos from astrophysical sources via the Cherenkov light of charged particles generated in neutrino interactions in the ice or the rock below the ice.

IceTop: The IceTop air shower array is located above IceCube at a height of 2832 m above sea level, corresponding to an atmospheric depth of about 680 g/cm^2. It consists of 162 ice Cherenkov tanks, placed at 81 stations and distributed over an area of 1 km^2 on a grid with mean spacing of 125 m (Fig. 1). In the center of the array, three stations have been installed at intermediate positions. Together with the neighbouring stations they form an in-fill array for denser shower sampling. Each station comprises two cylindrical tanks, 10 m apart from each other, with a diameter of $1.86\,\mathrm{m}$ and filled with $90\,\mathrm{cm}$ ice. The tanks are embedded into the snow so that their top surface is level with the surrounding snow to minimize temperature variations and snow accumulation caused by wind drift. However, snow accumulation (mainly due to irregular snow surfaces) cannot be completely avoided so that the snow height has to be monitored (see ref. [1]) and taken into account in simulation and reconstruction (currently this is still a source of non-negligible systematic uncertainties).

Each tank is equipped with two 'Digital Optical Modules' (DOMs), each containing a $10''$ photo multiplier tube (PMT) to record the Cherenkov light of charged particles that penetrate the tank. In addition, a DOM houses complex electronic circuitry supplying signal digitisation, readout, triggering, calibration, data transfer and various control functions. The most important feature of the DOM electronics is the recording of the analog waveforms in $3.3\,\mathrm{ns}$

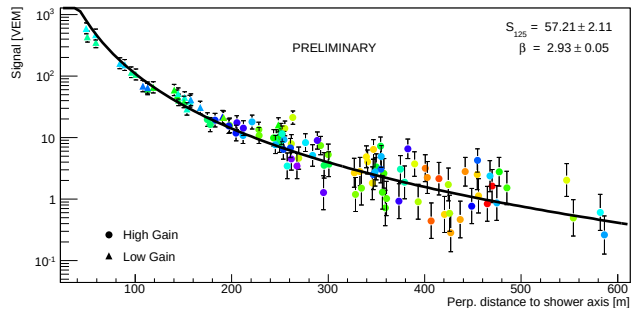

Figure 2: Reconstruction of shower parameters from the lateral distribution.

wide bins for a duration of $422\,\mathrm{ns}$. DOMs, electronics and readout scheme are the same as for the in-ice detector.

The two DOMs in each tank are operated at different PMT gains ($1 \cdot 10^5$ and $5 \cdot 10^6$) to cover a dynamic range of more than 10^4. The measured charges are expressed in units of 'vertical equivalent muons' (VEM) determined by calibrating each DOM with muons (see ref. [1]).

To initiate the readout of DOMs, a local coincidence of the two high gain DOMs of a station is required. This results in a station trigger rate of about 30 Hz compared to about 1600 Hz of a single high gain DOM at a threshold of about 0.1 VEM. The data are written to a permanent storage medium, and are thus available for analysis, if the readouts of six or more DOMs are launched by a local coincidence. This leads to a trigger threshold of about 300 TeV. Additionally, IceTop is always read out in case of a trigger issued by another detector component (and vice versa). For each single tank above threshold, even without a local coincidence, condensed data containing integrated charge and time stamp are transmitted. These so-called SLC hits (SLC = 'soft local coincidence') are useful for detecting single muons in showers where the electromagnetic component has been absorbed (low energies, outer region of showers, inclined showers).

For monitoring transient events via rate variations, the time of single hits in different tanks with various thresholds are histogrammed.

3 Shower reconstruction

For each triggered tank in an event, time and charge of the signal are evaluated for further processing. Likelihood maximisation methods are used to reconstruct location, direction and size of the recorded showers. In general, signal times contain the direction information, and the charge distribution is connected to shower size and core location. The standard analysis requires five or more triggered stations leading to a reconstruction threshold of about $500\,\mathrm{TeV}$. A constant efficiency is reached at about $1\,\mathrm{PeV}$, depending on shower inclination. For small showers an effort was launched to decrease the threshold to about $100\,\mathrm{TeV}$ with a modified reconstruction requiring only three stations.

The lateral signal distribution is fitted by a function which describes the logarithm of the tank signals as a second order polynomial in the logarithm of the distance from the shower axis (Fig. 2). Characterizing the shower size the signal S_{125} at a reference radius $R_{\mathrm{ref}} = 125\,\mathrm{m}$, coinciding with the grid spacing, has been used for the analyses presented in this paper. Studies of alternative lateral distribution functions are reported in a separate contribution to this conference [2].

The true energy spectrum is obtained by unfolding the S_{125} distribution in different zenith angular ranges. Since the unfolding matrices depend on the primary mass composition, a mass model has to be assumed [3] or the correlation with mass sensitive observables, most notably the muon number in the deep detector, has to be exploited for an essentially two-dimensional unfolding [4].

The energy resolution improves with energy and approaches 0.05 in $\log_{10} E$, or 12 % in E, at about 10 PeV for zenith angles less than 30°. The angular resolution is better than 1°, almost independent of energy and zenith angle. The detector coverage is $A\,\Omega \approx 3\,\mathrm{km}^2\,\mathrm{sr}$ for IceTop alone and $A\,\Omega \approx 0.3\,\mathrm{km}^2\,\mathrm{sr}$ for coincidences with the in-ice detector.

4 First results

Energy spectrum: The shower reconstruction from IceTop signals has been developed mainly using data taken with 26 stations (nearly 1/3 of the complete detector) in 2007. The spectra of the shower size parameter S_{125} for three different zenith angular ranges are shown in Fig. 3. Except for the threshold region, this parameter is a close proxy for the primary energy for a given zenith angle range. The relation between S_{125} and the true energy is mass dependent. Under the assumption of an isotropic cosmic ray flux, the S_{125} spectra for different zenith angles should yield the same energy spectrum. It has been shown that this can only be achieved under the assumption of a mixed composition [3].

A first evaluation of IceTop data from the 2010 season with 79 IceCube strings and 73 IceTop stations is reported elsewhere in these proceedings [5].

Mass composition using IceTop and deep-ice coincidences: As emphasized in the introduction, a strength of IceCube is the possibility to measure high energy muons in the deep ice in coincidence with the shower reconstructed in IceTop. The first analysis of such coincident data is presented at this conference [4]. The data set is constrained to a small fraction of the detector and a relatively short time period (about 1 month). However, the results are currently more affected by systematic uncertainties than by statistics.

Figure 4 shows a simulation of the correlation between the parameter K_{70}, which measures the muon energy in the deep ice, and the shower size parameter S_{125}, which is a measure of the electromagnetic component of the shower. Different primary masses populate different bands in this

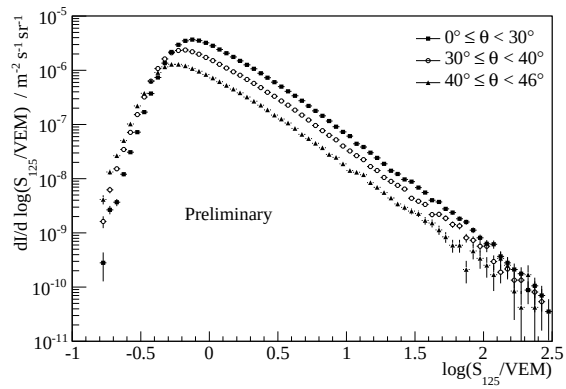

Figure 3: Measured spectrum of the shower size parameter S_{125} for three different zenith angular ranges (data from 6 months with 26 IceTop stations).

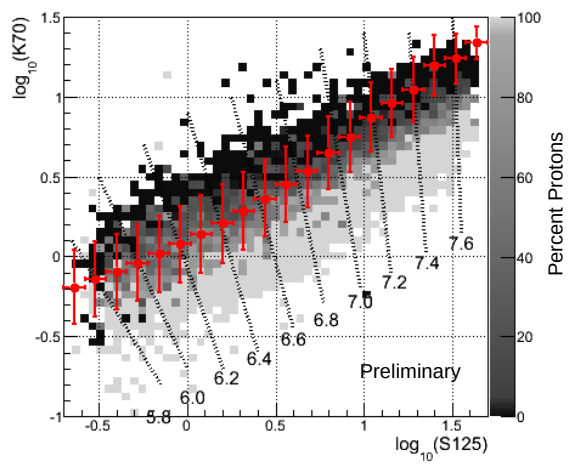

Figure 4: Mass composition measurement: plotted is the muon energy parameter K_{70} measured in the deep ice versus the shower size S_{125}. The band is obtained by simulating proton and iron primaries. The shading indicates the proton content, with 100% protons at the bottom und 100% iron at the top. Indicated are also curves of constant primary energy as determined by a neural net (the labels are in units $\log_{10} E/\mathrm{GeV}$). The points and the vertical bars are averages and dispersions, respectively, of the measured experimental distributions of a $\log_{10} S_{125}$ bin (indicated by the horizontal bars) projected unto the $\log_{10} K_{70}$ axis.

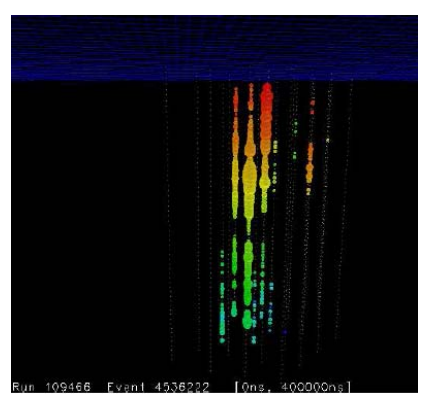

Figure 5: IceCube event display showing light signals in DOMs: Candidate muon bundle with a high-p_T muon (on the right).

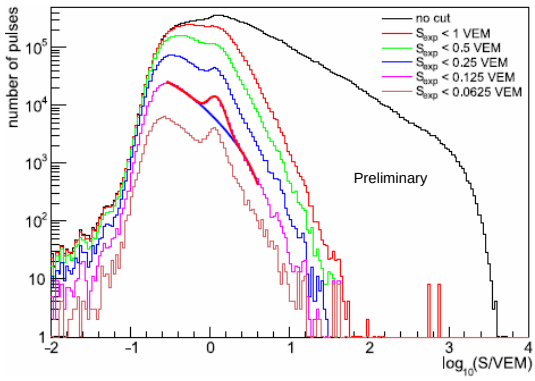

Figure 6: Muon counting in IceTop: Distribution of tank signals for various cuts on the signal expectation S_{exp} in the energy range between 1 and 30 PeV.

plot. Indicated are also curves of constant primary energy. The data points in $\log S_{125}$ bins are plotted with the dispersion of their distribution along the K_{70} axis.

With a neural network, the primary energy and a parameter related to $\ln A$ (A is the atomic mass number) has been determined yielding an energy and average $\ln A$ spectrum between 1 and 50 PeV. The method allows for the extraction of multiple mass contributions from fits to the neural network output, see details in ref. [4].

High-p_T muons: Prompt decays of heavy flavour hadrons occurring in the first interactions are expected to produce muons with large transverse momentum. The predictions are still very model dependent. In these proceedings, an analysis is presented [6] where high-p_T muons have been found as single tracks separated from a muon bundle by more than 200 m (Fig. 5). Current work concentrates on understanding the systematic uncertainties in the resulting p_T distribution.

Searching for PeV gamma rays: IceCube can efficiently distinguish PeV gamma rays from the background of cosmic rays by exploiting coincident in-ice signals as veto. Gamma-ray air showers have a much lower muon content than cosmic ray air showers of the same energy. Candidate events are selected from those showers that lack a signal from a muon bundle in the deep ice. Results of one year of data, taken in the 2008/2009 season when the detector consisted of 40 strings and 40 surface stations, are presented at this conference [7]. The projected gamma-ray sensitivity of the final detector is also given.

Muon counting in IceTop: The muon content of a shower is a mass sensitive observable since heavier primaries tend to have a higher muon abundance. Although the number of high energy muons in the muon bundle near the shower core is most sensitive, muons counted at the surface (at typically much lower energies than in the deep ice) provide additional information on the mass. The comparison of both methods allows one to test hadronisation models.

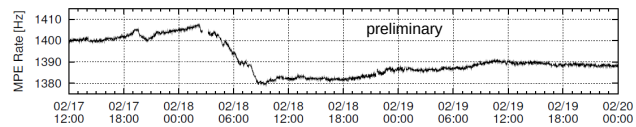

Figure 7: Average scaler rates of several tanks in IceTop during a period in February 2011 when a Forbush decrease occured.

Muonic and electromagnetic signals in IceTop can in general not be distinguished. However, muons show up as a relatively constant signal of about 1 VEM at larger distances from the shower axis where the expectation value of a tank signal, S_{exp}, becomes small compared to a muon signal (S_{exp} is obtained from the fit to the lateral shower distribution). As shown in Fig. 6, the muon signal becomes more and more prominent when requiring smaller S_{exp}. For $S_{exp} < 0.125$ VEM the figure illustrates that the number of muons can be well fitted. Comparing these muon numbers as a function of energy to simulations of different primary masses an independent information on the mass composition is obtained.

Heliospheric physics: The IceTop tanks detect secondary particles produced by cosmic rays in the multi-GeV energy regime interacting in the atmosphere with a counting rate exceeding 1 kHz per detector. With IceTop, heliosperic disturbances of this rate can be studied with very good time resolution. Since each detector has a different threshold setting, it is also possible to estimate the energy spectrum of the cosmic rays related to such events. In an IceCube contribution to this conference [8] the performance during a Forbush decrease observed in February 2011 is demonstrated (Fig. 7).

Other cosmic ray results: At this conference the Icecube Collaboration also reports results on the observation of cosmic ray anisotropies in the southern sky [9]. These results and the cosmic ray studies in ref. [10] use all muons detected in the deep detector which gives a much larger angular coverage.

References

[1] IceCube Collaboration, paper 899, these proceedings.
[2] IceCube Collaboration, paper 379, these proceedings.
[3] F. Kislat for the IceCube Coll., Astrophys. Space Sci. Trans. 7 (2011) 175.
[4] IceCube Collaboration, paper 923, these proceedings.
[5] IceCube Collaboration, paper 838, these proceedings.
[6] IceCube Collaboration, paper 323, these proceedings.
[7] IceCube Collaboration, paper 939, these proceedings.
[8] IceCube Collaboration, paper 735, these proceedings.
[9] IceCube Collaboration, papers 305, 306, 308, these proceedings.
[10] IceCube Collaboration, papers 85, 662, these proceedings.

Cosmic Ray Composition from the 40-string IceCube/IceTop Detectors

THE ICECUBE COLLABORATION[1]
[1]*See special section in these proceedings*

Abstract: The IceCube Observatory at the South Pole is composed of a deep detector and a surface detector, IceTop, both of which use Cherenkov light to detect charged particles. Cosmic ray air showers contain multiple particle components: in particular, electrons and muons detectable at the surface by IceTop, and high-energy muons detectable by the deep IceCube detector, in relative amounts that depend on the primary cosmic ray mass. Thus, coincident events can be used to measure both the energy and the mass composition. Here, a neural network is trained with simulations to map observables from the two detectors (input) into energy and mass estimators (output). Experimental data is then run through the same network, to measure the energy spectrum and average logarithmic mass of cosmic rays in the energy range of about 1-30 PeV.

Corresponding authors: K. Andeen[2] (*karen.andeen@icecube.wisc.edu*), K. Rawlins[3], T. Feusels[4]
[2]*Dept. of Physics, University of Wisconsin-Madison, WI 53706, USA (now at Rutgers University)*
[3]*Dept. of Physics and Astronomy, University of Alaska Anchorage, AK 99508, USA*
[4]*Dept. of Physics and Astronomy, Gent University, B-9000 Gent, Belgium*

Keywords: mass; composition; knee; IceCube; IceTop

1 Introduction

Measuring more than one particle component of a cosmic ray air shower is a powerful tool for separating light and heavy nuclei in Extensive Air Shower (EAS) data, at energies at the knee and above where direct measurements of cosmic rays are not possible. The IceCube Observatory at the South Pole is being used in such a manner, with an array of light sensors (Digital Optical Modules, or DOMs) buried on strings between 1450 and 2450 m (herein "IceCube") together in coincidence with a corresponding array of DOMs in frozen water tanks on the surface ("IceTop"). An IceTop "station" is two tanks separated by 10 m; IceCube strings and IceTop stations are separated by 125 m [1].

Both instruments measure the Cherenkov light emitted by charged particles through the surrounding medium. In IceTop, the medium is water frozen in tanks at the site. The DOMs in the tanks measure light from the electromagnetic and GeV muonic components of the EAS. In IceCube, the medium is the Antarctic icecap, and the deeply-buried DOMs measure light from high-energy (TeV) muons bundled near the central axis of the shower.

2 Reconstruction

Events in IceTop are reconstructed by a likelihood method [3], comparing the detected signal locations, charges, and times from hit stations (as well as the locations of not-hit stations) to what is expected from a cosmic ray EAS. Signal *times* are compared to an expected timing profile, and signal *charges* are compared to an expected lateral distribution function (LDF). The LDF used, a function of the perpendicular distance from the shower axis, r, is known as the "Double Logarithmic Parabola,":

$$S(r) = S_{\mathrm{ref}} \cdot \left(\frac{r}{R_{\mathrm{ref}}}\right)^{-\beta-\kappa\log_{10}\left(\frac{r}{R_{\mathrm{ref}}}\right)} . \qquad (1)$$

The logarithm of the signals S are assumed to have normal distributions, and are expressed in units of "vertical equivalent muons" (VEM). Here, R_{ref} represents a "reference distance" from the shower axis, and S_{ref} is the signal strength at that reference distance. The reference distance found to have the most robust measurement at these energies is 125 m [3], so S_{125} is the observable representing the "shower size".

Events in IceCube are reconstructed with a similar philosophy: the signals N_{PE}, measured in photoelectrons, are compared to an LDF which is a function of perpendicular

distance to the track d (described in detail in [4, 5, 6]):

$$N_{PE}(d, X, z) = A \left[\frac{a}{b}\left(e^{bX} - 1\right)\right]^{-\gamma_\mu} \frac{e^{-d/(c_{\rm ice}(z)\cdot\lambda_0)}}{\sqrt{(c_{\rm ice}(z)\cdot\lambda_0)d}}. \quad (2)$$

This function of d is dominated by the decaying exponential; the "slope" of this exponential is the attenuation length of light in the ice. Since the clarity of the ice changes due to well-measured horizontal dust layers [7, 8], this slope is treated as a bulk attenuation length λ_0 multiplied by a depth-dependent correction factor $c_{\rm ice}$ based on scattering length data measured at different depths z. The first term, containing the slant depth from the snow surface X, corrects for the ranging-out of muons as they penetrate deeper into the ice; the parameters a, b, and γ_μ in the first term are constants.

The overall normalization of this LDF scales with the energy deposited by muons in the detector, and this is parametrized with K_{70}, which is the expected signal (given by Equation (2)) evaluated using reference values of X = 1950 m, $c_{\rm ice} = 1$, and at a perpendicular distance d = 70 m. Since the track direction affects the signal expectation N_{PE} at all the DOMs (by changing d and X), the same likelihood function can also be used to find the track direction. These two reconstruction techniques (using surface signals to find the core position and S_{125} in IceTop, and using signals in IceCube to find the track direction and K_{70}) are used iteratively to find a reliable best-fit track.

3 Data, Simulation, and Event Selection

This analysis used data from August 2008, when the detector was in its 40-string/40-station configuration, for an overall detector livetime of 29.78 days. Because of unsimulated effects near the detector threshold due to snow buildup over tanks deployed before 2007, data from the subarray of IceTop deployed after 2007 were used. Monte Carlo simulated events were produced using the CORSIKA air shower generator [9] with the SIBYLL-2.1/FLUKA-2008 hadronic interaction models [10, 11], and an atmospheric model representing austral winter at the South Pole. Five particle species (proton, helium, oxygen, silicon, and iron) were generated according to an E^{-1} spectrum from 1 TeV to 46.4 PeV. The showers (3000 of them per species per third of a decade in energy) were generated uniformly over all azimuths and to a zenith angle of 65°, oversampled 100 times, and thrown over a circle of radius 1200 m centered on IceTop. The response of the IceTop tanks, the propagation of the high-energy muons through the ice to the depth of IceCube, the Cherenkov photons propagating to the DOMs, and the response of the DOMs themselves, are included in a detector simulation.

Quality cuts were applied to select those events which were well-reconstructed and contained within both the IceTop area and IceCube detector volume. Parameters such as track length and reconstructed effective propagation length (λ_0) were used to quantify reconstruction quality (see [6] for details). These cuts allow for a resolution (containing 68% of events) of better than 9 m in core position and less than 0.5° in track direction. The final event sample contains 239797 events from the August 2008 experimental data and 20289 total simulated events of five primary species.

4 Neural Network Mapping Technique

Once S_{125} and K_{70} have been reconstructed and quality cuts applied, simulations show that light and heavy nuclei are separated in this two-dimensional parameter space, as shown in Figure 1. The relation between the K_{70}-S_{125} space and the mass-energy space is non-linear, therefore a mapping technique is required to correlate one space to the other.

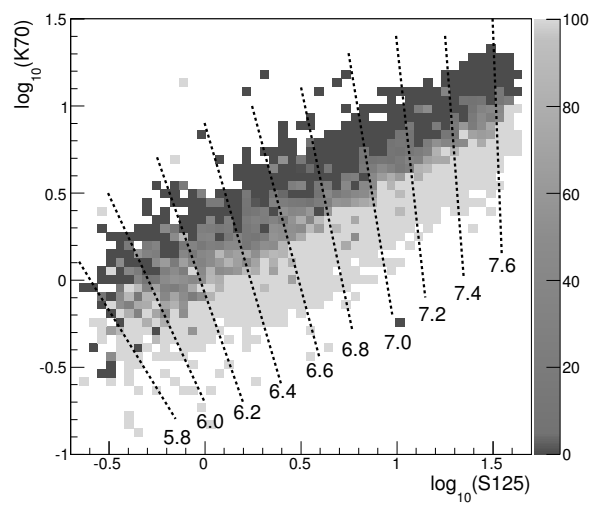

Figure 1: Fraction of each bin populated by protons (when only protons and iron are included in the sample). Dark grey indicates 100% iron, light grey indicates 100% protons; intermediate greys indicate overlapping populations. The dotted black lines approximating energy contours guide the eye for both nuclei.

A neural network was chosen for this work, which consists of a set of input parameters (in this case, K_{70} and S_{125}) which are connected to a set of output parameters (in this case, $\log_{10}(E)$ and $\ln(A)$) through a series of nodes which are arranged in layers. Each node is connected to other nodes in the previous and subsequent layer via a series of weights. At each node, an activation function acts on its input parameters as modified by the weights. Both the two inputs and the two outputs are renormalized so that they are numbers between zero and one.

The weights relating the inputs to the outputs are determined by "training" the network on a subsample of the Monte Carlo simulations (1/4 of the events) for which the true energy and true mass are known. Through a series of learning cycles, the network adjusts the weights to improve the accuracy of reconstructed outputs. A "testing" sample

(an independent 1/4 of the events) are put through the network after each learning cycle and the errors monitored to ensure that the network is not becoming too specific to the training events, or being "overtrained". The remaining half of the simulated data is known as the "analysis" sample and was used for the final steps described in section 6 below.

5 Energy Spectrum

For each event of experimental data, the neural network assigns a reconstructed energy and a reconstructed mass parameter. Reconstructed energies agree well with the true energies of simulated events; Figure 2 shows the energy resolution, and the reconstruction bias, as a function of energy.

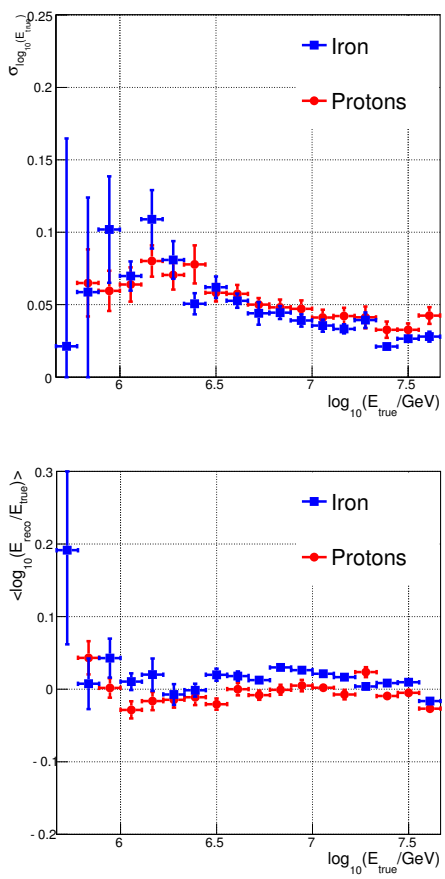

Figure 2: Upper: The energy resolution of the neural network output (sigma of distribution of $\log(E_{reco}) - \log(E_{true})$). Lower: The bias or misreconstruction of energy (mean of that distribution).

From these reconstructed energies, one can create an all-particle energy spectrum from experimental data. For a given flux Ψ as a function of energy E_0,

$$\Psi(E_0) = \frac{1}{\eta A \Omega \tau}\frac{dN}{dE} = \frac{1}{\eta A \Omega \tau}\frac{0.4343}{E_0}\frac{dN}{d\log_{10}(E_0)}, \quad (3)$$

where η is the efficiency (the ratio of simulated events left after all cuts to the number generated, which is a function of E_0), A is the area over which the CORSIKA showers were thrown, τ is the livetime of the detector (in this case 29.78 days), and Ω is the solid angle over which the events were generated. The resulting energy spectrum is shown in Figure 3.

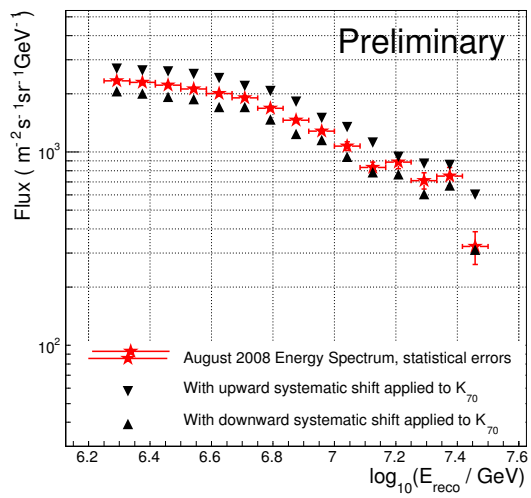

Figure 3: Measured all-particle flux as a function of particle energy, from August 2008 experimental data, with statistical error bars. Triangles indicate alternate spectra derived from data with K70's shifted up or down by 22.2% (see section 7).

6 Mass Composition

Within each slice in energy and for each simulated species, the neural network produces a distribution of mass outputs which is called a "template histogram". Examples of template histograms for three kinds of primaries are shown in Figure 4, for one slice in energy as an example. Data, when put through the same neural network, also has a histogram of outputs which can be decomposed into a linear combination of the template histograms of the individual species (proton, oxygen, etc.). A minimizer finds the optimal mixture of simulated species to match the data.

Proton and iron template histograms alone are not sufficient to reproduce the data, and so intermediate nuclei are necessary. Because there is a great deal of overlap between the template histograms of all five nuclei, we matched the data to a combination of three template histograms: protons, iron, and "intermediate nuclei" (which is a 50-50 mixture of helium and oxygen). When this procedure is applied to a "hand-mixed" sample of Monte Carlo events (treating the sample like data, with different $\ln(A)$ at different energies), the fit found mixtures which correctly reproduced the $\ln(A)$ at all energies. When the procedure was applied to

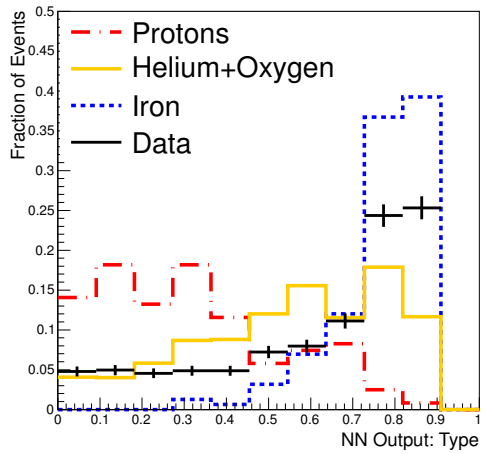

Figure 4: Three "template histograms": protons, iron, and a 50-50 mixture of helium and oxygen. The energy bin shown here is $\log_{10}(E/\mathrm{GeV})$ from 6.9 to 7.1.

experimental data from August 2008, the $\ln(A)$ as a function of energy was computed and is shown in Figure 5.

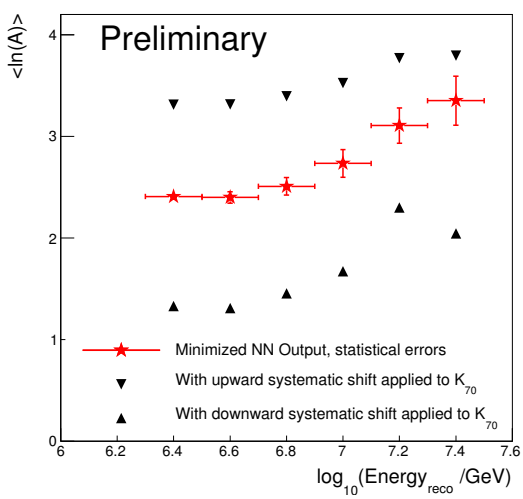

Figure 5: Measured $\ln(A)$ as a function of reconstructed energy, with statistical error bars. Triangles indicate alternate results if K70 is shifted up or down by 22.2%.

7 Systematic Errors

Both Figures 3 and 5 include estimates of the systematic error due to a variety of effects:

- *Hadronic Interaction Model:* Samples of events simulated with both EPOS-1.99 [12] and QGSJET-II-03 [13] were generated for comparison with SIBYLL. *Percent error in K_{70}: 9.7%*
- *Ice Model:* Since K_{70} depends on the propagation of photons through the ice, the effect of two different models of the attenuation of light in dust layers (known as AHA [7] and SPICE [8]) were investigated. *Percent error in K_{70}: 9.7%*
- *DOM Efficiency:* The efficiency of the DOMs in IceCube depends upon a number of factors, which have been measured in a controlled setting [14]. *Percent error in K_{70}: 8%*
- *Errors introduced from corrections:* The Monte Carlo simulation used for this work did not include two relevant effects: a recent improvement of the parameterization of the light yield from muon bundles in IceCube, and the accumulation of snow on the surface above IceTop. The effects were quantified and corrected for, but some error due to the application of this correction was estimated. *Percent error in K_{70}: 14.8% and 4.7%, respectively*

The total systematic shift in K_{70} (added in quadrature) is 22.2%. The effect of these systematics on the final results (i.e. the spectrum in Figure 3 and the mass composition in Figure 5) were studied by applying these errors as shifts to the input parameters of the neural network (i.e. K_{70}) before it goes through the neural network, and seeing how the output parameters, and any analysis downstream of the neural network, changes. Both of these figures show alternative results with such a shift (both up and down) applied. If improved simulations eliminate the errors introduced from corrections, the total systematic error could be substantially reduced.

References

[1] H. Kolanoski, IceCube summary talk, these proceedings.
[2] The IceCube Collaboration, paper 807, these proceedings.
[3] S. Klepser, PhD thesis, Humboldt Univ, Berlin (2008)
[4] K. Rawlins, PhD thesis, Univ. of Wisconsin-Madison (2001)
[5] J. Ahrens et al., *Astropart. Phys.* **21** (2004) 565-581.
[6] K. Andeen, PhD thesis, Univ. of Wisconsin-Madison (2011)
[7] M. Ackermann et al., *J. Geophys. Res.*, **11** (2006)
[8] "Study of South Pole ice transparency with IceCube flashers" (The IceCube Collaboration), to be published.
[9] D. Heck, et al., *Forschungszentrum Karlsruhe Report FZKA 6019* (1998)
[10] E. J. Ahn et al. *Phys. Rev. D* **80** (2009) 94003.
[11] G. Battistoni et al., *AIP Conf. Proc.*, **896** (2007) 31.
[12] K. Werner *Nucl. Phys. B Proc. Suppl.*, **175** (2007) 81.
[13] N. N. Kalmykov, S. S. Ostapchenko and A.I. Pavlov, *Nucl. Phys. B Proc. Suppl.*, **52** (1997) 17.
[14] R Abbasi et al., *Nucl. Inst. and Methods in Phys. Res. Section A*, **618** (2010) 139.

Seasonal Variations of High Energy Cosmic Ray Muons Observed by the IceCube Observatory as a Probe of Kaon/Pion Ratio

THE ICECUBE COLLABORATION[1]
[1]*See special section in these proceedings*

Abstract: The high statistics of cosmic ray induced muon events detected by the IceCube Observatory makes it possible to study the correlation of muon intensity with the stratospheric temperature over Antarctica with high precision. Using 150 billion events collected by IceCube experiment over 4 years, the muon rate was found to be highly correlated with daily variations of the stratospheric temperature and exhibits a $\pm$ 8% annual modulation. The correlation between the muon rate and the upper atmospheric temperature is related to the relative contribution of π and K to the production of muons. Therefore it is possible to estimate the K/π ratio from the seasonal variation of the muon rate, which was found to be 0.09 $\pm$ 0.04 at cosmic ray median energy of about 20 TeV.

Corresponding authors: P. Desiati[1], T. Kuwabara[2], T.K. Gaisser[2], S. Tilav[2], D. Rocco[1]
[1]*IceCube Research Center and Dept. of Physics, University of Wisconsin, Madison, WI 53706, U.S.A.*
[2]*Bartol Research Institute and Dept. of Physics and Astronomy, University of Delaware, Newark, DE 19716, U.S.A.*

Keywords: cosmic muons, seasonal modulation, IceCube

1 Introduction

When cosmic ray particles enter the Earth's atmosphere, they generate a hadronic cascade in which mesons are produced, primarily pions and kaons. These mesons can either interact again or decay into muons. The relative probability of decay or interaction depends on the local density of the atmosphere, which in turn depends on the temperature [1]. The differential flux of muons with energies larger than 100 GeV can be described with good approximation as [2]

$$\phi_\mu(E_\mu,\theta) = \phi_N(E_\mu) \times \left\{ \frac{A_{\pi\mu}}{1 + B_{\pi\mu}\cos\theta^\star\, E_\mu/\epsilon_\pi} + \frac{A_{K\mu}}{1 + B_{K\mu}\cos\theta^\star\, E_\mu/\epsilon_K} \right\}, \quad (1)$$

where $\phi_N(E_\mu)$ is the primary spectrum of nucleons (N) evaluated at the energy of the muon. The first term in Eq. 1 corresponds to muon production from leptonic and semileptonic decays of pions, while the second term is related to kaons. The constants $A_{\pi\mu}$ and $A_{K\mu}$ include the branching ratio for meson decay into muons, the spectrum weighted moments of the cross section for a nucleon to produce secondary mesons, and those of the meson decay distribution. The denominators in Eq. 1 reflects the competition between decay and interaction of secondary mesons in the atmosphere. When $E_{\pi,K} < \epsilon_{\pi,K}/\cos\theta^\star$, the meson decay is the dominant process, and muons are produced with the same spectral index as the parent cosmic rays. At high energy meson interaction dominates and the corresponding muon spectrum becomes one power steeper than the primary spectrum. The characteristic critical energies $\epsilon_{\pi,K}$ at a given atmospheric depth are inversely proportional to the atmosphere's density at that point, and therefore are affected by temperature variations. In an isothermal approximation of the atmosphere, the density is described by an exponential with a scale height of $h_\circ \approx 6.19$ km (over Antarctica). The numerical value applies to the lower stratosphere, where most of the muons are generated. In this approximation $\epsilon_{\pi,K}$ are proportional to the atmosphere's temperature in the perfect gas state limit. At a mean atmospheric temperature of $T_\circ = 211°$K the critical energies are $\epsilon_\pi = 111$ GeV and $\epsilon_K = 823$ GeV. The dependence of the critical energies on temperature is the main source of the seasonal variation in muon rate. This modulation was studied by underground experiments such as MACRO [3], LVD [4] and MINOS [5], and by AMANDA [6] and IceCube [7]. Here we update the analysis with four years of IceCube data with an emphasis on the systematic effects that can be studied with a very large amount of data.

2 Temperature Correlation

The relation between the variation of temperature and the variation of muon intensity at a particular energy and zenith angle can be expressed in terms of a theoretical correlation

coefficient calculated from Eq. 1 as

$$\alpha_\mu(E_\mu,\theta) = \frac{T}{\phi_\mu(E_\mu,\theta)}\frac{\partial\phi_\mu(E_\mu,\theta)}{\partial T}, \qquad (2)$$

which depends explicitly on the characteristic critical energies $\epsilon_{\pi,K}$.

Measured rates depend on the convolution of the muon differential spectrum with the detector response, which depends on muon energy and zenith angle. To compare with measurements, it is therefore necessary to calculate a weighted correlation coefficient as

$$\alpha_T^{th}(\theta) = \frac{T\cdot\frac{\partial}{\partial T}\int dE_\mu\,\phi_\mu(E_\mu,\theta)\,A_{eff}(E_\mu,\theta)}{\int dE_\mu\,\phi_\mu(E_\mu,\theta)\,A_{eff}(E_\mu,\theta)}, \qquad (3)$$

where $A_{eff}(E_\mu,\theta)$ is the effective detector area obtained from simulation. Eq. 3 defines the correlation coefficient for a particular zenith angle θ. The total correlation coefficient is then obtained by averaging $\alpha_T^{th}(\theta)$ over θ with a weight given by the observed event angular distribution. With this definition the variation in muon intensity I_μ is given by

$$\frac{\Delta I_\mu}{I_\mu} = \alpha_T^{th}\,\frac{\Delta T_{eff}}{T_{eff}}, \qquad (4)$$

where T_{eff} is the effective atmospheric temperature as defined below. Since the rate R_μ of observed muons is proportional to the incident muon intensity I_μ, it is correlated with the effective temperature as well

$$\frac{\Delta R_\mu}{\langle R_\mu\rangle} = \alpha_T^{exp}\,\frac{\Delta T_{eff}}{\langle T_{eff}\rangle}, \qquad (5)$$

where α_T^{exp} is the experimentally determined correlation coefficient.

Since muon production occurs over an extended portion of the upper atmosphere and the temperature depends on altitude, it is necessary to define a parameter referred to as effective temperature, in order to quantify the relationship between variations in temperature and those in measured muon rate.

The pion and kaon terms in Eq. 1 are derived from the integral over the atmospheric slant depth X (in g/cm^2) of the muon production spectrum $P_\mu(E_\mu,\theta,X)$, which in turn is given by the probability distribution for meson decay to muons integrated over the parent meson spectrum [2].

The effective temperature as a function of muon energy and zenith angle is defined as the actual temperature profile weighted by the muon production spectrum

$$T_{eff}(E_\mu,\theta) = \frac{\int dX\,P_\mu(E_\mu,\theta,X)T(X)}{\int dX\,P_\mu(E_\mu,\theta,X)}, \qquad (6)$$

where $P_\mu(E_\mu,\theta,X)$ is the sum of muon production spectrum from pion and kaon contributions. The rationale for this definition is that the depth dependence of the muon production spectrum weights the temperature with the regions of the atmosphere where the meson decay to muons occurs. The critical energies that appear in the production spectrum are evaluated at the mean temperature, $T_\circ$, but the production profile does not depend strongly on temperature.

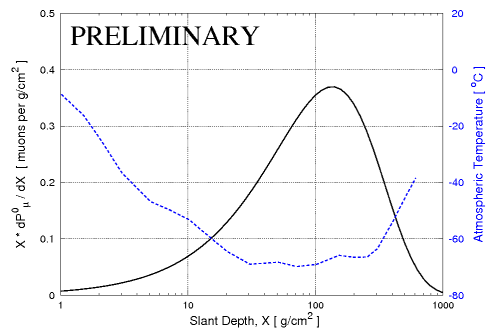

Figure 1: The differential weighting function used in the calculation of the T_{eff}, as a function of atmospheric depth X (continuous line), superimposed on the average atmospheric temperature profile (dashed line).

This formulation of the effective temperature differs from that in Grashorn et al. [8], where the low energy limit of the temperature derivative of muon production spectrum produces an unphysical discontinuity. The IceCube observatory is located at a depth of >1.3 km.w.e./cosθ so only muons with energies above about 400 GeV/cosθ can reach and trigger the detector. At these energies muon decay and energy loss in the atmosphere are negligible. This enables us to use analytic forms for muon production analogous to Eq. 1 without accounting for decay and energy loss of muons in the atmosphere and hence to obtain a physically correct result without any discontinuity.

To compare predictions with measurements it is necessary to determine the convolution with the detector response function

$$T_{eff}(\theta) = \frac{\int E_\mu\,\int dX\,P_\mu(E_\mu,\theta,X)\,A_{eff}(E_\mu,\theta)\,T(X)}{\int E_\mu\,\int dX\,P_\mu(E_\mu,\theta,X)\,A_{eff}(E_\mu,\theta)}, \qquad (7)$$

where the denominator, as in Eq. 3, is the total measured muon intensity. As for the correlation coefficient, the total effective temperature T_{eff} is the weighted average of Eq. 7 over the event zenith distribution. Fig. 1 shows the differential weighting function used in the calculation of the effective temperature along with the average atmospheric temperature profile over the seasons. It peaks at about 100 g/cm^2, which is where most of the muons are produced.

3 Muon and Temperature Data

In this analysis we used 150 billion muon events collected by the partially completed IceCube Observatory from March 2007 to April 2011 (see [9] for an overview on IceCube). These events are generated by cosmic rays with median energy of about 20 TeV.

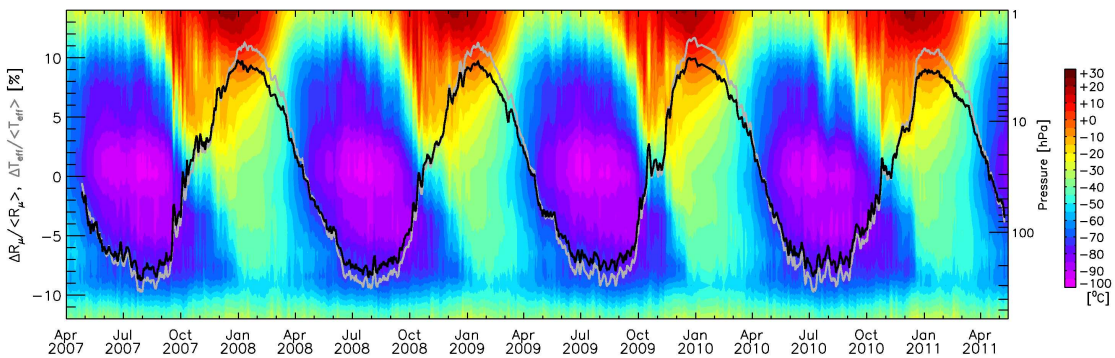

Figure 2: The daily atmospheric temperature profiles over Antarctica produced by NASA AIRS instrument on board the Aqua satellite [10] are shown from 2007 to 2011 (in color code), along with the relative modulation in the measured muon event rate (black line) and the relative variation of the effective temperature (grey line). Note that the statistical uncertainties in the data are between about 0.1 Hz (in 2007) and about 0.16 Hz (in 2011) on the daily rates. The corresponding uncertainties on the relative rate variations are 0.02 % and 0.008 %, respectively.

The muon rate increased substantially over these four years as new detectors were added during each construction season. As the instrumented volume increased, the probability that one data record included two or more separate cosmic-ray events increased from about 1% to about 4%. A correction to the daily recorded rate was therefore applied to obtain a corrected rate of muon events, R_μ.

The atmospheric temperature profile data used in this analysis were collected by the NASA Atmospheric Infrared Sounder (AIRS) on board the Aqua satellite. Daily atmospheric temperatures at 20 different pressure levels from 1 to 600hPa above the South Pole were obtained from the AIRS Level 3 Daily Gridded Product available on NASA Goddard Earth Sciences, Data and Information Services Center (GES DISC) [10]. Using these data the daily effective temperature T_{eff} was calculated based on the zenith-weighted average of Eq. 7.

4 Results and Determination of K/π Ratio

Fig. 2 shows the measured $\frac{\Delta R_\mu}{\langle R_\mu \rangle}$ as a black continuous line along with $\frac{\Delta T_{eff}}{\langle T_{eff} \rangle}$ as a black dashed line. The figure also shows the actual atmospheric temperature profile as a function of pressure level (equivalent to atmospheric depth X). The statistical uncertainties in the measured muon rate are too small to show in the figure. Note that besides the large seasonal modulation, the daily muon rate is strongly correlated with short time temperature variations in the upper atmosphere.

Based on Eq. 5, the experimental temperature coefficient was determined from regression analysis and found to be $\alpha_T^{exp} = 0.860 \pm 0.002$ (stat.) $\pm$ 0.010 (syst.). The experimental systematic uncertainty on α_T^{exp} is dominated by the effective area $A_{eff}(E_\mu, \theta)$, which is used in the calculation of the effective temperature and of the theoretical correlation coefficient in Eq. 3. Most of the detected muons range out within the large instrumented volume of IceCube, and the energy profile of the effective area depends on the distribution of depths the muons reach within the array. The spread on this distribution, translates into an estimated uncertainty in the experimental correlation coefficient of 0.01.

Since the temperature correlation coefficient depends on the relative contribution of pions and kaons, it is possible to use the seasonal variations of the muon rate to determine the K/π ratio.

The effective temperature T_{eff} is relatively insensitive to variations in the cosmic ray spectral index, the proton attenuation length, the critical energies and K/π ratio because the dependence cancels to a large extent due to the normalization in Eq. 7.

The theoretical correlation coefficient α_T^{th}, on the other hand, depends primarily on the critical energies and on the K/π ratio. Changing the cosmic ray spectral index and proton attenuation length within a wide range, has an effect smaller than 1%. Therefore it is possible to use the parameters for attenuation lengths and spectrum weighted moments from Ref. [2], assuming a cosmic ray spectral index of -2.7. The critical energies evaluated at the average effective temperature of $T_\circ = 211°$K are used.

In particular, the kaon to pion ratio $R_{K/\pi} = \frac{Z_{NK}}{Z_{N\pi}}$ depends on the spectrum weighted moments Z_{NK} and $Z_{N\pi}$ of the cross section for a nucleon N to produce secondary kaons and pions, respectively, from a target nucleus in the atmosphere. The dependence on the spectrum weighted moments Z_{NK} and $Z_{N\pi}$ is implicit in the parameters $A_{\pi\mu}$ and $A_{K\mu}$ in Eqs. 1, 3, 7.

The nominal value of K/π ratio is taken to be [2]

$$R_{K/\pi} = \frac{0.0118}{0.079} = 0.149 \pm 0.060, \qquad (8)$$

which is based on laboratory measurements below 100 GeV center of mass energy. The 40% uncertainty corresponds to that in the current cosmic ray interaction models [11].

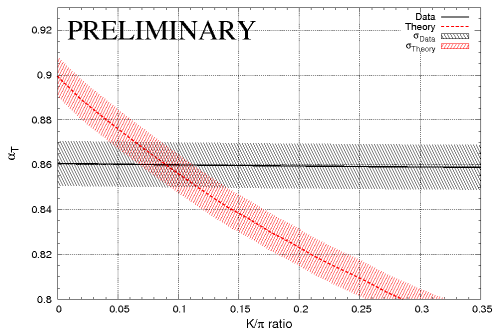

Figure 3: The preliminary α_T^{exp} determined by IceCube as a function of the K/π ratio (continuous line), with its error given by the band, and the predicted α_T^{th} (dashed line) with the corresponding error given by the band. The intersection region between the two bands is at $R_{K/\pi} = 0.09 \pm 0.04$.

By calculating the theoretical correlation coefficient α_T^{th} as a function of $R_{K/\pi}$ and comparing it with the experimental value, it is possible to measure the kaon to pion ratio for proton interaction with atmospheric nuclei (mainly nitrogen) at cosmic ray particle energy of 20 TeV.

Fig. 3 shows the experimental and theoretical values of α_T as a function of K/π ratio for the IceCube data. While, as mentioned above, α_T^{exp} is almost insensitive to $R_{K/\pi}$, the value of α_T^{th} has a strong dependence. Since the statistical uncertainties are very small, the band on α_T^{exp} is dominated by systematic uncertainties. The band on α_T^{th} reflects the theoretical uncertainties in the calculation of the correlation coefficient mentioned above, and conservatively estimated to be 1%. The crossover in Fig. 3 is at $R_{K/\pi} = 0.09 \pm 0.04$. Fig. 4 shows a comparison of the IceCube measurement with other observations.

5 Conclusions

Using 150 billion cosmic ray induced muon events collected in four years by IceCube, a strong correlation of the daily observed muon rate with the stratospheric temperature was observed, along with a $\pm 8\%$ annual modulation. The K/π ratio at 20 TeV cosmic ray energies was determined by comparing the observed temperature correlation coefficient with the theoretical one, and found to be $R_{K/\pi} = 0.09 \pm 0.04$.

The value obtained with IceCube implies that $Z_{NK} \sim 0.0071$, which is about 40% lower than its nominal value from Ref. [2]. In calculating the theoretical correlation coefficient the sum $Z_{NK} + Z_{N\pi}$ was kept constant to its nominal value 0.0908. One way to reconcile the measurement of $R_{K/\pi}$ with other results is by reducing the amount of associated production $pN \rightarrow nK^+$. Keeping the nominal value of $Z_{NK^-} = 0.0028$, while reducing Z_{pK^+} from its nominal value of 0.0090 to 0.0043 is also likely to give a better agreement with recent measurements of the ratio of

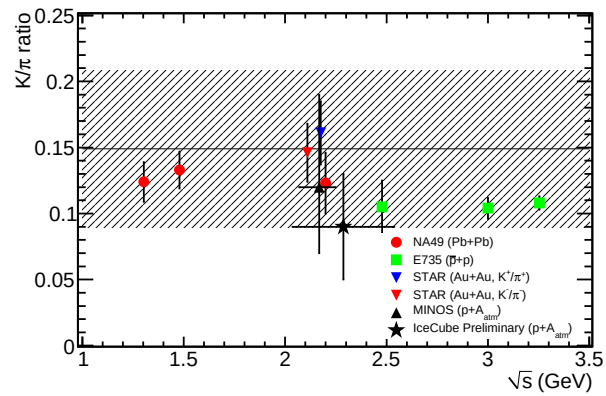

Figure 4: A compilation of selected measurements of K/π for various center of mass energies. Data points are from NA49 [12, 13], E735 [14], STAR [15] and MINOS [5]. The horizontal line and gray band represents the reference value K/π ratio 0.149 ± 0.060 [2, 11].

the atmospheric muon charge ratio from MINOS [16] and OPERA [17].

6 Acknowledgements

The temperature data used in this study were acquired as part of the NASA's Earth-Sun System Division and archived and distributed by the Goddard Earth Sciences (GES) Data and Information Services Center (DISC) Distributed Active Archive Center (DAAC).

References

[1] P.H. Barret, *et al.*, Rev. Mod. Phys., 1952, **24**(3), 133.
[2] T.K. Gaisser, 1990, Cosmic Rays and Particle Physics, ed. CUP
[3] M. Ambrosio, *et al.*, Astrop. Phys., 1997, **7**, 109.
[4] M. Selvi, Proc. of 31st ICRC, 2009, Łòdż, Poland.
[5] P. Adamson, *et al.*, Phys.Rev., 2010, **D81**,01200.
[6] A. Bouchta, Proc. of 26th ICRC, 1999, Salt Lake City, UT, U.S.A.
[7] S. Tilav, *et al.*, Proc. of 31st ICRC, 2009, Łòdż, Poland, arXiv:1001.0776.
[8] E.W. Grashorn, *et al.*, Astrop. Phys., 2010, **33**, 140.
[9] H. Kolanoski, IceCube summary talk, these proceedings.
[10] http://disc.sci.gsfc.nasa.gov/AIRS/data-holdings.
[11] G.D. Barr, *et al.*, Phys. Rev., 2006, **D74**, 094009.
[12] S.V. Afanasiev, *et al.*, Phys. Rev., 2004, **C66**, 054902.
[13] C. Alt, *et al.*, Eur. Phys. J. C, 2006, **45**, 343.
[14] T. Alexopoulos, *et al.*, Phys. Rev., 1993, **D48**, 984.
[15] C. Adler, *et al.*, Phys .Lett., 2004, **B595**, 143.
[16] P. Adamson, *et al.*, Phys. Rev., 2007, **D76**, 052003.
[17] N. Agafonova, *et al.*, 2010, arXiv:1003.1907.

Measurements of the Air Shower Parameters with IceTop

THE ICECUBE COLLABORATION[1]
[1]*See special sections in these proceedings*

Abstract: We study the lateral distribution function (LDF) of signals in the IceTop air shower detector as a function of distance from the air shower core. The completed IceTop detector consists of 81 stations with two tanks each. It can now study the signals at distances approaching 1 km from the core position. We discuss the general shape of lateral distributions of the signal and its dependence on the shower zenith angle and primary mass. We also show the simulated individual tank signal lateral distribution for a large number of simulated proton and iron showers. We find that the form of the lateral distribution function used for more widely spaced arrays of water Cherenkov detectors, Haverah Park and Auger in the EeV range, can also be used with appropriate parameters to describe IceTop data in the 10-100 PeV range.

Corresponding authors: Shahid Hussain[2] (*shahid@bartol.udel.edu*), Todor Stanev[2] (*stanev@bartol.udel.edu*), Serap Tilav[2] (*tilav@udel.edu*)
[2]*University of Delaware, Newark, DE 19716, U.S.A.*

Keywords: IceCube, IceTop, lateral distributions

1 Introduction

IceTop, the surface air shower array above the IceCube neutrino detector, was completed in the 2010/2011 deployment season. IceTop consists of 81 stations, each of which has 2 tanks of area 2.7 m^2 containing 90 cm of clear ice. The average distance between the tanks in a station is 10 m and the average distance between stations is 125 m. The Cherenkov light generated by the charged particles that hit the tanks is collected by two digital optical modules (DOMs) that run at different gains to increase the dynamic range. The signal strength is measured in vertical equivalent muon units (VEM), i.e. the signal that a 1 GeV vertical muon produces in the tank. A station triggers when there are signals above the threshold (0.16 VEM) in both tanks within one microsecond. In this way we avoid triggering on coincidental muons that belong to different atmospheric cascades.

The current shower reconstruction of IceTop events is based on a procedure which was designed when the array contained only 26 stations in a much smaller area [1]; the reconstruction procedure is applied to showers that trigger at least five stations. The signal lateral distribution function in this procedure does not include tanks with zero signal (i.e. tanks that do not trigger) and the fitting routine accounts for these tanks with a separate, no-hit probability, term in the likelihood function.

In this paper we instead use a lateral distribution function of the form [2]

$$S(r) = A \times r^{-(\eta + r/r_0)}, \tag{1}$$

where $S(r)$ is the signal at a perpendicular distance r from the shower core in shower coordinates; η, r_0, and A are fit parameters. This form has been used for Haverah Park [3] and Auger [4] to fit showers observed with water Cherenkov tanks. IceTop is at a much higher altitude (2835 m) than HP (sea level) and significantly higher than Auger (1400 m) and collects data in a different primary energy range with detectors spaced by 125 m as compared to several hundred meters for HP and 1500 m for Auger. We investigate here the extent to which the lateral distribution form used for the other Cherenkov shower detectors scale to the location and energy range of IceTop. Everywhere in this paper, S(r) gives the signal strength at a perpendicular distance r from the shower core in shower coordinates. We include tanks with and without a signal directly in the lateral fit, both for simulated and observed air showers.

2 Monte Carlo Calculation

To study the lateral distribution we have simulated air showers initiated by protons and iron nuclei with fixed primary energies of 10 and 100 PeV and fixed zenith angles of 0, 25, and 45 degrees. Air showers are simulated with CORSIKA-SIBYLL [5] and the detector simulation uses Geant4 [6] for the tank response. 50 showers per primary

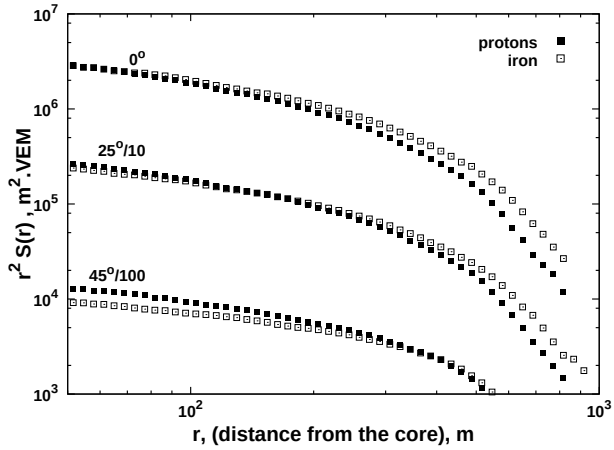

Figure 1: LDF of the signal strengths (weighted by square of the distance from core) for 100 PeV simulated proton and iron showers at three zenith angles.

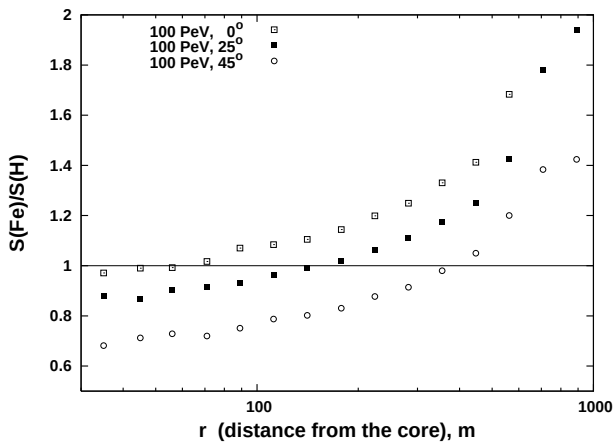

Figure 2: Ratio of the signal strength in simulated iron to proton showers for three zenith angles.

type, energy, and zenith angle were dropped on the IceTop array 100 times each within a 600 meter radius from the array center. As a result, there are 5,000 showers in each set. The simulated showers were reconstructed with the current standard procedure and all results presented below use the reconstructed shower core position, direction, and shower energy for event selection. Fewer than 200 showers in each set were not reconstructed well and are not analyzed here.

Figure 1 shows the average LDF of the IceTop signals for simulated proton and iron initiated showers at the three zenith angles. As expected, the proton showers have higher signals close to the shower core and iron showers have higher signal density at large distances from the core[1]. The intersection point of the proton and iron signals LDF changes with zenith angle and increases significantly even at the modest zenith angle of 45 degrees. The ratio of iron to proton signal LDF is presented in Figure 2. While for strictly vertical showers the intersection point is at about 50 m from the shower core; it is between 120 and 150 m

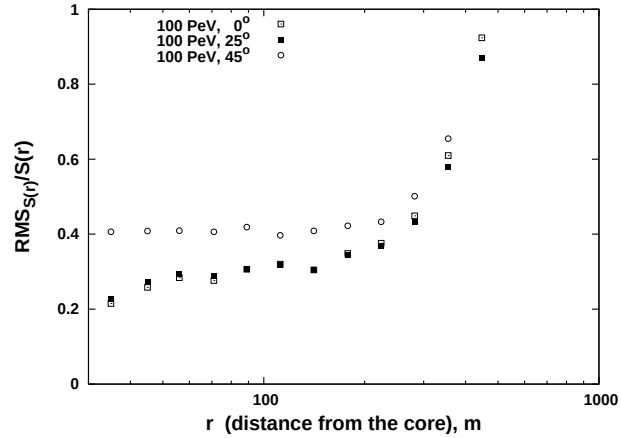

Figure 3: The ratio of RMS of the signal to its strength in simulated 100 PeV proton showers at three different zenith angles.

away from the core for θ=25 degrees and above 300 m at 45 degrees. Furthermore, although not shown here, the intersection point for 10 PeV showers is relatively larger for each angle; it is around 130, 180, and 400 m for θ=0, 25, and 45 degrees, respectively. The IceTop reconstruction procedure currently uses the signal at 125 m, S_{125}, from the shower core as the energy-related parameter, which seems to be mass independent for showers near the peak of the angular response for IceTop (25 degrees) as the classical papers of A.M. Hillas [7] recommend. However, as we see in Figure 2 for IceTop, there is no single distance from the shower core that is independent of mass for all energies and angles. Minimizing the fluctuations is also desirable in the choice of an optimum distance r used for energy assignment. Figure 3 shows the ratio of RMS$_S/S(r)$ for E = 100 PeV proton showers and the three angles. The signal fluctuations are almost constant between 50 m and 150 m from the shower core for all three angles. The fluctuations are higher for the most inclined showers and still constant below 150 m distance from the core. the goal is to apply the lateral distribution function to experimental data which may include a mixture of proton, iron, and several other primaries. Therefore, it is instructive to look at the VEM range of signals for a given primary energy for both proton and iron together. As an example, we show in Fig. 4 the signals measured by IceTop in 100 proton and 100 simulated showers of primary iron nuclei. At distances around 100 m the signal variation is slightly larger than a factor of two. At much larger distances, around 500 m, the signal variation increases to more than one order of magnitude. A fraction of these fluctuations is due to the fact that we plot proton and iron induced showers together. There is a strong increase in fluctuations for each species at distances greater than 300 m, as shown in Fig. 3. Note also the relatively small statistics at distances below 100 m.

1. Everywhere in this paper, distance from the core is the perpendicular distance from the core in shower coordinates.

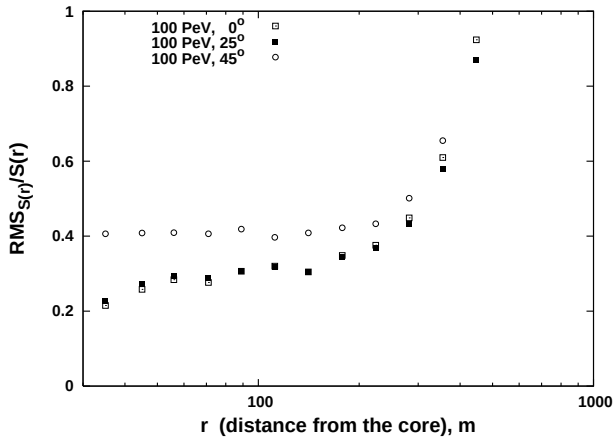

Figure 4: The signals recorded by all non-zero tanks for 100 proton and 100 iron induced vertical showers of energy 100 PeV are plotted as a function of the distance to shower core.

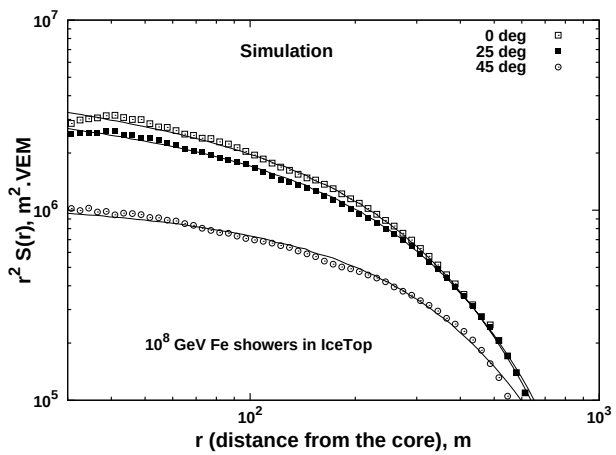

Figure 5: The average LDF of the signal strength for 100 PeV simulated iron showers at three zenith angles fitted with the HP-like function.

3 Fitting the simulated signal LDF

Both HP and Auger have fitted their data with a lateral distribution function similar to Eq. 1 r_0 fixed. Here we fit the average of the simulated showers at each energy with the same form. As an illustration, the signal LDF of the simulated 100 PeV iron showers and the fits obtained are shown in Fig. 5. As expected, the lateral distribution becomes flatter with angle. The parameter η is 2.22, 2.21, and 2.06 for 0, 25, and 45 degrees, respectively. The respective r_0 values are 1410, 1507 and 1783 m. The respective normalization parameter A is 7.18×10^6, 5.31×10^6, and 1.25×10^6 VEM. The χ^2 values of all fits are smaller than 1 per degree of freedom.

The fits of simulated proton showers have similar results. The η values are 2.25, 2.22, and 2.10 for 0, 25, and 45 degrees, respectively. The respective r_0 values are 1215, 1280 and 1474 m. While η values are similar for proton and iron showers, the r_0 values are always significantly smaller by about 200 m than those of iron showers. The respective normalization parameter A is 8.58×10^6 , 7.29×10^6, and 2.02×10^6 VEM for proton showers.

One has to note that the fits are not very good for core distances less than about 50 m. The reason is that we are using reconstructed position of the shower core. The average error in the core position is less than 20 m but this error still affects the LDF at small distances in a negative way. The statistics at small distances is also low. For these reasons the measured or interpolated signal strengths at small distances are not reliable.

4 Fitting of individual showers

The next step in the study of the signal lateral distribution function is the fitting of individual showers. We have attempted to fit individual simulated and experimentally detected showers with the function of Eq. 1. The fitting procedure is less stable when applied to individual showers especially because there are usually few points at distances smaller than 100 m from the shower core. This makes the r_0 parameter vary even more than in the case of average lateral distribution from a large number of showers.

The well fitted showers, however, show a good agreement between the experimentally detected and the simulated showers. To compare these two sets of showers we chose experimental showers with standard IceTop reconstructed parameters very close to the simulated (fixed primary energy E_p and zenith angle θ) ones. For vertical showers, for example, we chose showers with $\cos(\theta) \geq 0.95$ and with $1.97 \leq \log_{10}(E_p/\mathrm{PeV}) \leq 2.03$. Figure 6 shows the LDF fit of a simulated proton (top) and an experimentally detected shower (bottom). Both showers have a large number of triggering stations - 48 stations in the simulated shower and 46 in the experimental one. The experimental shower shown in Fig. 6 is from 2010 when IceTop consisted of 73 stations (or 146 tanks). The tanks with '0' signal are not shown, but they are included in the average for each annular bin of r. In the graph of the experimental shower we also show the average signal strength calculated in logarithmic radial bins around the reconstructed shower core.

The fits have a χ^2 of 0.6 p.d.f. However, the performance of the fit will depend on χ^2 distributions from fits on a reasonable sample of showers; a detailed study is needed in this regard.

5 Summary

We have studied the lateral distribution of air shower signals in IceTop tanks using a function similar to the one used by Haverah Park and Auger Observatory. Tanks with signals below threshold are included as zeros in averaging the signal in each radial bin. The simulated proton and iron showers at 10 and 100 PeV can be described with lateral

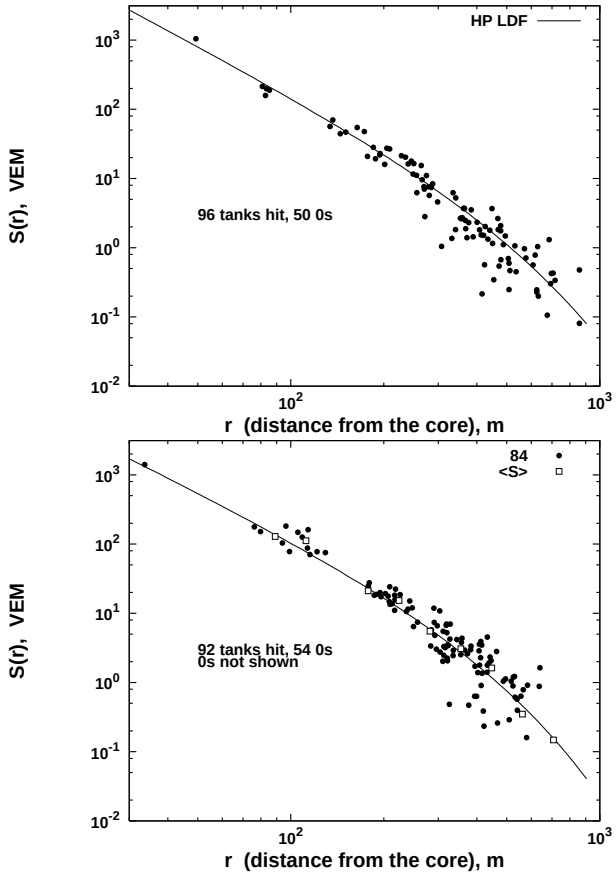

Figure 6: Example fits on two individual showers; both showers are almost vertical ($\cos(\theta)\geq$0.95) with energies close to 100 PeV. Top: a simulated proton shower. Bottom: experimentally observed shower.

distribution functions of the VEM signal having the same form as those used by the Haverah Park and Auger Observatory. We have not studied the lateral distribution of signal at distances smaller than 50 m because the lateral distance and the uncertainty in the reconstructed core position become comparable to each other; this results in a large uncertainy in the signal at shorter distances. The LDF of both iron and proton showers becomes flatter with increasing zenith angle.

We also see, as expected, the flatter lateral distribution of the simulated iron showers compared to that of the proton showers. The highest ratio of the iron to proton LDF occurs at distances more than 500 m from the shower core. We also show the distance at which the relative signal strengths of the signals from proton and iron showers are equal. the crossover radius depends significantly on the shower zenith angle and also on energy. For 100 PeV showers, it varies between 50-150 m for zenith angles as large as 25 degrees, and it is above 300 m at 45 degrees. For 10 PeV showers, not shown here, it varies between 130-180 m for zenith angles as large as 25 degrees, and it is above 400 m at 45 degrees. For a mass independent energy reconstruction in this energy range, we will explore the possibility of scaling the energy estimation reference distance, with the energy and zenith angle of the shower using an iterative procedure. In this regard, it is encouraging that, for showers in the peak of the angular distribution for IceTop (θ $\sim$25 degrees) and energies 10-100 PeV, the variation of the iron to proton signal ratio is around 1 and it has about 10$\%$ variation for the reference distance range of 100-150 m. It is also encouraging that the signal fluctuations are almost constant in the distance range 50-150 m.

References

[1] S. Klepser, PhD thesis, Humboldt Univ, Berlin (2008).

[2] D. Newton, J. Knapp & A.A. Watson, Astropart. Phys. **26**, 414 (2007).

[3] M.A. Lawrence, R.J. Reid, and A.A. Watson, J.Phys.G **G17**, 733 (1991).

[4] J. Abraham et al. (Pierre Auger Collaboration), Phys. Rev. Lett.**101**:061101, arXiv:0806.4302 (2008).

[5] http://www-ik.fzk.de/corsika/.

[6] http://www.geant4.org/geant4/.

[7] A.M. Hillas,Proceedings of the 11th ICRC, Budapest, Hungary (1969); Hillas, A. M.; Marsden, D. J.; Hollows, J. D.; Hunter, H. W., Proceedings of the 12 ICRC, Hobart, Australia (1971).

Extensive Air Showers Measured by the 79-string IceCube Observatory at South Pole

THE ICECUBE COLLABORATION[1]
[1] *See special section in these proceedings*

Abstract: The IceCube Neutrino Observatory was completed in the 2010-11 Antarctic season with 86 deep strings and 81 surface stations. Between June 2010 and May 2011 IceCube collected high quality data with 73 stations and 79 strings. The performance of the detector as an air shower array to contribute to our understanding of the cosmic ray spectrum from the knee region up to 1 EeV will be demonstrated. The sensitivity to primary composition using high energy muon bundles seen by the IceCube array will also be discussed.

Corresponding authors: T. Feusels[2] (*tom.feusels@ugent.be*), S. Tilav[3] (*tilav@udel.edu*)
[2]*Dept. of Physics and Astronomy, University of Gent, B-9000 Gent, Belgium*
[3]*Bartol Research Institute and Dept. of Physics and Astronomy, University of Delaware, Newark, DE 19716, U.S.A.*

Keywords: IceTop; IceCube; Extensive Air showers; Muon bundles

1 Introduction

The IceCube Neutrino Observatory started taking data in May 2011 with the complete array of 81 surface stations and 86 strings in the deep Antarctic ice [1]. The array grid is shown in Figure 1. In the period of June 2010-May 2011, the surface air shower array, IceTop [2], was operated with 73 stations (146 ice Cherenkov tanks) positioned on a triangular grid with a 125 m spacing. The IceCube detector had 79 strings with 60 sensors on each string at depths between 1450 m and 2450 m in the ice. We refer to this configuration as IceTop-73/IceCube-79. The detector collected data with 98% uptime during this period.

IceCube, located at the geographic South Pole (altitude: 2835 m), is at an optimum atmospheric depth of 680 g/cm^2 where cosmic ray air showers in the PeV energy range are close to their shower maximum. In addition, with fast digital electronics for signal processing and high resolution waveforms, IceTop is in a unique position to make a detailed measurement of the cosmic ray energy spectrum in this energy region in a few years. About 30% of showers trigger both detectors; these are called coincident events. The energy deposited along the kilometer long tracks of the penetrating muon bundles in IceCube, when combined with the energy deposited on the surface in IceTop, provide a mass composition sensitive measurement.

In this paper we evaluate the performance of IceCube as a three dimensional Extensive Air Shower (EAS) array based on nine months of data from June 15, 2010 to March 15, 2011. The data is split into an austral winter dataset (Jun 15, 2010 - Nov 1, 2010) and an austral summer dataset

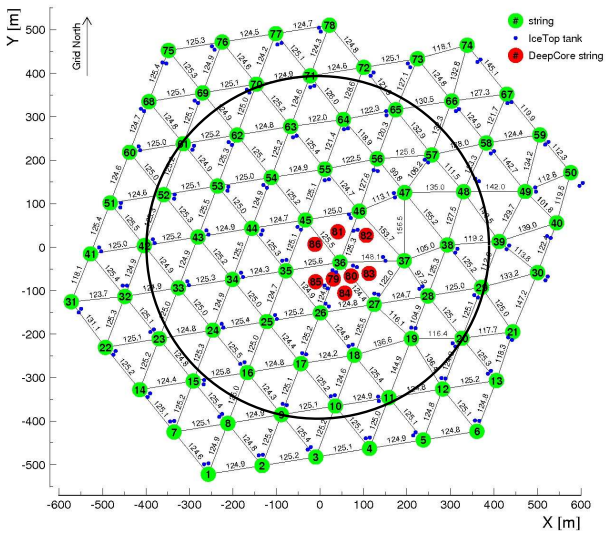

Figure 1: The surface map of IceCube in its completed configuration. IceTop Stations 1, 7, 14, 22, 31, 79, 80 and 81 were not yet deployed in 2010. The circle with a 400 m radius shows the containment criterium for the reconstructed shower core position.

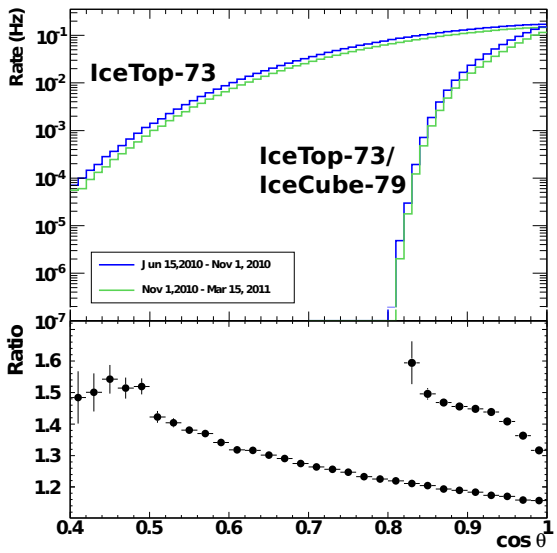

Figure 2: The differential rate of events in cosine zenith angle is shown in the top plot for IceTop-73 data and for coincident data. The dark (blue) and light (green) lines represent the austral winter and summer rates respectively. The ratio of winter to summer rates in the bottom plot shows the zenith angle dependence.

(Nov 1, 2010 - Mar 15, 2011) to investigate the basic shower observables and their temporal behaviour due to atmospheric changes. After minimal cuts the quality of the reconstructed events already reaches an accuracy to probe the inherent systematics left in data which may degrade the energy resolution and thus need to be studied further.

This analysis uses the largest statistical data set which covers two austral seasonal conditions. Earlier analyses [3, 4] did not account for atmospheric changes and could therefore not combine data of more than one season.

2 Reconstruction of basic observables

IceTop measures the Cherenkov light emitted by charged particles passing through the tanks. The timing information is used to reconstruct the arrival direction, while the signal strength is used for the core position. The lateral distribution of the energy deposition by each shower is fitted to a function of the signal strength in Vertical Equivalent Muons (VEM) versus distance to shower core. The signal strength evaluated at 125 m from the reconstructed shower core, S_{125}, is found by simulation studies to be sufficiently mass independent to primary energy for nearly vertical showers [5]. For coincident events also the IceCube signals were used, together with a fixed reconstructed core position at the surface, to fit the direction using a function which describes the muon bundle range-out [4]. This improves the angular resolution [6] and will be used to remove unrelated IceTop/IceCube coincident events.

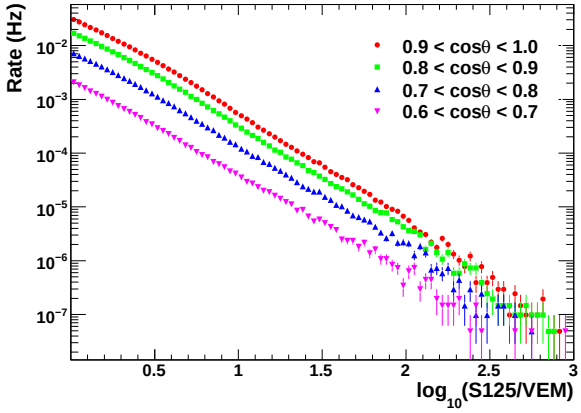

Figure 3: The differential rate of $\log_{10}(S_{125})$ for four zenith angle bands of equal solid angle in the region where IceTop is fully efficient. The plot quantifies the attenuation of showers with zenith angle. This attenuation is corrected when converting S_{125} to primary energy.

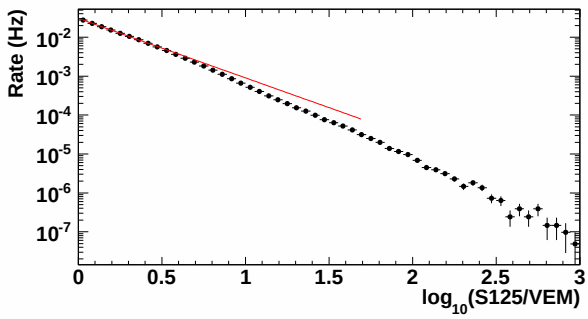

Figure 4: The differential rate of $\log_{10}(S_{125})$ for the coincident IceTop-73/IceCube-79 events with a line fitted between 0 and 0.5 to guide the eye.

2.1 Event selection

Air shower events which trigger at least five IceTop stations were reconstructed with the standard IceTop reconstruction procedure [7]. The events were selected if the reconstructed observables converged successfully, and the core location was reconstructed within a circle of 400 m radius from the IceTop array center as shown in Figure 1. On average, the reconstructed event rate was 2.55 Hz with a 12% variability due to the barometric pressure changes.

Events which trigger both the IceTop and the IceCube array, but do not belong to the same air shower constitute an important background for the coincident data sample. These so-called random coincident events were cut based on the time difference between the signals in IceTop and the signals in IceCube. The zenith angle difference between IceTop and IceCube direction reconstructions was also used to remove random coincident events. For a good energy loss reconstruction in the deep ice, the muon tracks which were not well contained by the detector volume (corner clippers) were not used in the final sample. This basic

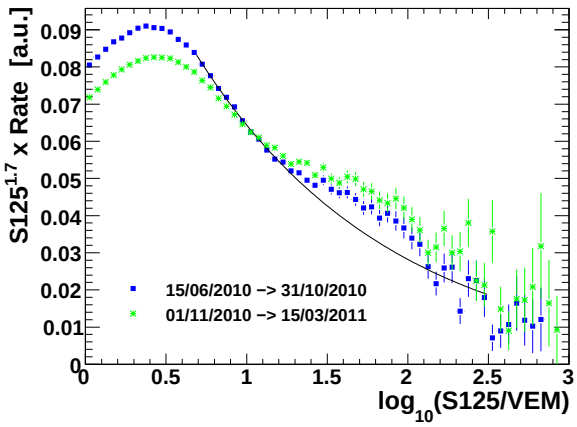

Figure 5: The weighted spectrum of $\log_{10}(S_{125})$ for the IceTop-73 events with $\cos\theta > 0.8$ is shown for winter and summer months by (blue) squares and (green) stars respectively. An exponential function is fitted to the slope of the winter curve between 0.7 and 1.1 and extrapolated to $\log_{10}(S_{125}) = 2.5$ to guide the eye.

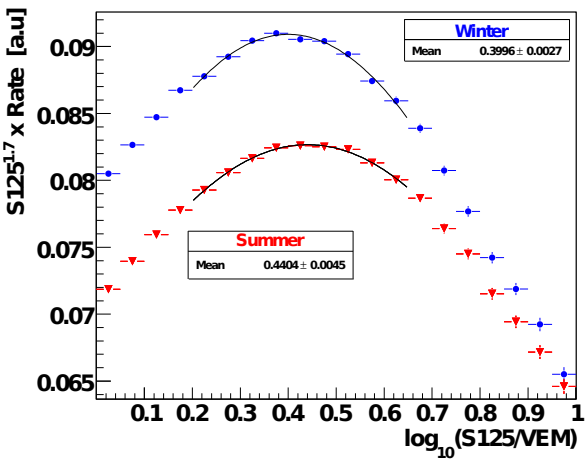

Figure 6: The knee region of the S_{125} spectrum. A shift of 0.04 in $\log_{10}(S_{125})$ is observed between the winter (blue circles) and summer (red triangles) spectra.

set of cuts results in a high quality, well reconstructed data sample with an angular resolution below 1° and a core resolution of about 10 m. The average IceTop-73/IceCube-79 coincident event rate after this selection was 0.72 Hz with a 15% variability.

In total 34.8 million events were left in the IceTop-73 data sample, while 9.5 million events remained in the coincident data sample (for a livetime of 236.44 days).

2.2 Basic shower observables and their temporal behaviour

Figure 2 shows the differential rate in cosine zenith angle for both IceTop-73 events and IceTop-73/IceCube-79 coincident events. The requirement that the muon bundle component of the air shower must pass through the IceCube detector leads to a steeper distribution for the coincident events. The light (green) line is the rate in the austral summer season and the dark (blue) line shows the rate in the austral winter season. The change in the atmospheric density profile [8] from winter to summer as well as the snow accumulation of 21 cm on average during 2010 contribute to the observed difference in rates between the two seasons. The ratio quantifies the angular dependence of both atmospheric and snow effects.

The differential rate of $\log_{10}(S_{125})$ is plotted for four zenith angle bands of equal solid angle in Figure 3 in the range where IceTop is fully efficient. The rate difference observed between the different zenith bands is due to the atmospheric attenuation. We could apply the classic Constant Intensity Cut analysis by calculating the attenuation for different zenith angles and evaluating the spectra at one zenith angle. In this analysis the IceTop-73 events were restricted to $\cos\theta > 0.8$ to study the atmospheric effects within this narrow angular range. However, with high statistics it will be possible to use each zenith band as a separate dataset to reconstruct and analyze with different methods and further explore its mass composition sensitivity.

In Figure 4 the differential rates of $\log_{10}(S_{125})$ for the coincident IceTop-73/IceCube-79 events are presented. The break seen in slope of the spectra around $\log_{10}(S_{125}) = 0.4$ is the cosmic ray knee.

To probe the details in the spectrum the rate weighted by $S_{125}^{1.7}$ for $\cos\theta > 0.8$ is plotted in Figure 5. It is interesting to note the opposite behaviour of the high and low energy events in different atmospheric conditions, causing a change in the slope. The spectra show a hardening trend between $1.2 < \log_{10}(S_{125}) < 2.1$. This systematically significant feature could not be traced back to any anomaly in data and is also seen by previous analyses [3, 4].

The knee position changes by 0.04 in $\log_{10}(S_{125})$, from 0.44 in summer to 0.40 in winter as shown in Figure 6. As the knee position should be at the same primary energy, the conversion from S_{125} to primary energy will need to take into account that the atmospheric variation and snow accumulation changes the detector response for the same primary energies.

From an energy estimator, which was derived by simulations of proton showers, $\log_{10}(S_{125}) = 1$ corresponds to about 10 PeV, $\log_{10}(S_{125}) = 2$ to about 100 PeV, and $\log_{10}(S_{125}) = 2.7$ to about 1 EeV. From Figures 3 and 4, the measured rates indicate that about 150 events per year are measured by the three dimensional IceCube air shower array above 300 PeV and about 15 events above 1 EeV. There is also no indication of array saturation up to 1 EeV.

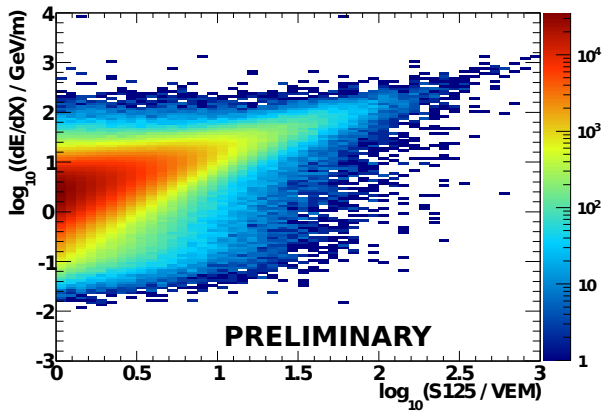

Figure 7: The average muon bundle energy loss $\frac{dE}{dX}$, measured by IceCube, shows a strong correlation with the shower size, reconstructed by IceTop, up to the highest cosmic ray energies.

3 Sensitivity to primary composition

When EAS propagate through the South Pole ice layer, only narrow ($\sim$ 20 m) bundles of highly energetic muons (>500 GeV) survive to the depth of IceCube. They will lose energy mainly stochastically which then generates Cherenkov light detected by IceCube. Here the average energy loss of muon bundles at the center of the IceCube detector volume is reconstructed using the measured charge signals and taking into account light propagation and the ice properties [9]. The energy loss of a muon bundle is a convolution of the muon multiplicity, the muon energy distribution within the bundle and the single muon energy loss. Both the multiplicity and the energy distribution depend highly on the primary mass and energy. Thus, the muon bundle energy loss provides a composition sensitive observable and can be determined with a resolution of about 0.3 in $\log_{10}$ of $\frac{dE}{dX}$ [9].

In Figure 7, nine months of high quality coincident data is shown. There is a clear correlation between the IceTop energy sensitive observable, S_{125}, and the energy loss up to the highest energies. Also, the shape of the distribution becomes narrower for higher S_{125} (larger showers). From simulations we know that proton and iron distributions become well separated in energy loss as function of primary energy [6]. The narrower distribution could therefore be related to a change in composition and will be studied further by simulations.

Events with a relatively low energy deposition in IceCube and no correlation with the IceTop shower size form the main background at this basic level of cuts as these are mainly caused by remaining random coincident events. However with minor cuts this is already reduced to the $\sim$1% level and will be further reduced in the next stage of the analysis.

4 Summary/Outlook

In this paper the performance of IceCube as a three dimensional cosmic ray detector was investigated using nine months of high quality data from June 15, 2010 to March 15, 2011 when the IceCube detector was in its 73-station/79-string configuration. We studied the behaviour of the basic observables in two distinct atmospheric conditions with the data split as austral winter and summer sets. We observed the change induced on the lateral development of showers by the atmospheric effects and snow accumulation, and a shift of 0.04 in $\log_{10}(S_{125})$ around the cosmic ray knee region between the two datasets. This observable effect on the shower development will be studied in detail. We observed that the high and low energy showers are affected by the seasonal effects in opposite way, having a higher rate of high energy showers in the austral summer atmosphere than in winter. The S_{125} spectra shows a systematically significant hardening between $1.2 < \log_{10}(S_{125}) < 2.1$. The cause of these effects, whether due to a change in shower maximum, change in the energy spectrum or a change in mass composition, will be the subject of further studies.

The observed zenith angle dependence of EAS and the seasonal expansion of the atmosphere can be used for composition studies. For coincident IceTop/IceCube air showers the composition sensitive ratio of muon bundle energy loss to shower size at the surface as well as the width of the energy loss distribution is being exploited.

A few years of cosmic ray data will already provide enough statistics to accurately measure cosmic ray energy spectrum and composition up to 1 EeV by using multiple composition and energy dependent shower observables through different techniques such as neural networks [4].

References

[1] H. Kolanoski, IceCube summary talk, these Proceedings.
[2] IceCube Collaboration, paper 807, these Proceedings.
[3] "All-particle cosmic ray energy spectrum measured with 26 IceTop stations" (The IceCube Collaboration), to be published.
[4] IceCube Collaboration, paper 923, these Proceedings.
[5] IceCube Collaboration, paper 379, these Proceedings.
[6] T. Feusels *et al.* , In Proc. 31th ICRC, Lodz, Poland, 2009, arXiv:0912.4668.
[7] S. Klepser, PhD thesis, Humboldt Univ, Berlin (2008).
[8] S. Tilav *et al.* , In Proc. 31th ICRC, Lodz, Poland, 2009, arXiv:1001.0776.
[9] S. Grullon *et al.* , In Proc. 30th ICRC, Merida, Mexico, 2007.

Simulation of IceTop VEM calibration and the dependency on the snow layer

THE ICECUBE COLLABORATION[1]
[1]*See special section in these proceedings*

Abstract: Seven years of construction on the IceTop air shower array have culminated in the final detector setup of 162 ice-filled tanks. The tanks are paired as stations over an area of one square kilometer. A continuous and automatic procedure calibrates each tank via the extraction of the vertical equivalent muon peak in the tank charge spectrum. Over the years snow has drifted unevenly on top of the tanks. The overburden of snow influences the charge spectrum as the electromagnetic part of an air shower is attenuated more than the muonic part. The impact on individual tanks affects trigger rates and the air shower event structure. We will present tank response studies with Monte Carlo simulations and compare them to measured IceTop charge spectra in light of the varying thickness of the snow layer.

Corresponding authors: Arne Van Overloop[2] (*arne.vanoverloop@ugent.be*)
[2]*Department of Physics and Astronomy, University of Gent, B-9000 Gent, Belgium*

Keywords: Vertical Equivalent Muon; Calibration; Cosmic Rays; IceTop; Simulations

1 Introduction

IceTop is the cosmic ray surface detector of the IceCube Neutrino Observatory [1], which is located at the South Pole and was completed in March 2011. The final setup consists of 162 tanks paired in 81 stations on a hexagonal grid with horizontal separations of about 125 m. The array covers an area of one square kilometer at an altitude of 2835 m above sea level, which is equivalent to an average atmospheric depth of 680 g/cm^2. The location together with the geometry and the applied trigger settings make the array sensitive to cosmic rays with energies between 100 TeV and 1 EeV.

An IceTop tank acts as a calorimeter, converting energy deposited by charged relativistic particles into Cherenkov light. The reconstruction of air shower observables such as space angle (zenith and azimuth), core location (x and y) and shower size relies on a good understanding of the light signals in the individual IceTop tanks. A natural way to calibrate and simulate tanks with their individual responses is to use the reference signal - vertical equivalent muon (VEM) - that high energy vertical muons imprint in the charge spectra of each tank.

A schematic of an IceTop tank is shown in Figure 1. The tank is a cylindrical polyethylene vessel 186 cm in diameter and 130 cm in height covered with insulation. The walls are 6 mm thick and the inner part is covered with 4 mm thick diffusely reflective liner of Zirconium[1] fused polyethylene. Each tank is initially filled up to a height of about 90 cm with purified water. Afterwards the water freezes via a controlled top-to-bottom procedure that lasts for about 40 to 50 days. To minimize impurities or contamination and cracks in the ice during the freezing process, a degasser system in combination with a circulation pump extracts air, swirls the water slowly around and removes excess water. At the top of the ice volume, two Digital Optical Modules (DOMs) are mounted to record the Cherenkov light pattern created by through-going and stopping particles. A DOM [2] is an ensemble of a photomultiplier tube (PMT) and digitising, communication and operation electronics inside a glass pressure sphere. In data taking mode the two PMTs inside one tank operate at a different voltage setting, enlarging the dynamic range in linear pulse charge assignment. Moreover, in case one DOM in a tank fails, the tank is not lost in further physics analysis. The ice surface and the two DOMs are covered with perlite, a volcanic ash, that acts as an insulator and prevents light from entering the ice volume and triggering the PMTs.

The tanks are embedded in snow until the snow level equals the surrounding surface. So at installation there is only snow on the sides, but winds blow snow on top of the tanks. Each year some tanks accumulate up to 30 cm of snow on top while others are still in the original setup without a snow layer. This leads to an asymmetry in the behavior of the array and needs to be understood via data and Monte Carlo comparisons.

1. Note that this is true for 150 tanks. The first 8 installed tanks in the year 2005 and 4 out of 16 tanks installed in the year 2010 are different and contain a Tyvek bag that acts as a reflector.

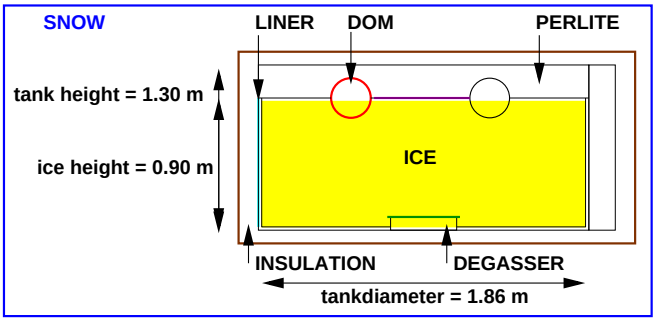

Figure 1: Schematic of an IceTop tank with its dimensions and its most important components. The trench where the tank is installed is backfilled with snow. Winds bring in snow that can accumulate on top of the tank.

2 Calibration

A good handle to study tank dependencies is to use the tank charge spectrum that is naturally generated by the very abundant low energy primary proton showers. Secondary muons within the 1 GeV to 10 GeV energy region leave a very clear and distinguishable signal behind in the tanks. The technique was used to calibrate the water tanks in the Auger experiment [3],[4] and it is also in use in IceTop [5] since 2005. An example of a charge spectrum (expressed in number of photo-electrons (PE)) of one single tank can be seen in Figure 2. The data was recorded between the 15th and the 22nd of January 2011. The overall spectrum is fit by the sum (solid) of a signal part (dashes) attributed to muons and a background part (dots) generated by electrons, positrons and gammas. The exact formula [6] reads:

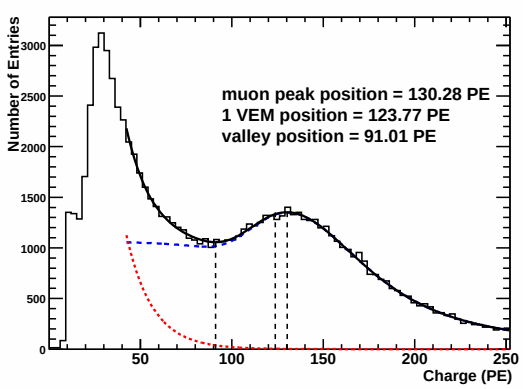

Figure 2: This is an experimentally measured charge spectrum of DOM 61-61 running in calibration mode. The total fit (solid) is the sum of the muon (dashed) and electromagnetic (dotted) contributions. The three extra lines visualize the positions given by the legend.

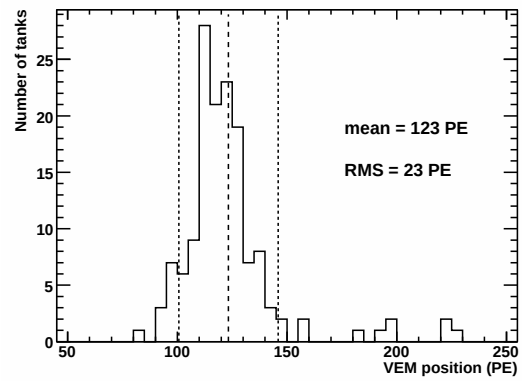

Figure 3: This histogram represents the VEM values of all the 146 (high gain) DOMs running between the 15th and the 22nd of January 2011. The lines visualize the mean and the root mean square region.

$$
\begin{aligned}
f(x) &= p_0 \left(\frac{1.85}{p_1} \frac{1}{\exp(\frac{x-p_1}{p_2}) + 1} + \mathrm{L}(x, p_1, p_2) \right) \\
&+ p_3 \cdot \exp(p_4 \cdot x) \quad ,
\end{aligned}
$$

where the first term in the summation describes the muon part: on its own a sum of a step function that describes corner clipping muons and L(x,p_1,p_2) a Landau function with p_1 the most probable value and p_2 a scale parameter that describes the bulk of through-going muons. So the signal part describes muons of all energies and incoming directions. Muon telescope measurements have pointed out that vertical muons build up charges around 95 % of the overall muon peak. The last term in the equation describes the exponential electromagnetic contribution. The three dashed vertical lines visualize the position of the valley, the muon peak and the 1 VEM unit.

Since June 2009 all the tanks of the IceTop detector are calibrated via an automated online procedure based on the fit described above. The muon calibration data is collected simultaneously with the physics data and hence both DOMs are evaluated at their running[2] gains. The calibration data is taken via a dedicated trigger that records every 8192nd hit per (high gain) DOM that is not in local coincidence with the other tank in the same station, i.e. there was no activity in the other tank within a short time window of 1 μs.

Each IceTop tank responds in an individual way to air shower particles due to small differences in size, ice quality, liner reflectivity, snow coverage and interfaces between the ice and DOM, the ice and the liners, the ice and the perlite and the ice and the degasser. The size of the ice block is important as more/fewer photons will be generated for longer/shorter tracks. Reflectivity and transmission will

2. In the old method calibration was performed on a different set of data where both DOMs were adjusted to the same gain.

depend on the amount of impurities and cracks in the ice, the quality of the liner and the interface between the ice and the surrounding material. The snow on top insulates the tank and so the PMTs in different tanks operate at different temperatures and hence gains. Snow also blocks the low energy electrons, positrons and gammas and so the energy threshold differs. Figure 3 shows the variety in PE per VEM for the 146 (high gain) DOMs operational between January 15th, 2011 and January 22nd, 2011. The average number is about 123 PE per VEM with a root mean square of 23 PE per VEM. The outliers with higher values belong to tanks lined with the higher reflectivity Tyvek.

3 Simulated VEM Spectrum

The VEM spectrum is the result of the convolution of two components: the ground particles created in air showers and the detector response for each of the particles. The air showers in this study are produced via CORSIKA (v6900) [7]. The high energy hadronic interactions are treated via SIBYLL (2.1) [8] while the low energy interactions are taken care of by FLUKA (2008) [9]. The transition between the models is set at center of mass energy of 80 GeV. The electromagnetic interactions are treated via EGS4 [10] parametrisations. The detector response to each particle is simulated via the official IceTray software [11] of the IceCube Collaboration. The IceTop tanks are modeled in a GEANT4 [12] environment that also tracks the ground level particles. The amount of Cherenkov photons that are generated inside the optical volume is used to assign the measured number of photo-electrons. The DOMs allocate a charge via an experimentally measured single photo-electron charge distribution.

The air showers are generated according the following conditions: only protons are assumed; the zenith angle θ ranges from 0 to 89 degrees and the azimuth angle from 0 to 360 degrees. The azimuth angle is sampled uniformly while the zenith angle is sampled from a $\cos(\theta)\sin(\theta)$ relation, the flat detector approach. The lowest triggering primary energy is given by the minimum amount of energy needed to create a muon in the atmosphere that can possibly arrive at the surface. At the South Pole this energy is about 3 GeV. The high energy limit is restricted by the calibration trigger condition that deletes hits from the calibration stream when there is activity in the nearby tank. Simulations point out that the upper limit is situated around 30 TeV. Moreover, Figure 4 shows that it is sufficient to simulate up to 10 TeV as the integrals of the muon spectra saturate. The x-axis is expressed here in units of VEM/0.95, so that the muon peak is situated at one. In the threshold region [0;0.4] the highest energies contribute a bit more than in the muon peak region [0.8;1.2]. This is also visible in Figure 5 where the integrals of the former spectra are shown as a function of the maximum energy in the dataset. Between 10 TeV and 30 TeV the integral increases about one to two percent, see therefore the solid line. The other markers give the integrals for the intervals

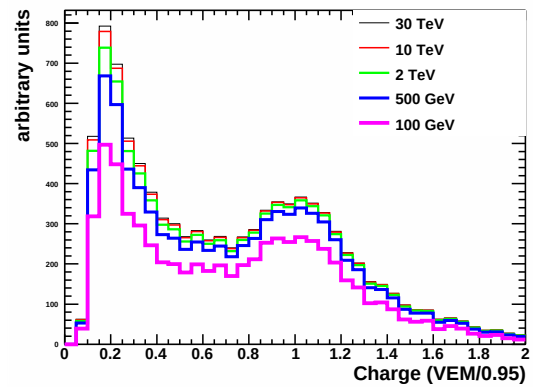

Figure 4: Different simulated muon spectra (weighted to $E^{-2.7}$) where the maximum energy that has been simulated changes. From bottom to top the maximum energy goes up between 100 GeV and 30 TeV as written in the legend.

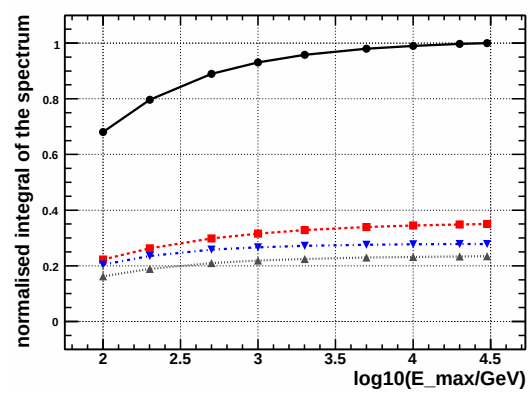

Figure 5: The same as Figure 4, but here the integrals of the muon spectra are plotted as a function of the maximum energy $E_{\max}$ used to build up the muon spectra. The solid line represents the whole integral. The dashed, dotted, dash-dotted lines are the integrals in following intervals [0;0.4], [0.4;0.8] and [0.8;1.2].

[0;0.4] (squares), [0.4;0.8] (triangles) and [0.8;1.2] (inverse triangles).

The VEM spectrum technique is used to calibrate the air shower simulations for high energy analysis. The simulated charge signals are calibrated in VEM units such that the simulated calibration muon peak is at the same position as in the corresponding experimental calibration data. The simulations perform well. All systematic checks completed and listed in Table 1 exhibit a stability in the 1 VEM position within two to three percent. The first (second) column gives the shifts of the 1 VEM position for simulations weighted to $E^{-2.4}$ ($E^{-2.7}$). The checks included tests on stability of random numbers, hadronic interaction uncer-

Check	$E^{-2.4}$	$E^{-2.7}$
different seeds	0.2 %	0.5 %
July vs January atmosphere	1.6 %	2.7 %
SYBILL vs QGSJET01c	0.7 %	2.9 %
10 cm to 200 cm of snow	0.4 %	0.7 %
different tanks/DOMs	1.5 %	–

Table 1: Results of systematic checks for the shift of the muon peak and according 1 VEM position due to a variety of effects listed. Two primary energy weightings are presented.

tainty, daily variations of the atmosphere, the accumulation of snow and the differences of all (high gain) DOMs.

4 Snow Dependency

Over the years, snow drifts unevenly on top of the tanks. As can be seen from Figure 6, the overburden of snow influences the charge spectrum as the electromagnetic part [0;0.75] of an air shower is attenuated more than the muonic part [0.75;1.25]. The ratio (S/B) between integrals of the muonic (M(h)) and the electromagnetic fit (EM(h)) in Figure 2 and expressed in the following formula:

$$(S/B)(h) \quad = \quad \int_{0.3\mathrm{VEM}}^{2.0\mathrm{VEM}} M(h) / \int_{0.3\mathrm{VEM}}^{2.0\mathrm{VEM}} EM(h) \quad ,$$

is a function of snow depth h. This is shown in Figure 7. The markers represent simulations where the primary energy is weighted via different differential spectral indices. The dotted and dashed lines are extrapolations to indices of -2.6 and -2.7 respectively. Direct weighting to these more realistic values of the differential spectral indices was not possible due to low statitics and large fluctuations. In comparison the experimental relation is given by the solid line which shows a bit stronger dependency on the thickness of the snow layer.

5 Summary

The VEM spectrum can be efficiently generated with an uncertainty of 2-3%. This leads to an absolute charge calibration in simulation. The snow dependency of the signal to background (muon versus electromagnetic) ratio in experimental data is slightly stronger than the one found in simulated data and has to be further investigated.

References

[1] H. Kolanoski et al, IceCube summary talk, these proceedings
[2] R. Abbasi et al, NIM A, 2009, **601**: 294
[3] X. Bertou et al, 28th ICRC Proc., 2003, 813
[4] A. K. Tripati et al, 28th ICRC Proc., 2003, 1

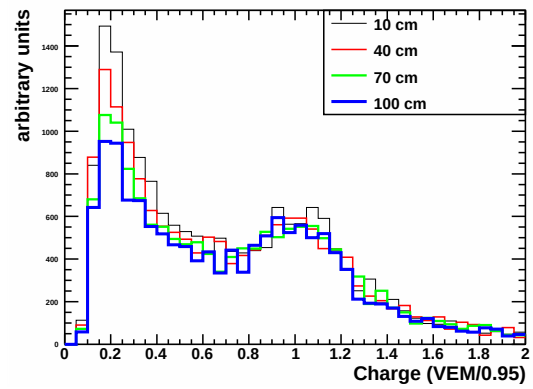

Figure 6: The four histograms represent the ($E^{-2.7}$) simulations of DOM 61-61. The only difference is the amount of snow on top of the tank lids. From top to bottom the snow thickness amounts to 10 cm, 40 cm, 70 cm and 100 cm.

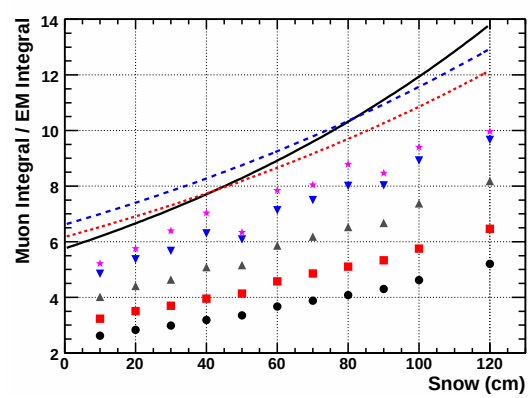

Figure 7: The snow dependency of S/B (see text). The markers represent the simulation weighted with different differential spectral indices: -1.6 (circles), -1.8 (squares), -2.0 (triangles), -2.2 (inverse triangles) and -2.4 (diamonds). The solid line is the relation found in experimental data. The dotted and dashed lines represent extrapolated results for differential spectral indices of -2.6 and -2.7 respectively.

[5] L. Demirörs et al, 30th ICRC Proc., 2007, 1261
[6] M. Beimforde, diploma thesis Humboldt University, 2006
[7] D. Heck et al., Report FZKA 6019
[8] R.S. Fletcher et al, PRD, 1994, **50**: 5710
[9] A. Fasso et al, CERN-2005-10 (2005), INFN/TC 05/11, SLAC-R-773
[10] W. R. Nelson et al, Report SLAC 265 (1985)
[11] T. DeYoung et al, CHEP2004
[12] S. Agostinelli et al., NIM A, 2003, **506**: 250

Atmospheric Muon Spectrum from Catastrophic Energy Losses in IceCube

THE ICECUBE COLLABORATION[1]
[1] *See special section in these proceedings*

Abstract: While the primary purpose of IceCube is the search for high-energy astrophysical neutrinos, the overwhelming majority of events is caused by downgoing cosmic-ray induced muons. This provides a high-statistics data set which can be used for both detector calibration and supplemental physics investigations. In this work, we present a method to identify TeV-scale catastrophic energy losses along muon tracks and its application to the separation of single high-energy muons from large-multiplicity bundles which dominate the event sample above the horizon at high energies. The information can be used to derive the single-muon energy spectrum at all zenith angles up to energies of hundreds of TeV. We demonstrate that our measurement is sensitive to a cutoff of the proton spectrum at the cosmic ray knee and potentially to the prompt lepton flux caused predominantly by decay of charmed hadrons in atmospheric CR interactions.

Corresponding authors: Patrick Berghaus[2] *(berghaus@icecube.wisc.edu)*, Chen Xu[2] *(chen@udel.edu)*

[2] Bartol Research Institute, University of Delaware, USA

Keywords: Muon Spectrum, Stochastic Losses, Knee

1 Introduction

In recent work on high-energy atmospheric muon fluxes, it was pointed out that second-generation astrophysical neutrino detectors such as IceCube should be able to substantially extend the energy range of muon energy spectrum measurements and hence address various important open problems in cosmic-ray physics. These include verification of hadronic interaction models, primary composition at PeV energies and prompt contributions to the lepton flux [1].

From an experimental perspective, the main challenge in the measurement of the muon energy spectrum is limited spatial resolution due to the sparse instrumentation of the detector. With a minimum separation of 17 meters between Digital Optical Modules (DOMs) in IceCube, resolution of individual muons within a shower is usually impossible. Previous measurements [2, 3] took advantage of the shorter range of large-multiplicity muon bundles compared to individual high-energy muons during passage through matter to measure the muon spectrum at large slant depths near the horizon. The limited angular resolution of the detector and background from up-going atmospheric neutrinos mean that the range of this technique is limited to values up to approximately 100 TeV. Furthermore, the muon spectrum can in this way only be measured in an angular region where the relative contribution from prompt interactions is lowest, excluding investigation of this flux component for practical purposes.

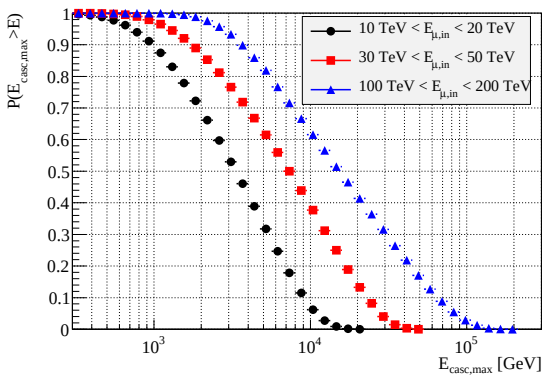

Figure 1: Probability for a stochastic loss above a given energy to occur within the detector volume, for three typical muon energy ranges. The simulation was performed using MMC [5].

In order to take advantage of the full potential of a large-volume detector, it is therefore necessary to develop a method that allows separation of showers with exceptionally highly energetic muons from the dominant background of bundles containing low-energy muons of higher multiplicity. It has long been proposed to make use of the fact that the stochasticity of energy deposition along muon tracks increases with energy [4]. In this analysis, by identifying muon track segments with unusually strong photon

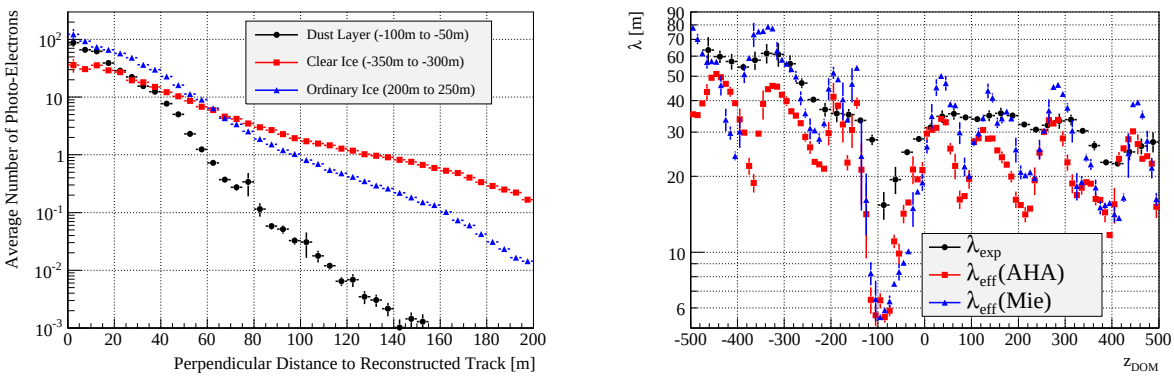

Figure 2: Left: Average number of photo-electrons registered in IceCube DOMs as a function of perpendicular distance from reconstructed muon tracks for three different depth bins. Values are averaged over events with a total charge $Q_{tot} >$ 1000 p.e. Right: Value of scattering parameter λ_{exp} from fitting distributions on the left to Eq. 1 in dependence of vertical depth. The value of $z_{DOM} = 0$ corresponds to the center of the IceCube array, located 1950 meters below the surface of the ice. The effective scattering length in two different ice models [6] is included for comparison. It is important to note that the physical meaning of λ_{eff} and λ_{exp} is not identical. Fine structures in the depth dependence are inherently smeared out in the experimentally derived parameter.

emission, the amplitude of individual stochastic losses can be used to infer the most likely energy of the parent muon, as illustrated in Figure 1.

2 Energy Estimation Method

The IceCube detector array records Cherenkov photons emitted by relativistic particles during passage through ice. The amount of charge in the optical modules provides calorimetric information that can be used to calculate the energy released in the event.

Previous energy reconstructions relied on prior assumptions about ice properties whose accuracy was necessarily limited. The method described here is based exclusively on experimental observations. Its is based on two simple assumptions:

- Down-going tracks in IceCube consist mainly of muon bundles dominated by minimum-ionizing muons which lose their energy smoothly and continuously.
- The total number of emitted Cherenkov photons is in good approximation proportional to the deposited energy.

As illustrated in Figure 2, the total amount of light registered in the DOMs can then be approximated by the empirical function

$$\frac{dE(x = x_0)}{dx} \propto Q(x_0) \cdot d(x_0) \cdot \exp\left(\frac{d(x_0) - 25}{\lambda_{exp}(x_0)}\right) \quad (1)$$

where $\frac{dE(x)}{dx}$ is the energy loss at vertical depth x, Q is the total charge in each DOM and d is the perpendicular distance between a DOM and the reconstructed muon track.

This data-derived model only relies on a single scattering parameter λ_{exp}, which varies in dependence of the local ice properties. From the charge in each DOM, it is possible to calculate a value that is approximately proportional to the energy deposited in its vicinity. Monte-Carlo simulated data are only required to determine the proportionality factor in Eq. 1 and for verification. Assuming point-like isotropic emitters on the track, clusters of exceptionally high values can be used to identify energetic stochastic energy losses. An example can be seen in Figure 3.

There are two important additional benefits that arise naturally from this technique. The first is the reduction of biases resulting from uncertainties about exact ice properties, allowing for detailed investigation of simulation biases. The other is the availability of information about differential energy deposition, permitting the construction of more accurate event energy estimators.

3 Analysis Procedure

This analysis was based on data from IceCube in its 59-string configuration (IC59). Only events with a total of more than one thousand photo-electrons registered in the detector were considered. This selection provides a sample of events at all zenith angles which is not biased by the quality criteria used to select physics filter streams.

The analysis procedure itself mainly consists of two relatively simple steps. First, a sample of muon tracks with strong stochastic losses inside the detector volume were identified. Then, the energy of the strongest single energy deposition was reconstructed and its spectrum compared to various benchmark models.

The principal conditions that were imposed in the selection are:

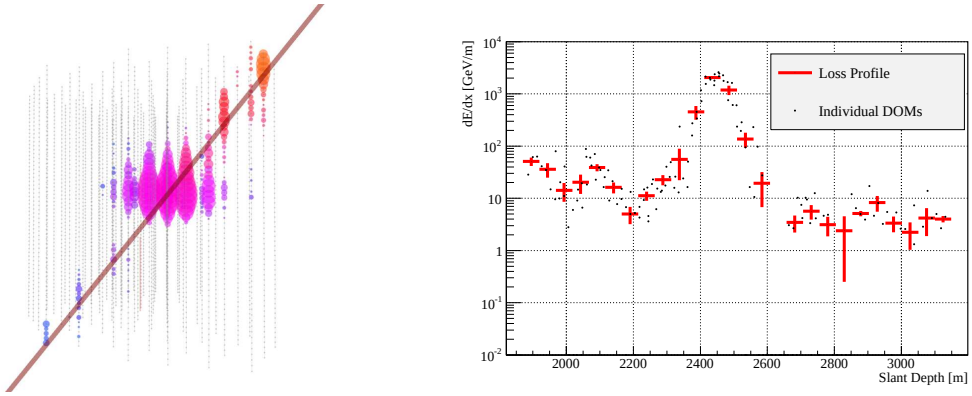

Figure 3: Example for massive stochastic loss event found in IC59 data. The energy deposition estimate shown on the right hand side is consistent with an 80 TeV cascade. The x-axis corresponds to the distance along the track, measured from the surface of the ice.

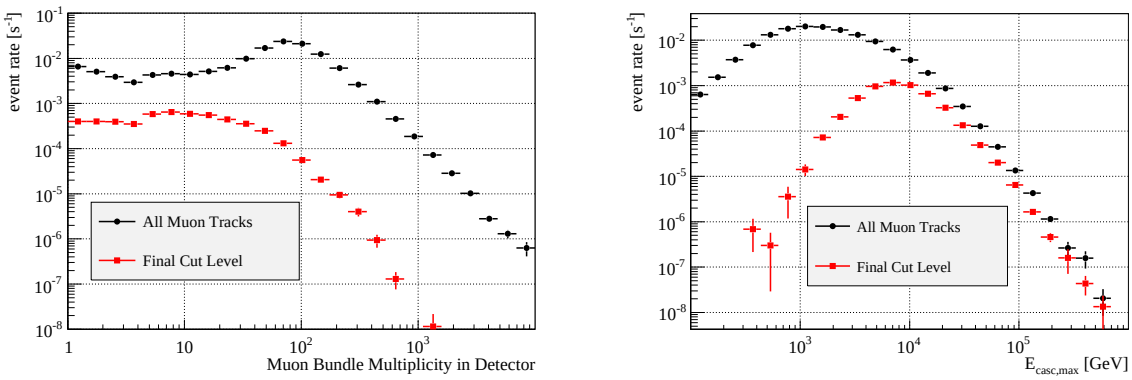

Figure 4: Left: Muon multiplicity in cosmic-ray showers at entry into detector volume before and after selection cuts, simulated using CORSIKA/SIBYLL. The analysis favors muon bundles of moderate multiplicities while reducing both high-multiplicity bundles and low-energy tracks with high recorded DOM charges due to unusual topologies. Right: Effect of selection cuts in dependence of true maximum stochastic loss energy. The effective threshold energy lies around 10 TeV.

- Presence of a well-reconstructed muon track with a length of at least 600 meters inside the detector volume.
- A peak energy loss value in a 50-meter bin along the track which exceeds the median differential energy loss in the event by a factor of 10.
- Location of peak energy loss within 150 meters from at least 50 DOMs, assuring containment within the main detector volume.

Figure 4 shows the cumulative effect of the cuts.

So far, the effective threshold energy for stochastic losses lies around 10 TeV. It is in principle possible to reduce this threshold further by relaxing the requirement on the total recorded DOM charge.

4 Result

To estimate the sensitivity of the method, the measured energy spectrum of stochastic losses was compared to simulations based on various primary composition models [7]:

- **Constant Composition**: The spectrum of each primary nucleus type changes by the same amount at an energy corresponding to the cosmic-ray knee.
- **Rigidity-Dependent Cutoff**: Each component of the cosmic ray flux is subject to a cutoff at an energy that is proportional to the charge of the nucleus.
- **Mass-Dependent Cutoff**: Similar to the previous model, but assuming a cutoff dependent on the nuclear mass. The main distinction here is a sharper transition, resulting in a stronger cutoff signature.
- **No Knee**: This additional model was included for purposes of illustration only, assuming unbroken spectra for each component and therefore completely

eliminating the knee. It should be noted that this assumption is strongly disfavored by previous experimental results.

Figure 5 shows the preliminary result, based on a subsample of 10 percent of the data taken with IC59. For models incorporating a cutoff in the individual primary spectra, a corresponding effect can clearly be discerned in the simulated muon-induced stochastic losses. The limited experimental statistics do not yet allow any definite statement about preferred models, even while neglecting systematic uncertainties.

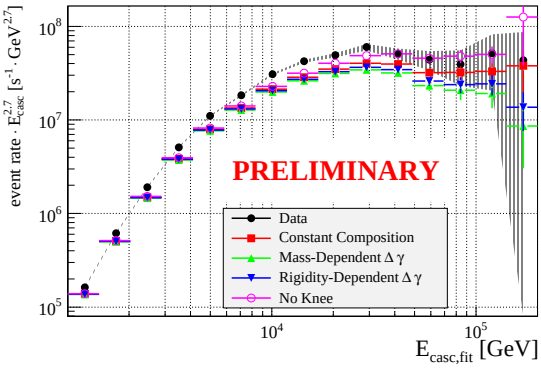

Figure 5: Comparison of reconstructed maximum stochastic loss energy for simulated and experimental data summed over all zenith angles. All simulated curves were obtained by reweighting the same data set generated with CORSIKA. Experimental data correspond to a subset of ten percent of IC59 events. The error band is purely statistical.

5 Conclusion and Outlook

As can be seen from comparing Figures 5 and 6, the highest muon energy found in the analyzed sample is most likely located around 500 TeV, with slight variations depending on the exact primary spectrum. This means that despite the fact that the spectrum falls off almost as the fourth power of the particle energy, the range of the measurement can be extended by roughly an order of magnitude compared to earlier experiments. The method presented here furthermore allows the measurement of cosmic-ray induced muon spectra independently of the zenith angle, introducing an entirely new degree of freedom.

Consequently, it will be possible to address a variety of new physics issues that were previously inaccessible. It has already been demonstrated that the behavior of cosmic rays around the knee can now be probed directly. A separate but equally important question is the contribution of prompt production processes to lepton fluxes at high energies. In optimistic models, the charm-induced component becomes dominant around 300 TeV at near-vertical angles [8] and would therefore be directly measurable. If on the other

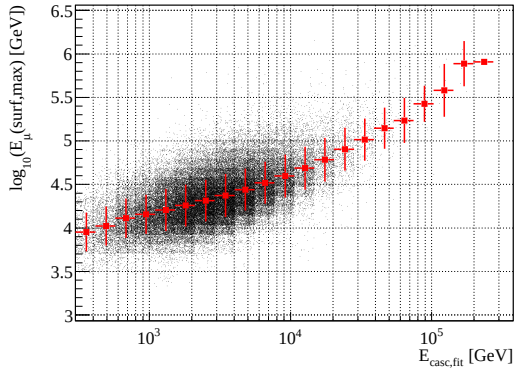

Figure 6: Relation between reconstructed cascade and muon surface energy obtained from Monte-Carlo simulation, assuming a poly-gonato primary spectrum and neglectic prompt muons. The change in slope around 10 TeV can be attributed to threshold effects.

hand the prompt muon flux were low enough to be dominated by decays of unflavored light mesons [9], it should be possible to set a stringent limit that would strongly constrain the atmospheric neutrino background in searches for astrophysical sources.

It should also be emphasized that the method to distinguish unusually energetic muons from large-multiplicity background events is readily adaptable for analyses targeting neutrino fluxes at energies in the PeV range.

References

[1] S. I. Sinegovsky, A. A. Kochanov, T. S. Sinegovskaya, A. Misaki and N. Takahashi, Int. J. Mod. Phys. A **25** (2010) 3733, [arXiv:0906.3791].

[2] P. Desiati [AMANDA Collaboration], *Proc. of ICRC 2003*.

[3] P. Berghaus [IceCube Collaboration], *Proc. of ICRC 2009*, [arXiv:1004.2093].

[4] R. P. Kokoulin and A. A. Petrukhin, Nucl. Instrum. Meth. A **263** (1988) 468.

[5] D. Chirkin and W. Rhode, [arXiv:hep-ph/0407075].

[6] See the contribution by D. Chirkin in these proceedings.

[7] J. R. Hörandel, Astropart. Phys. **19**, 193 (2003), [arXiv:astro-ph/0210453].

[8] T. K. Gaisser, Nucl. Phys. Proc. Suppl. **118** (2003) 109, [arXiv:astro-ph/0502380].

[9] J. I. Illana, P. Lipari, M. Masip and D. Meloni, Astropart. Phys. **34** (2011) 663, [arXiv:1010.5084].

Study of High p_T Muons in IceCube

THE ICECUBE COLLABORATION[1]
[1]*See special section in these proceedings*

Abstract: Muons with a high transverse momentum (p_T) are produced in cosmic ray air showers mostly via semileptonic decay of heavy quarks and the decay of high p_T kaons and pions in jets. These high p_T muons have a large lateral separation from the shower core and accompanying muon bundle. IceCube, a kilometer-scale neutrino telescope consisting of an array of photodetectors buried in the ice of the South Pole and a surface air shower array, is well suited for the detection of high p_T muons. The surface shower array can determine the energy, core location and direction of the cosmic ray air shower while the in-ice array can do the same for the high p_T muon. This makes it possible to measure the cosmic ray muon lateral separation distribution at distances greater than 200 meters. The preliminary results from analysis of data from 25% of the full IceCube detector will be presented.

Corresponding authors: L. Gerhardt[2,3] (*lgerhardt@lbl.gov*), S. R. Klein[2,3] (*SRKlein@lbl.gov*)
[2]*Lawrence Berkeley National Laboratory, Berkeley, California 94720*
[3]*University of California, Berkeley, Berkeley, California 94720*

Keywords: cosmic rays, muons, icecube

1 Introduction

IceCube, a kilometer-scale neutrino telescope, is well suited for measuring the lateral separation of muons in cosmic ray air showers. Completed in December 2010, it consists of a 1 km^3 array of optical sensors (digital optical modules, or DOMs) buried deep in the ice of the South Pole and a 1 km^2 surface air shower array called IceTop. IceTop has an energy threshold of 300 TeV and can reconstruct the direction of showers with energies above 1 PeV within $\sim$1.5° and locate the shower core with an accuracy of $\sim$10 m [1]. The in-ice DOMs (here referred to as IceCube) are buried in the ice 1450 m under IceTop on kilometer-long strings of 60 DOMs with an intra-DOM spacing of 17 m. IceCube can reconstruct high quality tracks of high energy muons with $< 1°$ accuracy. IceTop and IceCube can be used together to select cosmic ray events with a muon with a minimum lateral separation of $\sim$200 m. The measurement of the lateral separation distribution of muons in air showers provides a valuable check on air shower simulation models and can be used as an independent method for determining the cosmic ray composition [2].

The most common source of muons with a large lateral separation is muons with a high transverse momentum (p_T) primarialy from charm and bottom mesons and jets of high p_T partons [2]. The transverse separation is given by:

$$d_T = \frac{p_T h c}{E_\mu} \tag{1}$$

where E_μ is the energy of the high p_T muon, and h is the interaction height of the shower, here taken as an average value of 25 km. The interaction height loosely depends on the composition and a full treatment of this is planned in the future. Using a separation of 200 m (75 meters more than the string separation) as a rough threshold for the two-track resolution distance of the high p_T muon from the shower core gives a minimum resolvable p_T of 8 GeV/c for a 1 TeV muon. Rough calculations predict on the order of tens of high p_T muon events in the studied data sample [2].

The combined acceptance for cosmic ray air showers that pass through both IceTop and IceCube is 0.3 km^{2}sr for the full 86-string IceCube array [3]. By the end of the austral summer of 2006/2007, 22 IceCube strings and 26 IceTop tanks had been deployed. The combined acceptance for showers that trigger both IceTop-26 and IceCube-22 is 0.09 km^{2}sr. In 2007 the discriminator threshold settings for IceTop were changed partway through the year to sub-optimal values, so this analysis discards the data taken during this period leaving 114 days of livetime. A search has been conducted in this data for cosmic ray events with a muon with a large lateral separation.

The underground muon detector MACRO has previously measured the separation between muons in air showers for shower energies ranging roughly from 10^4 GeV to 10^6 GeV [4]. MACRO measured muon pair separations out to a distance of about 65 meters. They verified the linear relationship between p_T and separation shown in Eq. 1 (with a

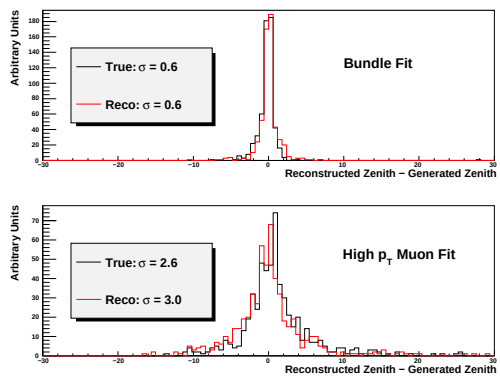

Figure 1: Zenith angle resolution of the high p_T reconstruction algorithm. The sigma are the results of Gaussian fits to the distributions.

small offset due to multiple scattering of the muons) out to momenta up to 1.2 GeV/c.

2 Reconstruction Methods

High p_T muons appear as a separate track coincident in time and parallel with the track from the central core of low p_T muons. Generally the bundle of low p_T muons leaves more light in the detector than the high p_T muon.

Current reconstruction algorithms in IceCube are designed to reconstruct single tracks. In order to reconstruct high p_T double-track events the hit DOMs (i.e. DOMs that detect at least one photon) are attributed to either the muon bundle or high p_T muon based on their timing and position. The muon bundle is reconstructed first by the IceTop surface array. This reconstruction serves as a seed for a likelihood-based reconstruction using the IceCube DOMs. Only IceCube DOMs within 90 m of the seed track are used for bundle reconstruction. The high p_T muon hits are selected relative to the reconstructed bundle track. The high p_T muon arrives at the same time but laterally separated from the bundle, so its hits will have a negative time residual relative to the bundle reconstruction. Additionally, high p_T muon hits are required to be at least 90 m from the reconstructed muon bundle track. The high p_T muon hit track is reconstructed using a likelihood reconstruction with a downgoing hypothesis.

Figure 1 shows the performance of this procedure after reconstruction quality selection criteria have been applied. The zenith angle resolution for groups determined using the true simulation information (black, solid lines) is compared to the resolution for groups determined using the splitting algorithm (red, dashed lines) for the muon bundle (top) and high p_T muon (bottom). Roughly 50% of the events fail to reconstruct because there are not enough DOMs in one of the groups.

These reconstruction algorithms achieve a zenith angle (space angle) resolution of 0.6° (1.3°) for the muon bundle and 2.6° (8.2°) for a high p_T muon separated by 200 m. The resolution is worse for the high p_T muon because fewer DOMs are hit. While high p_T muons with a greater separation are much easier to resolve with the two track algorithm, they also tend to be lower energy (see Eq. 1) and hit fewer DOMs. The average number of DOMs hit by the high p_T muon is 15, compared to 90 for the muon bundle. Additionally, because high p_T muons have fewer hit DOMs, a DOM hit by the muon bundle that is incorrectly placed in the high p_T group has a much larger effect on the reconstruction of the high p_T track (it can also degrade the bundle resolution, but to a lesser extent). These factors degrade the resolution of the high p_T track direction and timing. The spatial resolution of the high p_T muon track (as measured by the difference between the reconstructed track and the true track at the point of closest approach to the detector) is 40 m in x, y, and z.

3 Signal and Background Separation

Since high p_T muons occur in only a fraction of simulated showers, a toy model based on CORSIKA [5] proton showers was used to model the signal. A single muon is inserted into an existing CORSIKA event containing a muon bundle from an air shower. This modified shower is then run through the standard IceCube propagation, detector simulation, and reconstruction routines. Simulations insert a muon with energy of 1 TeV separated 100, 150, 200, and 400 m from the shower core.

Cosmic ray air showers that do not generate a high p_T muon (called 'single muon bundles') are a background to this search. Since they generate only one track in the array, these events are mostly eliminated by requiring there be two well-reconstructed tracks in the IceCube detector.

The IceCube 22-string configuration is large enough that the rate of simultaneous events from cosmic rays is significant. Muon bundles from two (or more) air showers can strike the array within the 10 μs event window, producing two separated tracks. These so-called double-coincident events are another background for air showers with high p_T muons. Since these double-coincident events are uncorrelated in direction and time, requiring that both reconstructed tracks be parallel (within 15° of each other) and occur within $\pm$600 ns can eliminate most of these events. However, an irreducible background remains from double-coincident events that happen to come from roughly the same direction and time. The rate of double-coincident events can be estimated by looking at the off-time rate of events (i.e. events with tracks that occur more than 600 ns apart) in the data that pass all other selection criteria.

A number of selection criteria are applied to separate events with high p_T muons. The events are required to trigger at least 6 DOMs in IceTop and at least 8 DOMs in IceCube. The events are also required to have high quality two-track reconstructions. This includes requiring that the tracks have at least one hit DOM with a time residual of less than 15 ns (a 'direct hit') and that tracks pass within the

detector fiducial volume. Further reduction of single muon bundles is done based on the differences in event topologies and timing. For instance, single muon bundles are well-reconstructed by a single track hypothesis, while the high p_T muon events are not. Figure 2 shows the negative log of the reduced likelihood of a single track reconstruction for single muon bundles, and showers with an inserted 8 and 16 GeV/c p_T, 1 TeV muon (separation of 200 m and 400 m from the shower core, assuming an average interaction height of 25 km). Well-reconstructed events have a lower likelihood value on this plot. For large separations, this variable separates single muon bundles from showers which contain a high p_T muon. This analysis retains events with a likelihood greater than 7.5. Next we require that the high p_T muon track be a robust track in the detector with at least 6 direct hits. Finally, the remaining background single muon bundle events are removed by requiring the perpendicular separation between tracks to be at least 160 m. The number of events passing each type of selection criteria for data and simulated background and signal are shown in Table 1.

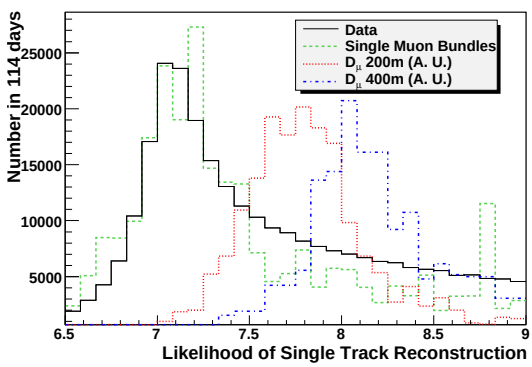

Figure 2: Negative log of the reduced likelihood for the single track reconstruction

4 Results

After applying all selection criteria 53 events remain in 114 days of data. No events remain in the simulated background. One event that passes all the selection criteria is shown in Fig. 3. The reconstructed high p_T muon and bundle track have a perpendicular separation of 207 m at the center of the detector. The two tracks arrive within 470 ns and 3.3° of each other.

4.1 Purity of Final Sample

Simulation of single muon bundle background events is too computationally intensive to accumulate large statistics. Although no simulated single muon bundle event passed all the selection criteria, the possibility exists that some single muon bundle background events could survive in the final data sample. In order to estimate the purity of

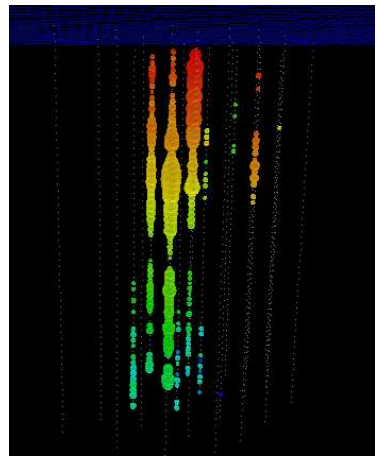

Figure 3: Candidate shower with a high p_T muon. The cosmic ray bundle is on the left and the high p_T muon is on the right.

the final sample a study has been conducted of simulated events which pass the reconstruction quality and double-coincident seleciton criteria (without applying the criteria designed to remove single track events). At this cut level, the only events left in the single muon bundle background are events which are incorrectly split into two tracks by the splitting algorithm. Two previously unused variables were developed that focused on studying how well the bundle fit described the high p_T muon hits and vice versa.

The first variable is the standard deviation of the time residual relative to the reconstructed bundle track (σ_{bundle}). Only hits belonging to the high p_T muon reconstructed track (time residual $<$ 100 ns and distance from the bundle $>$ 90 m) were used to calculate σ_{bundle}. In the single muon bundle background σ_{bundle} is small because the bundle reconstruction is equally good at describing both sets of hits. Conversely, events with high p_T muons have a laterally separated track that is causally disconnected from the bundle track. This leads to larger values of σ_{bundle}.

The second variable is the mean of the time residuals relative to the reconstructed high p_T muon track. Only hits within 90 m of the bundle track are used for this calculation. This variable uses the fact that the parallel but laterally separated high p_T muon track have a negative time residual relative to the bundle track. Single muon bundles incorrectly split into two groups tends to have time residuals that are closer to zero because both groups are causally consistent with the bundle hypothesis.

These two variables are shown in Fig. 4. The background single muon bundles and high p_T muon simulation are at a relaxed cut level with only reconstruction quality and double-coincidence selection criteria applied, while the data points are after all selection criteria have been applied. The dashed grey line is a fit to the mean of the background single muon bundle points. To estimate the purity of the data sample, this line has been moved upwards until every simulated single muon bundle event is below it. Thirty-one

Cut	Data	Simulation	Simulated Signal (%)
IceTop and IceCube Trigger	1.35 x 10^7	1.47 x 10^7	100%
Bundle and High p_T Reconstructions Successful	4.59 x 10^5	3.04 x 10^5	49%
Double-Coincidence Cuts	1.16 x 10^5	1.35 x 10^5	25%
Reconstruction Quality Cuts	2.57 x 10^4	1.64 x 10^4	13%
Single Track Cuts	53	0	8%

Table 1: Number of events in 114 days for data and simulated background. The percentage passing rates for simulated high p_T muons with a lateral separation of 200 m (8 GeV/c) are shown as well.

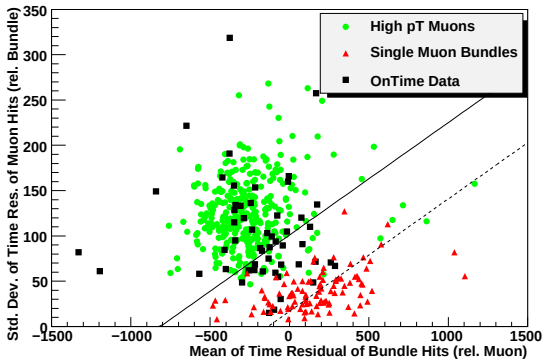

Figure 4: Standard deviation versus mean of time residuals. Note that the selection criteria have been relaxed for the simulated events.

of the fifty-three data events lie above the line, giving a preliminary estimation for the purity of the final event sample of at least 58%.

4.2 Estimation of Double-Coincident Rates

As mentioned in Section 3, an irreducible background remains from double-coincident cosmic rays. The number of these events in the on-time window ($\pm$600 ns) can be estimated by counting the number of events with tracks that occur with a time difference greater than 600 ns after applying all other selection criteria. In the final data sample, eight events were found in this off-time window. To be conservative, two events with a time difference greater than 20,000 ns are discarded. The remaining six events were spread over a time range of 2260 ns, giving an expectation that 3 of the 53 events in the $\pm$600 ns on-time window are due to double-coincident cosmic rays.

4.3 Lateral Distribution of Muons

Figure 5 shows the preliminary perpendicular separation between the bundle and high p_T muon reconstructions at the center of the detector. The black solid lines are the 53 data events that passed all selection criteria. Preliminary estimations indicate that this sample is 58% pure. The dashed red lines are the data events that passed all selection criteria, but had time differences greater than $\pm$600 ns. These events have been scaled down to the rate of 3 events in the on-time window.

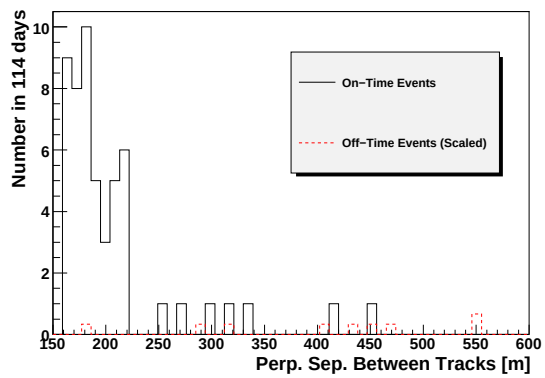

Figure 5: Preliminary perpendicular separation between bundle and high p_T muon reconstructions at the center of the detector.

5 Conclusions

A search for cosmic ray events with laterally separated muons has been conducted in 114 days with 25% of the full IceCube detector. The fraction of single muon bundle events remaining in the final sample has been conservatively estimated to be 42% and the number of background double-coincident events has been shown to be very small. Further searches with IceCube data with larger instrumented volume will have important implications for cosmic ray composition and air shower simulation.

References

[1] S. Klepser, 21st European Cosmic Ray Symposium (2008), arXiv:0811.1671.
[2] L. Gerhardt and S. Klein, 31st ICRC (2009), in arXiv:0909.0055.
[3] X. Bai and T.K. Gaisser, Proceedings of the TeV Particle Astrophysics II Workshop, J. Phys.: Conf. Ser. **60**:74 (2007).
[4] M. Ambrosio *et al.* , Phys. Rev. D **60**:032001 (1999).
[5] D. Heck, Forschungszentrum Karlsruhe Report FZKA 6019 (1998).

Energy Dependence of the Large Scale Galactic Cosmic Rays Anisotropy Measured With IceCube

THE ICECUBE COLLABORATION[1]
[1]*See special section in these proceedings*

Abstract: We report on a study of the energy dependence in the arrival direction distribution of cosmic rays at median energies of 20 and 400 TeV. The data used in this analysis contain 33×10^9 downward going muon events collected by the IceCube neutrino observatory between May 2009 and May 2010 when it comprised of 59 strings. The high rate of cosmic ray induced muons observed by IceCube allows us to perform the first study of the galactic cosmic ray arrival distribution around 400 TeV in the Southern sky. The sidereal anisotropy observed at 400 TeV shows substantial differences with respect to that at lower energy. Studies of the energy dependence of the anisotropy could further enhance the understanding of the structure of the local interstellar magnetic field and possible nearby cosmic ray sources.

Corresponding Authors: Rasha Abbasi[2](*rasha.abbasi@icecube.wisc.edu*), Paolo Desiati[2](*desiati@icecube.wisc.edu*)
[2]*Dept. of Physics, University of Wisconsin-Madison, Madison, WI 53703, USA*

Keywords: IceCube, Cosmic Rays, Anisotropy, Muons, Neutrinos.

1 Introduction

During the last decades, Galactic cosmic rays have been found to have a small but measurable energy dependent sidereal anisotropy in their arrival direction distribution with a relative amplitude of order of 10^{-4} to 10^{-3}. The first comprehensive observation of the cosmic ray sidereal anisotropy was provided by a network of muon detectors sensitive to cosmic rays between 10 and several hundred GeV [1]. More recent underground and surface array experiments in the Northern hemisphere have shown that a sidereal anisotropy is present in the TeV energy range (i.e. Tibet Air Shower Arrays (Tibet ASγ) [2], Milagro [3]). The IceCube neutrino observatory reported for the first time the observation of the cosmic rays sidereal anisotropy in the Southern sky at energies in excess of about 10 TeV [4]. The cosmic ray anisotropy reported by IceCube showed that the large scale features were a continuation of those observed in the Northern hemisphere in the same energy range.

At high energies, the Tibet ASγ collaboration reported the non-observation of a sidereal anisotropy in the cosmic ray arrival direction distribution at $\sim$ 300 TeV [2]. Another measurement at $\sim$370 TeV was recently published by the EAS-TOP collaboration reporting a larger sidereal anisotropy in amplitude with a shift in phase from that observed at lower energies [5]. At this point the two observations do not provide a coherent picture of the sidereal anisotropy at high energy in the Northern hemisphere.

In this contribution we present the analysis and the results of the study of large scale cosmic ray anisotropy at median energies of 20 and 400 TeV by IceCube for the Southern celestial sky. Observations of the energy dependence of the anisotropy could provide us with further information for the development of theoretical models to better understand the origin and propagation of cosmic rays.

2 Data Analysis

The main goal of the IceCube neutrino observatory is to detect astrophysical neutrinos. Neutrinos passing through the Earth and interacting in the vicinity of IceCube produce muons or other secondaries that emit Cherenkov radiation in the clear ice surrounding the detector. It is these light signals that the IceCube optical modules record. On the other hand, muons produced by cosmic ray air-showers in the atmosphere above IceCube are also detected. These are observed as down-going tracks.

The data used in this analysis are the downward going muons collected by the IceCube detector comprising 59 strings. The data were collected from May 2009 to May 2010 [6]. The events used in this analysis are those reconstructed by an online likelihood based reconstruction algorithm at an average rate of $\sim$1250 Hz with a median

angular resolution of $\sim 3^\circ$. A range of selection criteria is applied to that data to ensure good quality and stable runs. The final data set consists of 33×10^9 events corresponding to a detector livetime of 324.8 days.

Due to the detector's unique location, the IceCube Observatory has full coverage of the Southern sky up to declination angles of -25° degrees at any time of the year. The seasonal and atmospheric variation of the muon intensity were found to occur uniformly across the entire field of view, and therefore it did not affect the arrival distribution of the reconstructed events [4]. The crucial effect that needed to be accounted for was due to the geometrical shape of IceCube: events that were parallel to a larger number of strings were more efficiently reconstructed. The non-uniform time coverage due to detector downtime and run selection precluded the complete averaging of the detector geometrical asymmetry and generated artificial variations of the arrival direction of cosmic rays in equatorial coordinates. The local azimuthal asymmetry was corrected by reweighting the arrival directions of the data [4].

3 Energy Estimation

The energy dependence of the large scale anisotropy may hint at the nature of the source (or sources) of the cosmic rays, as well as their propagation through galactic magnetic fields. Similar measurements have been carried out over a wide range of energies by underground muon experiments and air shower arrays [1, 7, 8, 9, 10] but there are relatively few observations in the multi-TeV region.

Since IceCube detects cosmic ray properties indirectly through the observation of muons produced in the extensive air showers, the cosmic ray particles energy is inferred from the estimation of the muon energy. In this analysis, we use the number of optical modules Nch participating together with the zenith angle θ of the event to estimate the energy of the events. Using Monte Carlo simulations, we have identified cuts of constant energy in (Nch, θ) for the two event samples. The primary cosmic ray energy estimation had a resolution of about 0.5 in $\log_{10}$ scale and, this is due to the fact that it is dominated by the large fluctuations of the number and energy of muons produced in the extensive air showers. The low energy sample contained events with a median energy of 20 TeV, where 68% of the events were between $4-63$ TeV; and the high energy sample contained events with a median energy of 400 TeV, were 68% of the events were between $100-1258$ TeV.

4 Results

To investigate the arrival direction distribution of the cosmic rays, we study the relative intensity of the cosmic ray flux. The arrival direction distribution is dominated by the zenith angle dependence of the flux. Therefore, we normalize the flux within declination belts of width $\sim 3^\circ$, which corresponds to the angular resolution of the data.

To quantify the scale of the anisotropy, we fitted the right ascension projection distribution for declinations angles -25°to -75° degrees of the data to a first and second-order harmonic function of the form

$$\sum_{j=1}^{2} A_j \cos[j(\alpha-\phi_j)] + B \qquad (1)$$

where (A_i, ϕ_i) are the amplitude and phase of the anisotropy, α is the right ascension, and B is a constant. Figures 1 and 2 show the relative intensity cosmic ray maps together with the profile of the data in right ascension for events in both the 20 TeV and the 400 TeV energy sample. The error bars in the right ascension projection are derived by propagating the statistical errors from each declination belt, and the gray band indicates the estimated maximal systematic uncertainties (described in section 4.1.1). The solid line indicates the fit of eq. (1) to the data. The first and second harmonic amplitude and phase of the sidereal anisotropy for the low energy sample together with their statistical and systematic uncertainties are $A_1 = (7.9\pm0.1_{stat.}\pm0.4_{syst.})\times10^{-4}$ and $\phi_1 = 50.5^\circ\pm1.0^\circ_{stat}\pm 1.1^\circ_{syst.}$, $A_2 = (2.9\pm0.1_{stat.}\pm0.4_{syst.})\times10^{-4}$ and $\phi_2 = 299.5^\circ \pm 1.3^\circ_{stat} \pm 1.5^\circ_{syst.}$. While those for the high energy sample are $A_1 = (3.7\pm0.7_{stat.}\pm0.7_{syst.})\times10^{-4}$ and $\phi_1 = 239.2^\circ\pm10.6^\circ_{stat}\pm10.8^\circ_{syst.}$, $A_2 = (2.7\pm0.7_{stat.}\pm 0.6_{syst.})\times10^{-4}$ and $\phi_2 = 152.7^\circ \pm 7.0^\circ_{stat} \pm 4.2^\circ_{syst.}$.

4.1 Reliability Checks

4.1.1 Data Stability

In order to assess and quantify the systematic uncertainties in the sidereal anisotropy of cosmic ray arrival direction distribution a number of checks were applied by dividing the low and high energy data samples in exclusive halves based on different criteria. A full analysis was then applied for each dataset and the relative intensity distribution in right ascension was determined for each of them. The stability checks applied are:

- Seasonal variations dependence: where the data was divided in two seasons (winter and summer).
- Rate variations dependence: where the data was divided for each day by the sub-run (a sub-run corresponded to approximately 2 minutes of observations) rate fluctuating being greater than or less than the median rate of the day.
- Choices of events sample dependence: where the data was divided by the sub-run number using multiple categories.
- Non-uniform time coverage dependence due to detector down time and quality run selection: where the analysis was performed on the sub-sample of days with maximal data collection time.

The sidereal distribution of relative intensity in the arrival direction of the cosmic rays for the low and high energy samples are used to evaluate the spread in the experimental observation from the full-year event samples. The gray bands in the right ascension projection in Figures 1 and 2 describe the maximal spread obtained from the result of all the stability checks described in this section.

4.1.2 Solar Diurnal Anisotropy

To test for the stability of the observatory and its time coverage, an effective way to have an absolute calibration of the experimental sensitivity for the detection of the sidereal directional asymmetries is to measure the solar anisotropy from the Earth's revolution around the Sun. This observation has solid theoretical grounds and it was first reported in 1986 [11] and then later observed by multiple experiments in the multi-TeV energy range (i.e. [2], [3]). The observed solar anisotropy is consistent with a dipole that describes an apparent excess of cosmic rays in the direction of Earth's motion around the Sun and a deficit in the opposite direction.

Figure 3 shows the projections of the cosmic ray arrival direction in solar reference frame, for both energy samples (20 and 400 TeV). The error bars are the statistical errors, and the shaded bands indicate the expectation of the dipole. A fit to the projection of relative intensity distribution is shown by the black line and was done using the first harmonic term of eq. (1). The figures show that the experimental observation of the solar dipole is consistent with the expectations in both amplitude and phase. This observation of the solar diurnal anisotropy supports the reliability of the sidereal anisotropy determination.

4.1.3 Anti-sidereal Anisotropy

An annual modulation in the amplitude of the solar anisotropy is expected to result in a spurious effect in the sidereal anisotropy. This would produce a bias in the observed sidereal anisotropy. To estimate this bias the so-called anti-sidereal time, i.e. a non-physical time frame obtained by reversing the sign of the transformation from solar time to sidereal time [12].

Figure 4 shows the projections of the cosmic ray arrival direction in anti-sidereal reference frame, for both energy samples (20 and 400 TeV). The error bars are the statistical errors. The distributions were then fitted to the dipole term of eq. (1). The uncertainty in the first harmonic amplitude and phase implied by the study in the anti-sidereal time frame is within the statistical and systematic errors determined from the data stability tests. The absence of the signal in the anti-sidereal time insures the reliability of the anisotropy observed in sidereal time.

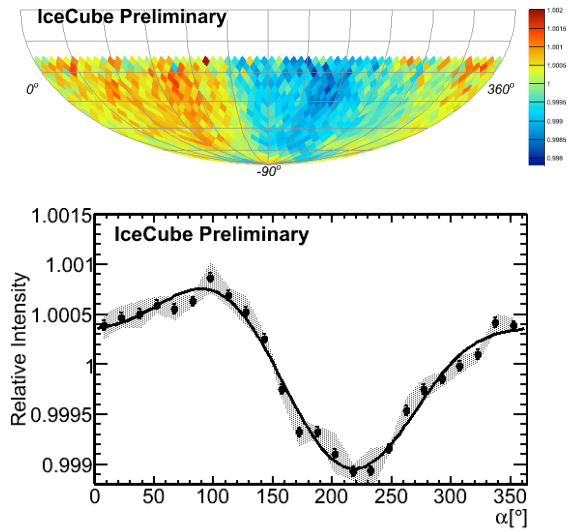

Figure 1: The top figure is the IceCube relative intensity cosmic ray map for the low energy sample (Median energy of the primary cosmic ray particle of 20 TeV). The bottom figure is the one dimensional projection in right ascension α of the two-dimensional cosmic ray map. The black line corresponds to the first and second harmonic fit to the data. The gray band indicates the estimated maximal systematic uncertainties.

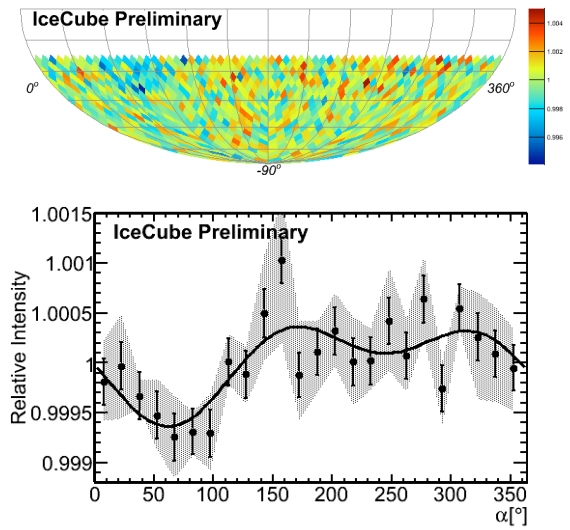

Figure 2: The top figure is the IceCube relative intensity cosmic ray map for the high energy sample (Median energy of the primary cosmic ray particle of 400 TeV). The bottom figures is the one dimensional projection in right ascension α of the two-dimensional cosmic ray map. The black line corresponds to the first and second harmonic fit to the data. The gray band indicates the estimated maximal systematic uncertainties.

5 Conclusion

In this contribution we presented the results on the large scale cosmic ray sidereal anisotropy at cosmic ray median

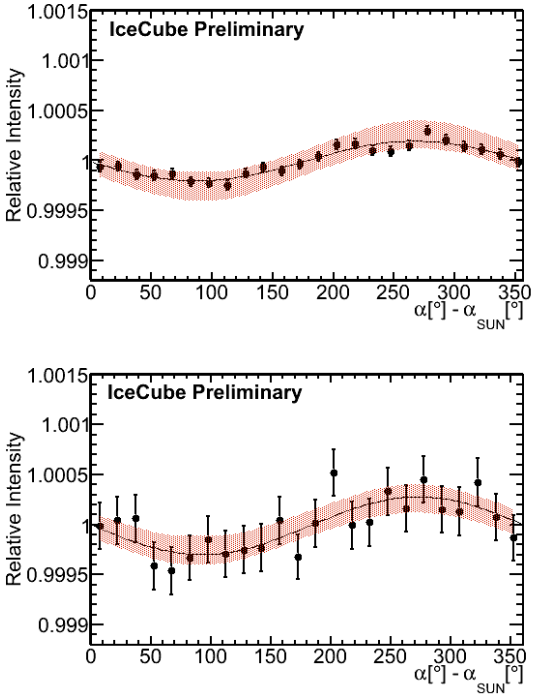

Figure 3: The solar projections for cosmic rays with median energy of 20 TeV (The top figure) and 400 TeV (The bottom figure). The error bars are the statistical errors, and the shaded band indicated the solar diurnal dipole expected from the motion of the Earth around the Sun.

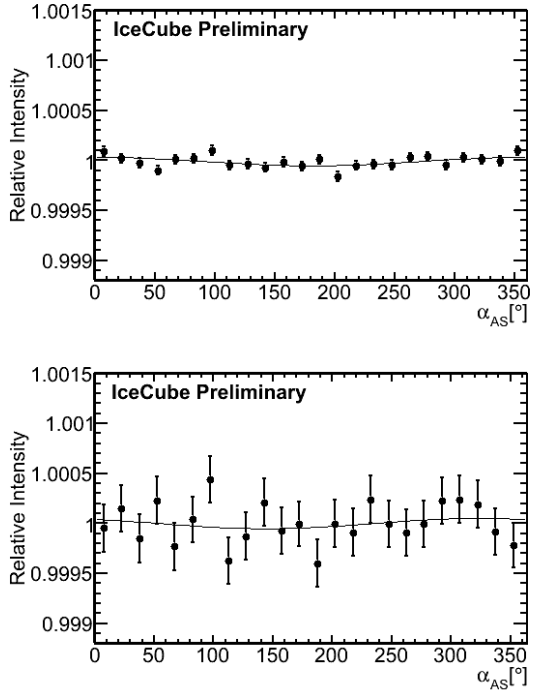

Figure 4: The anti-sidereal projections for cosmic rays with median energy of 20 TeV (The top figure) and 400 TeV (The bottom figure). The error bars are the statistical errors. The black line corresponds to the first harmonic fit to the data.

energies of 20 TeV and 400 TeV. The source of the sidereal anisotropy is still unknown. It is believed that a possible contribution to this observed anisotropy might be from the Compton-Getting effect, due to the orbital motion of the solar system around the galactic disk. However, the sidereal anisotropy from both energy samples do not appear to be consistent with that expected from the suggested Compton-Getting model neither in amplitude nor in phase.

The sidereal anisotropy observed at 20 TeV with IceCube-59 is consistent with the previously reported observation with IceCube [4], thus providing a confirmation of an apparent continuation of the arrival distribution pattern observed in the Northern hemisphere. On the other hand the sidereal anisotropy observed at 400 TeV shows substantial differences with respect to that at lower energy. The anisotropy at high energy shows a relative deficit region in right ascension where the broad excess dominated at primary median energy of 20 TeV. Also the wide relative deficit region at low energy seemed to have disappeared at primary median energy of 400 TeV. Whatever generated the sidereal anisotropy at 20 TeV seems to have no effect at 400 TeV.

This is the first observation of the sidereal anisotropy at 400 TeV in the Southern hemisphere. We are continuously analyzing events from IceCube with updated configurations. IceCube construction is now completed with 86 strings deployed with a volume of km^3 in January of 2011. With the higher statistical power expected from the observed cosmic ray muons we will be able to improve our understanding of the energy dependence of the anisotropy with more significance and close to the knee region. The energy dependence of the cosmic ray anisotropy is vital to our understanding of the source and propagation of cosmic rays.

References

[1] Nagashima et al., J. Geophys. Res., 1998, **103**: 17429.
[2] Amenomori et al., Science, 2006, **314**:439.
[3] Abdo et al., Astrophys. J., 2009, **698**:2121.
[4] Abbasi et al., Astrophys. J., 2010, **718**:L194.
[5] Aglietta et al., Astrophys. J., 2009, **692**:130.
[6] Abbasi et al., arXiv:1105.2326.
[7] Bercovitch, M., et al., International Cosmic Ray Conference,1981, **67**: 246.
[8] Cutler, D. J., et al., Astrophys. J., 1991, **376**: 322.
[9] Andreyev, Y. M., et al., International Cosmic Ray Conference, 1987, **2**: 22.
[10] Munakata, K., et al., International Cosmic Ray Conference,1999, **7**: 293.
[11] Cutler, D. J., & Groom, D. E., Nature, 1986,**322**: 434.
[12] Farley, F. J. M., & Storey, J. R., Proc. Phys. Soc., 1954,**67**: 996.
[13] Redfield, S., & Linsky, J. L., Astrophys. J., 2000,**534**: 825.

Observation of Anisotropy in the Arrival Direction Distribution of Cosmic Rays at TeV Energies with IceCube

THE ICECUBE COLLABORATION[1]
[1]*See special section in these proceedings*

Abstract: The IceCube neutrino detector at the South Pole is sensitive to atmospheric muons produced by primary cosmic rays in the TeV energy range. The high rate of events (about 2 kHz in the full 86-string detector) allows for searches of anisotropy in the arrival direction distribution of cosmic rays at the level of a few parts per mille. Using the muon data recorded with IceCube between 2007 and 2010, we show that the cosmic ray flux in the southern hemisphere is not isotropic, but exhibits significant structure on multiple angular scales. In addition to large-scale features in the form of strong dipole and quadrupole moments, the data include several localized regions of excess and deficit on scales between 10° and 30°. These features are statistically significant. The origin of the features is currently unknown.

Corresponding Authors: Segev BenZvi[2] (*sybenzvi@icecube.wisc.edu*),
Marcos Santander[2] (*santander@icecube.wisc.edu*), Simona Toscano[2] (*toscano@icecube.wisc.edu*),
Stefan Westerhoff[2] (*swesterhoff@icecube.wisc.edu*)
[2]*Dept. of Physics, University of Wisconsin-Madison, Madison, WI 53703, USA*

Keywords: Cosmic Rays – TeV; Anisotropy; Muons; Neutrinos

1 Introduction

The IceCube detector, deployed between 1450 m to 2450 m below the surface of the South Polar ice sheet, is designed to detect upward-going neutrinos from astrophysical sources. However, it is also sensitive to downward-going muons from cosmic-ray air showers. To penetrate the ice and trigger the detector, the muons must be produced by cosmic rays with energies of at least several TeV. The arrival direction of a cosmic muon is typically within 0.2° of the direction of the primary particle, so the arrival direction distribution of muons is also a map of cosmic ray arrival directions between about 1 and several hundred TeV.

At energies of a few TeV, it is believed that galactic magnetic fields should randomize the arrival directions of charged cosmic rays. However, in recent years an anisotropy in the arrival direction distribution has been reported on both large and small angular scales. The anisotropy is observed in the northern sky between several TeV and several hundred TeV by the Tibet ASγ array [1], Super-Kamiokande [2], Milagro [3, 4], ARGO-YBJ [5], and EAS-TOP [6]. In 2010, an analysis of muons recorded by the IceCube detector also revealed a large-scale anisotropy in the southern sky [7]. In these proceedings, we present the results of a search of the southern sky for anisotropy on all angular scales using data recorded between May 2009 and May 2010.

2 The IceCube Detector and Data

IceCube is a km^3-size neutrino detector frozen into the glacial ice sheet at the geographic South Pole. High-energy charged particles passing through the detector emit Cherenkov radiation, and their tracks are recorded by an array of Digital Optical Modules (DOMs) embedded in the ice. The DOMs are attached to 86 vertical cables, or strings (with 60 DOMs per string), which are used to transmit data to the surface. Construction of IceCube was completed in December 2010. The detector has been operating in various configurations since construction began. Between 2007 and 2008, it was operated with 22 strings deployed (IC22), between 2008 and 2009 with 40 strings (IC40), and between 2009 and 2010 with 59 strings.

Muons are identified using a simple majority trigger, which requires 8 or more DOMs in local coincidence within a $5\ \mu$s window. The trigger rate of downgoing muons is 0.5 kHz in IC22, 1.2 kHz in IC40, and 1.4 kHz in IC59, about a factor of 10^6 larger than the neutrino rate. The rate is too large to transfer complete waveforms for all events via satellite, so the muon data are reconstructed on-line and compressed using a Data Storage and Transfer (DST) format. Muon tracks are identified using a maximum-likelihood reconstruction, and the event arrival direction and energy estimators are stored in DST files and sent north by satellite. Digitized waveforms are discarded due to limited bandwidth.

The analysis presented in this paper uses the DST data collected during IC59 operations between May 20, 2009 and May 30, 2010. The data set contains nearly 3.4×10^{10} muon events recorded during a live time of 335.5 days. A cut in zenith angle at $65°$ removes less well-reconstructed tracks near the horizon, reducing the final analysis sample to 3.2×10^{10} events. The median angular resolution of events in the sample is $3°$; unlike the neutrino analysis, the cuts have not been optimized for point source identification. Using simulated data, we estimate the median energy of the events to be 20 TeV. The energy resolution of the cosmic ray primaries is about $\Delta \log(E/\text{eV}) = 0.5$.

3 Analysis

3.1 Calculation of the Reference Level

The arrival direction distribution of cosmic rays in IceCube exhibits anisotropy caused by non-physical effects such as gaps in the detector uptime. These effects must be removed before any physical anisotropy can be identified. Therefore, the first step in the analysis is the creation of a "reference map," a sky map that describes what the arrival direction distribution would be if the cosmic ray flux were isotropic. The reference map must be subtracted from the arrival direction distribution in the data to find regions where the cosmic ray flux deviates from the isotropic expectation.

We estimate a reference map for IC59 data using the time-scrambling method of Alexandreas et al. [8]. The sky is binned into an equal-area grid in equatorial coordinates with $0.9°$ resolution using the publicly-available HEALPix library [9]. From this sample two sky maps are produced. The data map $N(\alpha, \delta)$ stores the arrival directions of all events. For each detected event in the data map, "fake" events are generated by keeping the local zenith and azimuth angles (θ, ϕ) fixed but reassigning the time to that of another event recorded within a pre-defined time window Δt. The event times within the window are resampled 20 times and used to generate 20 fake celestial coordinate pairs (α, δ) which are used to fill a reference sky map $\langle N(\alpha, \delta)\rangle$ with a weight of 1/20.

A known disadvantage of the method is that it can be biased by a strong anisotropy, leading to artificial deficits or excesses next to regions of true excess or deficit [3]. However, the procedure does preserve the local arrival direction distribution of the data and naturally compensates for variations in the event rate which are difficult to model, such as changes in atmospheric conditions which affect the production of muons in air showers. The only critical requirement for time scrambling is to choose the buffer length Δt such that detector conditions remain stable during this period. Using χ^2 tests to compare the distribution of arrival directions in local coordinates across measurement periods, we have verified that the IceCube detector is stable over periods of at least one full day. In this analysis we choose $\Delta t = 24$ hr.

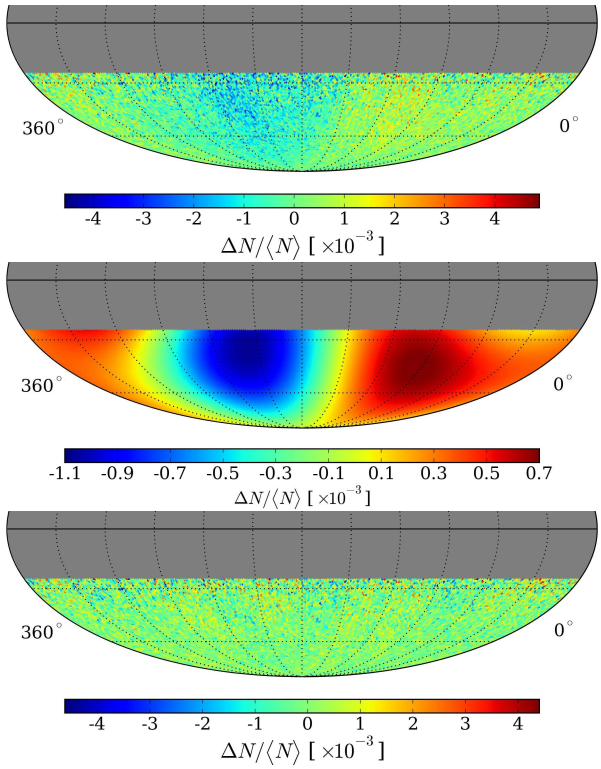

Figure 1: *Top*: Relative intensity of the IC59 data produced with $\Delta t = 24$ hr. *Middle*: Fit of dipole and quadrupole moments to the relative intensity. *Bottom*: Residual map after removal of the dipole and quadrupole.

3.2 Relative Intensity

Once the data and reference maps are calculated, deviations from isotropy can be analyzed by computing the relative intensity

$$\frac{\Delta N_i}{\langle N\rangle_i} = \frac{N_i(\alpha, \delta) - \langle N_i(\alpha, \delta)\rangle}{\langle N_i(\alpha, \delta)\rangle}. \quad (1)$$

which gives the amplitude of deviations from the isotropic expectation in each angular bin i. The significance of the deviation in bin i can be calculated using the method of Li and Ma [10].

A map of relative intensity of the IC59 data, binned with $0.9°$ resolution, is shown at the top of Fig. 1. The map exhibits obvious correlations between bins, such as a broad excess in the relative counts near $\alpha = 105°$ and a broad deficit near $\alpha = 225°$. The relative intensity in these regions is of order 10^{-3}. This structure is the large-scale anisotropy reported in the IC22 data by Abbasi et al. [7]. Since the IC59 data set is larger than that of IC22 by an order of magnitude, it is possible to see the large-scale structure in the data without further rebinning.

3.3 Removal of Large-Scale Structure

The relative intensity shown at the top of Fig. 1 is dominated by large-scale structures, but there are additional

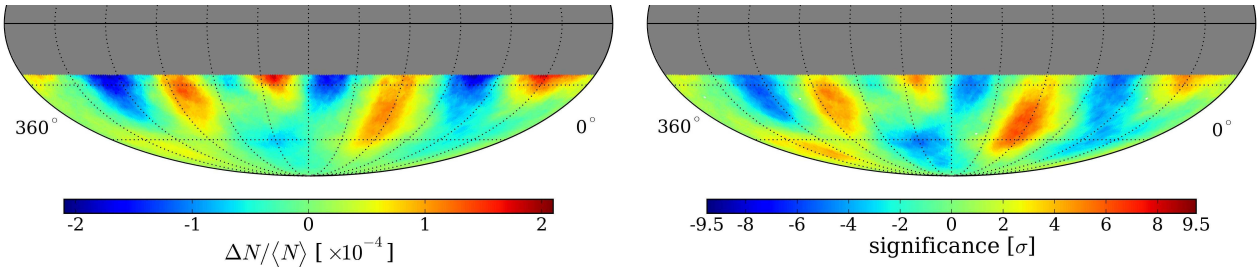

Figure 2: IC59 residual maps after subtraction of dipole and quadrupole moments, showing relative intensity (left) and significance before trial factors are applied (right). The maps have been smoothed with a circular window of $20°$.

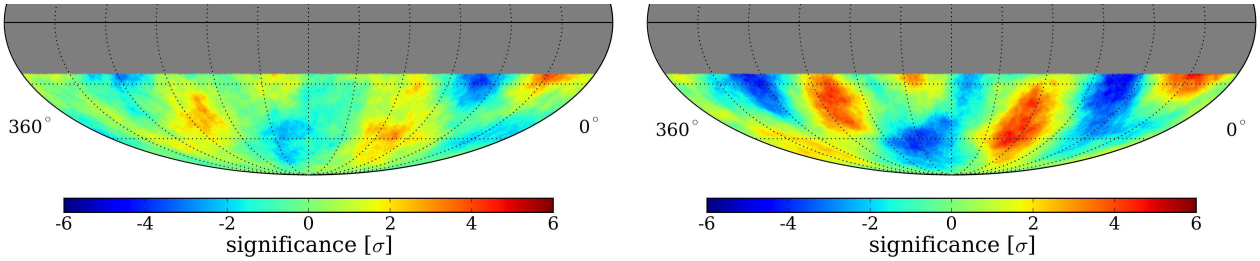

Figure 3: Residual maps from IC22 (left) and IC40 (right) showing the significance of deficit and excess regions with $20°$ smoothing.

small-scale features in the map. This can be demonstrated by calculating the angular power spectrum of the data, which exhibits significant power not only at the largest angular scales, but also down to scales of about $10°$ (see detailed discussion in Abbasi et al. [11]).

We can also demonstrate the presence of small-scale structure by explicitly removing the largest angular correlations in the data. This is accomplished by fitting dipole and quadrupole terms to the relative intensity map and then subtracting the fit to obtain a map of residual counts. In the middle panel of Fig. 1, we show the result of the fit of dipole and quadrupole moments to the intensity map. By themselves, these two terms account for much of the amplitude of the per-mille anisotropy observed in the data. However, the fit $\chi^2/\text{ndf} = 14743/14187$ corresponds to a χ^2-probability of approximately 0.05%, suggesting that the dipole and quadrupole are not sufficient to explain all of the structures observed in the angular distribution of $\Delta N/\langle N\rangle$.

Subtraction of the dipole and quadrupole fit from the data gives the bottom panel in Fig. 1. The fit residuals are relatively featureless at first glance, but the bin size is not optimized for a study of significant anisotropy at angular scales larger than the angular resolution of the detector. To increase the sensitivity to the small-scale structure in the data, we apply a smoothing procedure which takes the reference level and residual data counts in each bin and adds the counts from pixels within some angular radius of the bin. This procedure results in a map with Poisson uncertainties, though the bins are no longer statistically independent.

Smoothed residual maps of relative intensity and significance are shown in Fig. 2. To make this figure, a smoothing radius of $20°$ was chosen. Strong regions of excess and deficit are visible in the data. Note that the actual size of any given excess or deficit region (and thus the optimal smoothing scale) is not known *a priori*. Therefore, we study the sky map on all smoothing scales from $3°$ (the angular resolution of the data) to $45°$ in steps of $1°$ and search for regions of high significance at any location.

Applying this procedure, the two most significant features on the sky are a region with a peak significance of 5.3σ at a smoothing radius of $22°$ ($\alpha = 122.4°, \delta = -47.4°$) and a region of peak significance 4.9σ at a smoothing radius of $13°$ ($\alpha = 263.0°, -44.1°$). The significance values account for statistical trials due to the scan over smoothing radii and the location of the most significant pixels. The trial factors were estimated using a Monte Carlo simulation of an isotropic flux recorded by the IceCube detector.

4 Systematic Checks

Several tests have been performed on the data to ensure the stability of the observed anisotropy and to rule out possible sources of systematic bias. Among the influences that might cause spurious non-physical anisotropies are the detector geometry, the detector livetime, non-uniform exposure of the detector to different regions of the sky, and diurnal and seasonal variations in atmospheric conditions. Due to its unique location at the South Pole, many of these effects play a lesser role for IceCube than for detectors at the middle latitudes. We check the validity of this assumption by searching the data for a signal expected in solar coordinates, and by examining the data from previous configurations of the detector.

4.1 Solar Dipole Analysis

The cosmic rays at TeV energies do not co-rotate with the Earth about the Sun, and so it is expected that the flux of cosmic rays should exhibit a dipole modulation in solar coordinates. The expected change in relative intensity is given by

$$\frac{\Delta I}{I} = (\gamma + 2)\frac{v}{c}\cos\theta, \tag{2}$$

where I is the cosmic ray intensity, $\gamma = 2.7$ is the power law index of the energy spectrum at several TeV, v/c is the ratio of the orbital velocity of the Earth with respect to the speed of light, and θ is the angle between the cosmic ray arrival direction and the direction of motion of the Earth. Given $v = 30$ km s^{-1}, we expect an amplitude of 4.7×10^{-4}.

The solar dipole provides a convenient measurement with which to check the analysis technique. The reference and data maps were computed in solar coordinates, and the relative intensity map has been fit with a dipole function. A single dipole describes the data quite well: the fit $\chi^2/\text{ndf} = 14206.8/14192$ corresponds to a χ^2-probability of 41.6%. The dipole is aligned at a longitude of $270°$ in solar coordinates, following the expectation for a relative-motion anisotropy in this coordinate frame. Its amplitude is $(3.66 \pm 0.14 \pm 0.99) \times 10^{-4}$, in agreement with the expectation within the large systematic uncertainty. A more detailed study of the solar dipole anisotropy is presented in Abbasi and Desiati [12].

4.2 Anti-Sidereal Time Analysis

Seasonal variations in the solar dipole anisotropy can create spurious signals in equatorial coordinates, and vice-versa. We study this effect using an artificial time scale called anti-sidereal time, which is calculated by reversing the sign of the transformation between universal time and sidereal time. No physical anisotropy is expected in this reference frame, but it can be used to identify systematic distortions due to seasonal effects.

We have produced sky maps using anti-sidereal coordinates and performed the same analysis presented in Section 3. No regions of significant excess or deficit are observed in the anti-sidereal maps for any smoothing scale. A detailed discussion is provided in [11].

4.3 Comparison to IC22 and IC40 Data

An important cross-check of the IC59 analysis can be made by applying the same method to data recorded in the two data periods prior to IC59. The IC22 data set contains 4×10^9 events recorded between July 2007 and April 2008, and the IC40 data set contains 1.9×10^{10} events recorded between April 2008 and April 2009. While the samples are smaller than IC59, we expect to observe the most prominent structures in these data, albeit with reduced significance. The IC22 and IC40 data can be used to verify that the structures observed in the arrival direction distribution do not depend on the geometry of the detector or the data-taking period. For example, the shape of IC22 was highly asymmetrical, with a long and a short axis.

In Fig. 3, we show the residual maps from IC22 and IC40 after the subtraction of dipole and quadrupole terms and smoothing by $20°$. While none of the features in IC22 and IC40 have a pre-trial significance above 5σ, they align with the regions of deficit and excess observed with IC59 data (cf. Fig 2). The main features on both large and small scales appear to be persistent in all data sets.

5 Conclusions

Using 3.2×10^{10} events recorded with the partially-deployed IceCube detector between May 2009 and May 2010, we have found that the arrival direction distribution of cosmic rays at several TeV exhibits significant anisotropy on several angular scales. The data are dominated by dipole and quadrupole moments, but there is also significant structure on angular scales down to about $10°$. These structures become visible in the sky map when the dominant terms are subtracted.

There is currently no explanation for these local enhancements in the cosmic ray flux, and so the study of cosmic ray arrival directions in the TeV region will continue to be a major ongoing effort in IceCube. We are currently studying the anisotropy in the 79-string configuration of the detector (IC79). During the next several years, with the IceCube detector operating in its complete 86-string configuration, the data will increase by 4.5×10^{10} events per year. With these high statistics we will be able to study possible time dependencies in the anisotropy and compare to similar studies in the northern hemisphere [4, 13]

References

[1] M. Amenomori et al., Astrophys. J., 2005, **626**: L29
[2] G. Guillian et al., Phys. Rev., 2007, **D75**: 062003
[3] A.A. Abdo et al. Phys. Rev. Lett., 2008, **101**: 221101
[4] A.A. Abdo et al. Astrophys. J., 2009, **698**: 2121
[5] S. Vernetto et al. Proc. 31st ICRC, 2009, Łódź, Poland
[6] M. Aglietta et al. Astrophys. J., 2009, **692**: L130
[7] R. Abbasi et al., Astrophys. J., 2010, **718**: L194
[8] D.E. Alexandreas et al., NIM A, 1993, **328**: 570
[9] K.M. Gorski et al., Astrophys. J., 2005, **622**: 759
[10] T.-P. Li and Y.-Q. Ma, Astrophys. J., (1983), **272**: 317
[11] R. Abbasi et al., arXiv:1105.2326 [astro-ph], submitted to Astrophys. J., 2011
[12] R. Abbasi and P. Desiati, these proceedings.
[13] M. Amenomori et al., Astrophys. J., 2010, **711**: 119

Measurement of the Solar Anisotropy with IceCube

THE ICECUBE COLLABORATION[1]
[1]*See special section in these proceedings*

Abstract:

IceCube is a kilometer scale neutrino observatory that collects a large number of cosmic ray induced muon events. These events, which are background for neutrino searches, are observed at a rate that is suitable for high-statistics studies of cosmic rays in the Southern hemisphere. The apparent anisotropy created by the motion of the Earth around the Sun, the solar dipole, is systematically analyzed. The solar dipole is simulated, and the predictions for the integrated effect over an entire year and over shorter periods of a quarter-year are compared to data. The experimental observation is found to be in good agreement with the expectation. Finally, we show that the interference between the solar dipole and the sidereal anisotropy is well understood within the statistical uncertainties.

Corresponding Authors: Craig Price[2] (*cprice@icecube.wisc.edu*), Rasha Abbasi[2] (*rasha.abbasi@icecube.wisc.edu*), Paolo Desiati[2] (*paolo.desiati@icecube.wisc.edu*)
[2]*Dept. of Physics, University of Wisconsin-Madison, Madison, WI 53703, USA*

Keywords: IceCube; Cosmic Rays; Anisotropy; Muons; Neutrinos

1 Introduction

The motion of an observer in the cosmic ray plasma is predicted to cause an apparent dipole effect in the cosmic ray arrival direction; this effect was first pointed out in 1935 by Arthur Compton and Ivan Getting [1]. Using this principle, the motion of the Earth around the Sun would produce an excess in the direction of motion and a deficit in the opposite direction. This observation was first reported by Cutler in 1986 [2], and then later observed by multiple experiments (i.e. Tibet Air Shower Arrays (Tibet ASγ) [3], Milagro [4], and EAS-TOP [5]). This measurement is referred to in this contribution as the solar dipole effect anisotropy and is expressed as

$$\frac{\Delta I}{\langle I \rangle} = (\gamma + 2)\frac{v}{c}\cos(\theta_v) \tag{1}$$

where I is the intensity, γ is the differential cosmic ray spectral index, v is the Earth's velocity, c is the speed of light, and θ_v is the angle between the reconstructed arrival direction of the cosmic rays and the direction of the motion of the Earth [6].

In addition to the solar dipole effect, galactic cosmic ray anisotropies have been observed by underground and surface array experiments in the Northern hemisphere such as Tibet ASγ [3]. Furthermore, IceCube recently reported the first observation of the sidereal anisotropy in cosmic ray arrival direction in the Southern sky [7] with a relative amplitude of the order of 10^{-4} to 10^{-3}. The cosmic ray anisotropy showed that the sidereal anisotropy in the Southern sky is a continuation of that observed in the Northern hemisphere.

In this proceeding, we report on the study of the observation and the expectation of the solar dipole effect in one full year. We also examine the effect of the mutual interference between the sidereal anisotropy and the solar dipole effect by examining quarter-year periods. The solar dipole effect and the interference between the sidereal and the solar effect over quarter-year periods is found to be well understood. This understanding supports the reliability of the sidereal anisotropy observations.

2 Data Analysis

IceCube is optimized for the detection of up-going, high-energy neutrinos, however its trigger rate is dominated by down-going atmospheric muons created in cosmic ray air-showers above the detector. In this work, we use the down-going atmospheric muon flux as our signal to study cosmic rays in the Southern sky. The data used in this analysis are the down-going muons collected by the IceCube detector in its 59-string configuration from May 2009 to May 2010. The data are reconstructed by an online maximum likelihood based reconstruction algorithm at an average rate of $\sim$1.2 kHz. A range of selection criteria is applied to the data to ensure detector stability. The final data set consists

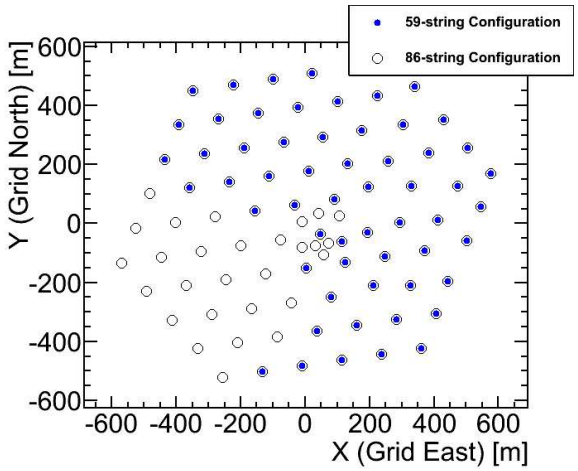

Figure 1: This plot shows the IceCube configuration with 86 strings in empty circles and the 59-string configuration in filled circles.

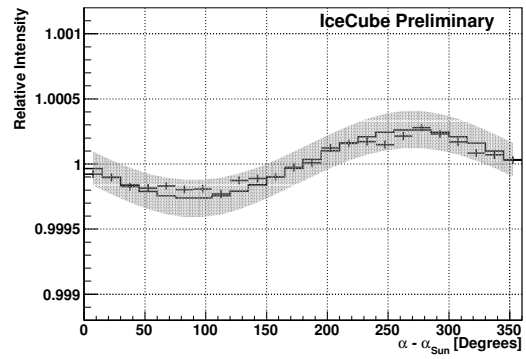

Figure 2: The plot shows the one-dimensional projection in $\alpha - \alpha_{Sun}$ of the relative intensity of cosmic rays. The data are shown with statistical uncertainties in black crosses, and the black line corresponds to the expectation from eq. 1. The gray shaded band indicates the 68% spread of the uncertainty in the simulated solar dipole.

of 33 billion events and corresponds to a detector livetime of 324.8 days. The events are initiated by muons from cosmic ray air-showers with a median primary energy of 20 TeV. The angular resolution between the muon to the primary cosmic ray particle has a median value of $\sim 3°$.

Located at the South Pole, IceCube observes the Southern sky year-round. However, an artificial azimuthal asymmetry occurs as an artifact of the detector's geometrical configuration (Figure 1) combined with non-uniform time coverage. This azimuthal asymmetry was eliminated by reweighting the azimuthal arrival directions of the incoming cosmic rays [7].

3 Solar Dipole Anisotropy Measurement and Expectation

The solar dipole is a well-known signal, both from theory and from observations by other experiments. A measurement of this well-known signal with IceCube strongly supports the reliability of the observation of the sidereal anisotropy with the same detector [8].

The amplitude of the solar dipole depends on the geographical latitude of the observer and on the angular distribution of the detected cosmic ray events at the observatory. Due to the location of the IceCube Observatory at the South Pole, the sky is fully visible at any given time. Therefore, the solar dipole is observed in a reference system where the location of the Sun is fixed, where the latitude coordinate is the declination, and the longitude coordinate is defined to be the difference between the right ascension of the cosmic ray arrival direction and the right ascension of the Sun ($\alpha - \alpha_{Sun}$). In this reference frame, the excess due to the solar dipole is expected to be at 270° and a deficit at 90°.

To verify that the experimental observation of the solar dipole is consistent with the expectation, the predicted projection of the solar anisotropy was calculated for the IceCube location. Since the observed amplitude of the solar dipole depends on the actual angular distribution of the detected muon events, the calculation of the expectation was performed using the azimuth-corrected experimental data. The expectation of the solar dipole was calculated by computing the relative intensity of the solar dipole through the cosmic ray plasma (through eq. 1). Instead of counting the number of events within a given bin in right ascension from the Sun, we calculated for each event, a mean weight corresponding to the expected relative intensity of the solar dipole.

The uncertainties in the cosmic ray spectral index, in the Earth's velocity, and in the reconstructed arrival direction of the events were included into the calculation of the uncertainty of the expectation. The mean spectral index was evaluated using the all-particle cosmic ray spectrum from [9] and was found to be 2.67 $\pm$ 0.19. The value used for Earth's velocity was v = 29.8 $\pm$ 0.5 km/s, where the error takes into account the spread between the maximum and minimum along the elliptical orbit. The angle θ_v between the reconstructed direction of the muon events and the Earth's velocity vector at the time the event was detected was evaluated accounting for the experimental point spread function. The expected solar dipole distribution, including the 68% spread in the uncertainty of the expectation, is shown in Figure 2. This figure shows that the observation is consistent with the expectation in both amplitude and phase.

4 Interference between the Sidereal and Solar Anisotropy

4.1 The Sidereal Anisotropy Interference in the Solar Dipole Anisotropy

A check applied to ensure that the solar dipole was well understood was to compare the expected solar dipole distribution to the observed distribution over the three month intervals (February-April, May-July, August-October, and November-January) with approximately the same detector livetime. However, complications exist in this simple dipole picture because if the data are not collected within an integer number of full years, the solar dipole is expected to be strongly distorted by the sidereal anisotropy [7]. This spurious effect is expected because the sidereal reference frame is defined where the celestial sky is fixed, while the solar reference frame is defined where the Sun is fixed. It takes about four fewer minutes to complete a sidereal day than a solar day. Therefore, a static point in the sidereal reference frame will move across the solar frame and return to the same position on the sky in one full year (this is observed implicitly in Figure 2). Therefore, any static sidereal distribution averages to zero in the solar reference frame after one year but not over partial time intervals of the year.

The points with their statistical errors in Figure 3 show the $\alpha - \alpha_{Sun}$ projection of the data collected in the time interval between February and April. The black line shows the solar dipole expectation from the motion of the Earth around the Sun for the same time interval. This illustrates the effect of the distortion by the sidereal anisotropy in the solar dipole. The plot shows that the observation in the solar reference frame is not in agreement with what is expected from the solar dipole alone and is strongly distorted by the sidereal anisotropy.

To eliminate such contamination, the experimental sidereal anisotropy distribution was used to determine how it would look like in solar reference frame. Specifically, a numerical calculation was performed where, every 100μs, an event was generated with a unique UTC time and with right ascension from the all-year experimental sidereal distribution. The corresponding distribution in $\alpha - \alpha_{Sun}$ was determined for the February-April time period and is shown in Figure 4. Once the sidereal anisotropy effect in the solar reference frame is known, it is then subtracted from the distribution measured in the solar reference frame.

Figure 3 shows the distorted cosmic ray distribution in the solar reference frame, and Figure 5 shows the distorted distribution minus the sidereal interference. The plot shows that the data, after correcting for the sidereal effect, is in agreement with the solar dipole expectation for the period from February to April. This effect was also estimated for each of the next three time intervals (May-July, August-October, and November-January) using the same method. The data was found to be in agreement with the expectation within statistical fluctuations.

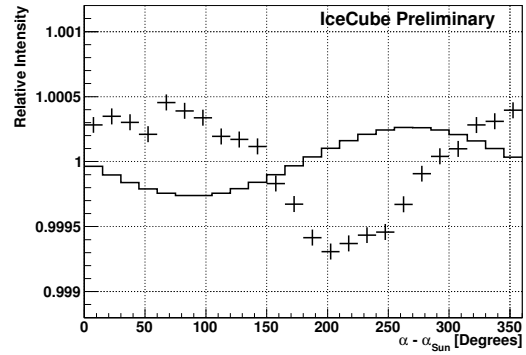

Figure 3: This plot shows the relative intensity of the one-dimensional projection of right ascension with respect to the Sun. The observed cosmic ray events in the period from February to April are shown with statistical uncertainties in the black crosses, and the black line is the relative intensity of the expected solar dipole for the same time period.

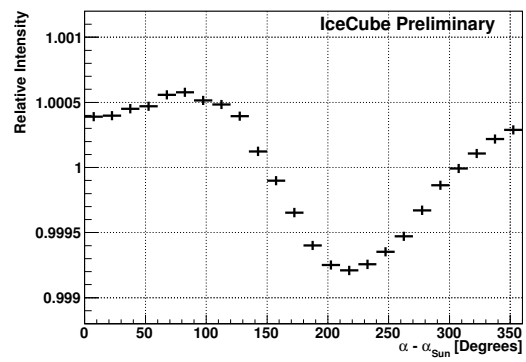

Figure 4: This plot shows the relative intensity of the sidereal anisotropy as it would appear in $\alpha - \alpha_{Sun}$ projection from February to April in absence of the solar dipole. The error bars are the statistical uncertainties.

4.2 The Solar Dipole Anisotropy Interference in the Sidereal Anisotropy

Similarly, the effect of the solar dipole interference in the sidereal anisotropy was also checked. This check allows for a better estimate of the systematic effect of the seasonal variation dependence in the sidereal anisotropy of the cosmic ray arrival direction [7]. If the relative intensity in equatorial coordinates is measured over a full year, then the observed sidereal anisotropy is devoid of any distortions by the solar dipole as explained previously. However, similar to the observation of the solar dipole in a quarter-year, we observe (as shown in Figure 6) that the sidereal anisotropy measured in the three month periods between February and March (in gray points) deviates from the full dataset observation (in black line).

This deviation is smaller than the solar dipole's distortion and is consistent with what we would expect. If the same sidereal-to-solar transformation procedure used previously

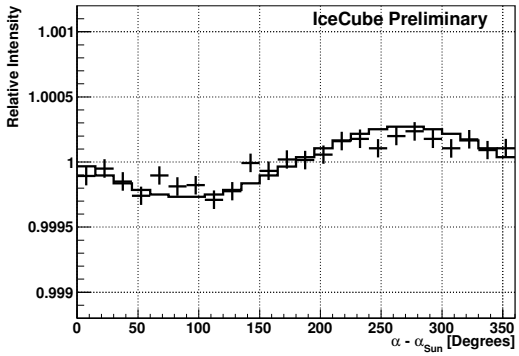

Figure 5: This plot shows the relative intensity of the one-dimensional projection in right ascension with respect to the Sun. The observed cosmic ray events with their statistical uncertainties in the period from February to April minus the propagated sidereal anisotropy in the solar reference frame for same time period are shown in black crosses. The black line is the relative intensity of the expected solar dipole.

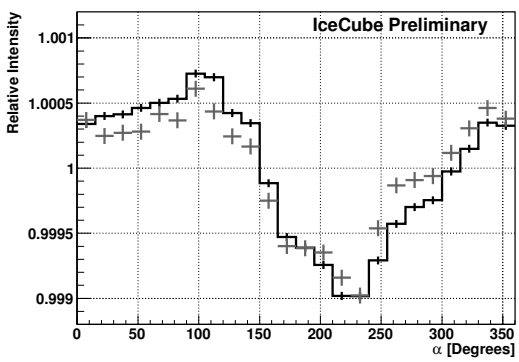

Figure 6: This plot shows the relative intensity of the one-dimensional projection of right ascension. The gray crosses are the observed cosmic ray events in the sidereal reference frame in the period from February to April. The black line is the relative intensity of the same sidereal anisotropy except over the full year. Both the full year and the quarter-year projections are plotted with their statistical error bars.

is applied, but for the sidereal anisotropy, then the solar dipole contribution from the sidereal observation is eliminated as shown in Figure 7. This effect was also corrected for the next three time intervals (May-July, August-October, and November-January) using the same method. The corrected sidereal anisotropy over each of the time intervals was also found to be in agreement with that observed over a full year.

5 Conclusion

In this contribution, we presented the observation of the solar dipole using the data collected by the 59-string configu-

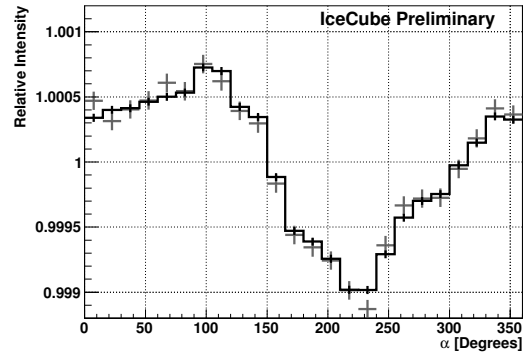

Figure 7: This plot shows the relative intensity of the one-dimensional projection of right ascension. The gray crosses are the observed cosmic ray events in the sidereal reference frame in the period from February to April minus the propagated solar anisotropy in the sidereal reference frame for same time period. The black line is the relative intensity of the same sidereal anisotropy except over the full year. Both the full year and the quarter-year projections are plotted with their statistical error bars.

ration of IceCube from May 2009 to May 2010. The solar dipole effect is studied in one full year and in 3 months intervals. The observed solar dipole in these time intervals was found to be consistent with what is expected from the motion of the Earth around the Sun in both amplitude and phase. The solar dipole effect is a well understood measurement that confirms, within statistical uncertainty, the reliability of the large-scale sidereal cosmic ray anisotropy observations.

References

[1] Compton, A. H., & Getting, I. A. Physical Review, 1935, **47**: 817.
[2] Cutler, D. J., & Groom, D. E., Nature, 1986,**322**, 434.
[3] Amenomori et al., Science, 2006, **314**: 439.
[4] Abdo et al., Astrophys. J., 2009, **698**: 2121.
[5] Aglietta et al., Astrophys. J., 2009, **692**: L130.
[6] Gleeson, L. J., & Axford, W. I. Ap&SS, 1968, **2**: 431.
[7] Abbasi et al., Astrophys. J., 2010, **718**: L194.
[8] IceCube Collaboration, paper 0305, these proceedings.
[9] Hörandel, J. R., Astroparticle Physics, 2003, **19**: 193.